MiWEBA

Millimetre-**W**ave **E**volution for **B**ackhaul and **A**ccess

EU Contract No. FP7-ICT-608637

WP5: Propagation, Antennas and Multi-Antenna Techniques

D5.1: Channel Modeling and Characterization

Contractual date:	M12
Actual date:	M12
Authors:	See list
Work package:	D5.1 Channel Modeling and Characterization
Security:	Public
Nature:	Report
Version:	1.0
Number of pages:	95

Abstract

This report contains results of the Work Package 5.1 “Channel modeling and characterization” for mmWave communication links at 60 GHz band. Chapter 2 gives an overview of most current mmWave experimental measurements and channel models. The scenarios and environment measurements in order to provide the necessary input data for deriving the model parameters are described in chapter 3. The mmWave channel experimental measurements results presented in chapter 4 along with the ray tracing modeling of the experimental scenarios and environments. Chapter 5 provides the new mmWave channel modeling methodology and 3D quasi-deterministic channel models for all MiWEBA scenarios. Final conclusions are given in chapter 6.

Keywords

mmWave, 3D channel model, ray tracing, stochastic, analytical and quasi-deterministic approach

Authors

Intel Corporation	Alexander Maltsev	alexander.maltsev@intel.com
	Andrey Pudeyev	andrey.pudeyev@intel.com
	Ilya Bolotin	ilya.bolotin@intel.com
	Gregory Morozov	gregory.v.morozov@intel.com
	Ingolf Karls	ingolf.karls@intel.com
	Michael Faerber	michael.faerber.intel.com
Orange	Isabelle Siaud	isabelle.siaud@orange.com
	Anne-Marie Ulmer-Moll	annemarie.ulmermoll@orange.com
	Jean-Marc Conrat	jeanmarc.conrat@orange.com
Fraunhofer HHI	Richard J. Weiler	richard.weiler@hhi.fraunhofer.de
	Michael Peter	michael.peter@hhi.fraunhofer.de
	Wilhelm Keusgen	Wilhelm.keusgen@hhi.fraunhofer.de

Table of contents

Abbreviations

Acronym	Description
AB	Advisory Board
AFO	Administrative Financial Office
APDP	Average Power Delay Profile
ART	Above Roof Top
AS	Azimuth Spread
BBU	Base Band Unit
BS	Base Station
COMP	Coordinated Multi-Point Transmission
C-plane	Control Plane
C-RAN	Cloud RAN
CSI	Channel State Information
DS	Delay Spread
EU	European Union
FST	Fast Session Transfer
HARQ	Hybrid Automatic Repeat Request
HetNet	Heterogeneous Network
ICD	Inter-Cell Distance
JP	Japan
LA	Link Adaptation
LOS	Line-of-Sight
MIM	Multiple Interface Management
MIMO	Multiple-Input Multiple-Output
MMR	Mobile Multi-hop Relay stations
mmWave	Millimeter-Wave band (30 to 300 GHz) will be used for 6 to 100 GHz
MPC	Multi Path Component
MS	Mobile Station
MTCN	Multi-Technology Cellular Networks
MTLA	Multi-Technology Link Adaptation
NLOS	Non-Line-of-Sight

PL	Path Loss
PoC	Proof of Concept
RPS	Reference Position Signal
RRH	Remote Radio Head
RRM	Radio Resource Management
RRU	Remote Radio Unit
RS	Relay Station
RX	Receiver
SP	Service Period
SRD	Short Range Distance
TX	Transceiver
UE	User Equipment
U-plane	User Plane
UWB	Ultra Wide Band

Executive Summary

There is mounting attention in using millimeter wave (mmWave) bands including 60 GHz for next generation mobile wireless networks. The absolute challenge for an mmWave channel model is to have just one channel model with adjustable parameters for all scenarios and propagation effects for the full frequency range from 6 GHz to 100 GHz. A feasible one is to develop a reasonable collection of 3D channel models for the most likely outdoor use case environments and scenarios.

Hence plenty of expensive measurement campaigns were already completed and are being currently done to characterize the mmWave communication channel in particular for these outdoor environments and scenarios. Then, using the measurement databases created, several approaches are investigated to predict the measured data or statistics such as path length, delay and angular spreads in the outdoor wireless network environments and scenarios. There are some preliminary 3GPP-like 3D mmWave channel models developed using either an analytical, a statistical or a ray-tracing based statistical approach to model the outdoor mmWave channel. The majority of these channel models tries to adopt to the 3GPP 3D channel model structure achieving a good fit with available 3GPP system level simulation environments.

All the currently available measurement campaigns and analysis have still got open issues like how to deal with human body shadowing or reflections due to moving vehicles or attenuation by dense vegetation in cities. More exploration is also needed to elaborate on whether mmWave systems are noise or interference limited, and the important aspects of polarization and there is the request for much greater temporal and spatial channel model resolution.

Consequently a new quasi-deterministic (Q-D) approach has been developed for modeling the outdoor and indoor channels at 60 GHz. The model is based on the representation of the mmWave channel impulse response as superposition of a few quasi-deterministic strong rays (D-rays) and a number of relatively weak random rays (R-rays). The structure of the proposed channel model allowed natural description of the scenario-specific geometric properties, the reflection attenuation and scattering, ray blockage and the mobility effects.

The 3D channel models for all main scenarios defined in the MiWEBA project proposal are delivered for open area (university campus), street canyon and hotel lobby in the framework of the Q-D approach. The appropriate model parameters for access links were selected on the base of experimental measurements and ray-tracing modeling. The versatility of the Q-D approach allows the developed channel models to be used for other usage models with same geometries. For all main scenarios the Q-D channel model was extended to Device to Device (D2D) links with a simple change of TX antenna parameters. In similar way, the street canyon access model was extended to the street-level backhaul deployment.

The MiWEBA channel model approach introduced firstly in this report addresses major challenges to model the outdoor wireless communication channel for mmWave including the 60 GHz band. This new model is of utmost importance for further measurement campaigns, channel model characterization, system level simulations and network access capacity estimations.

1 Introduction

1.1 Key technical challenges

The definitive challenge for an mmWave channel model is to have just one channel model with adjustable parameters for all scenarios and propagation effects for the full frequency range from 6 GHz to 100 GHz.

Well known channel models such as 3GPP Spatial Channel Model (SCM) [1], WINNER [2] and ITU-R IMT-Advanced propagation model guidelines [3] were built on extensive channel propagation measurement campaigns and are for frequencies of up to 6 GHz. The IEEE 802.11ad channel model [4] focus on the 60 GHz band indoor (created deterministically, parameterization is site specific) [5]. QuaDRIGa [6] models MIMO radio channels via ray-tracing for specific network configurations, such as indoor, indoor/outdoor or outdoor environments implementing a 3D geometry-based stochastic channel model. COST 2100 [7] works at the COST channel model, which counts on measurement campaigns and extractions of parameters. The most recent METIS 2020 intermediate deliverable D1.2 [8] "Initial channel models based on measurements" concludes that there might not be "one" channel modelling approach to fulfil the needs for e.g. mmWave bands. It is proposed to explore further geometry-based stochastic, visibility-region based, grid-based GSCM and map-based models including parameterization from measurement campaign results. Final METIS channel models will be published in D1.4 in February 2015.

Measurement campaign challenges arise from the sheer variety of propagation environments according to D1.1 which are indoor isolated rooms and large public areas and outdoor dense urban ultra-high-rate hot-spots, high-rate areas and larger areas. Since P2P and PMP scenarios are anticipated for backhaul and front haul including mobility, self-backhauling and relaying, the following link types need to be taken into account: backhaul BS-BS, front haul BS-BS, access BS-UE and D2D link UE-UE. Link topologies to be measured are outdoor to outdoor (O2O) and outdoor to indoor (O2I). Amongst measurement set-up parameters are for transmitter and receiver: distance, antenna height, location and velocity.

The propagation channel model in particular for MiWEBA has to address the following challenges:

- LSO and NLOS PL model for frequency range 57 - 66 GHz
- Shadowing
- Spatial consistency, environment dynamics
- Very large antenna arrays (spherical wave modelling)
- Dual mobility Doppler model for D2D
- Frequency dependency of propagation channel model parameters due to low amount of available measurement campaign data
- Ratio between diffuse and specular reflections
- Polarization

Propagation channel model parameterization challenges are the estimation of large scale parameters (LSP) like delay spread (DS), angular spreads (AS), Ricean K

factor (K) and shadow fading (SF) as well estimation of small scale parameters (SSP).

Simulation and implementation challenges are complexity, performance and availability.

1.2 Relation to other work packages

D1.1. (scenarios and use cases), focusing on the definition of a set of requirements for the traffic and propagation models and on a generic use case description close to the environment deployment and appropriate applications and services provided by the telecommunication operators, guides the analysis of the specific technical solutions in particular the channel modelling and characterization in this work package. For example front hauling as well as backhauling links, based on mmWave technologies, are proposed due to their flexibility and scalability in addition to access. Two basic access scenarios for indoor mmWave communications are suggested with isolated rooms and large indoor public areas. As outdoor coverage access scenarios are recommended ultra-high-rate hot-spots, high-rate areas and larger areas. Several P2P and PMP scenarios are anticipated for backhaul and front haul including mobility, self-backhauling and relaying. Five main use cases are proposed which are indoors dense hotspot (in shopping mall, enterprise and home environment), indoor/outdoor hotspot (in a square, urban) and outdoor non-hotspot (mobility, backhauling and front hauling in both dense urban and metropolitan areas).

D1.1. recommends to put a strong focus on mmWave outdoor propagation channel modelling and characterization and to take into account the simulation requirements of WP4 (supporting T4.1 system level simulation of mm-Wave overlay HetNets and T4.3 dynamic deployment activation and cell structuring) and WP5 (T5.2 highly-directional steerable mm-wave antennas development, T5.3 assessing beam steering and MIMO techniques). Results of D5.1 will be used to evaluate the performance of the mm-wave backhaul and access PHY used in T2.2 PHY/MAC interfaces to perform multi-RAT backhauling schemes and T3.2 mmWave link design and optimum integration of traffic and services.

D1.3 (development of business models) shows in chapter “regulation overview concerning spectrum around 60 GHz” exemplary that spectrum regulation is not harmonized globally regarding band allocations, allocation and power values and needs to be addressed further in regulation and taken into account in the continuation of this project.

Even if the ultimate goal for an mmWave channel model is to define continuous functions for all channel model parameters and propagation effects for the full frequency range, scenarios and use cases it could be that channel models might differ according to a large number of different scenarios and use cases. Therefore a tight interaction between WPs is established.

1.3 Structure of the document

This report contains results of the Work Package 5.1 “Channel modeling and characterization” for mmWave communication links. Chapter 2 gives an overview of most current mmWave experimental measurements and channel models. The scenarios and environment measurements in order to provide the necessary input data for deriving the model parameters are described in chapter 3. A new hybrid

methodology for mmWave channel models development is explained in chapter 4. Finally chapter 5 provides a 3D channel model for mmWave at 60 GHz and chapter 6 offers conclusions.

2 Overview of mmWave experimental measurements and channel models

2.1 Review of available experimental measurement results

This chapter presents a literature review (BROADWAY, EASY-C, METIS, COST, NYU Wireless, etc.) on measurements or propagation channel models in outdoor urban environment for terrestrial mobile services at frequencies higher than 6 GHz. The chapter does not address the terrestrial fixed wireless systems or satellite systems. Rain effects, vegetation attenuation, human body shadowing, ray tracing, material permittivity or conductibility are also not investigated in this chapter. Frequencies above 6 GHz may be divided in two groups: the millimeter wave (mmWave) frequency band above 10 GHz and the sub-mmWave frequency band below 10 GHz. This threshold is not based on the rigorous wave length but corresponds with a pragmatic classification of propagation papers.

2.1.1 Propagation channels for frequencies below 10 GHz

For frequencies below 10 GHz, the measurement scenario and especially the antenna configuration do not change. The TX antenna is omnidirectional or sectorial, the RX antenna is omnidirectional. The channel metrics such as the path loss or the impulse response are very little dependent on the antenna configuration and takes into account the greatest part of the multi-paths. The available results do not show a clear dependence of the delay spread or azimuth spread with the frequency [9]. The available results indicate a clear dependence of the path loss with the frequency. In free space, the theoretical correction factor is 20*log(f), f being the frequency. In urban environment with multi-paths generated by reflection or diffraction, the frequency correction factor is somewhere between 20 and 30*log(f) as indicated by the table below.

Table 2-1: Frequency correction factor in urban environment with multi-paths generated by reflection or diffraction

Model	Function	Validity domain
COST 231- WI [10]	$30*\log_{10}(f)$	800 / 2000 MHz
Hata [11]	$26*\log_{10}(f)$	400 / 1500 MHz
COST231-Hata [12]	$33*\log_{10}(f)$	1500 / 2000 MHz
Winner [13]	$23*\log_{10}(f)$	2/6 GHz
ITU UMa [14]	$20*\log_{10}(f)$	2/6 GHz

Reference	Function	Carrier frequency
Orange meas.	$27*\log_{10}(f)$	840 / 2200 / 3600 / 5100 MHz
Kitao [15]	$[23.8-1.4\log10(h_b)]*\log_{10}(f)$	460 / 810 MHz 2.2 / 3.35 / 4.7 / 5.2 / 8.45 GHz
Yonezawa [16]	$23*\log_{10}(f)$	820 MHz 5 GHz / 8.45 GHz
Sakawa [17]	[23 h_b = 55 m or 26 h_b = 10 m]$*\log_{10}(f)$	3.35/8.45/15.75 GHz
Oda 2001 [1]	$20*\log_{10}(f)$	460 MHz 2.2 / 4.7 / 8.45 / 15.75 GHz
Riback [18]	[30 f<900 MHz or 23 f>900 Mhz]]$*\log_{10}(f)$	460 / 880 / 1900 / 5100 MHz

Figure As a first assumption, channels above 6 GHz and below 10 GHz can be considered as an extension of current channel models at frequencies below 6 GHz such as WINNER or ITU channel models. Some measurement campaigns would be beneficial especially at frequency around 10 GHz to validate this assumption.

2.1.2 Propagation channels for frequencies above 10 GHz

Although mmWave have attracted much attention in the last years [19] [20] as mmWave are a candidate for the 5G wireless mobile system, the propagation channel analysis at mmWave frequencies in outdoor environment started before 1990. For instance, [21] [22] [23] [24] presented results around 60 GHz in urban or suburban environment. They observed reflected paths attenuated by 10-15 dB compared to the LOS path and delayed with a few ns. The analysis focused on the narrowband properties of the propagation channel including rain attenuation and oxygen absorption. More recently, [25] [26] [27] [28] presented measurement in Helsinki in E-band. Measurements were carried out in LOS conditions with highly directive antennas (24 or 45 dB). Although the LOS configuration and the high antenna directivity, multi-paths reflected on street walls were found but were attenuated by 20 dB compared to the LOS component. All of these papers were not dedicated to the directional properties at BS and MS, which are key parameters as the 5G system should use directive antenna at both link ends. Consequently, they are not described in details in the survey.

The literature review highlights results coming from measurement campaigns performed in Austin at 38 GHz and 60 GHz and in New-York at 28 GHz and 72 GHz. Reference [29] summarizes the different measurement campaigns. Reference [30] summarizes measurement campaigns in New-York and proposes a very wide literature review on mmWave systems including issues on propagation channel, antenna, RF component, performance estimation, etc. All the measurements used a similar device and procedure. The impulse response was measured by a sliding correlation channel sounder. The null-to-null analyzed bandwidth was 800 MHz. Both at BS (channel sounder TX) and MS (channel sounder RX), directive antennas transmitted and received the signal. The 3 dB antenna aperture was less than 10

degrees with an approximate gain of 25 dBi depending on the frequency. The directive antennas were mounted on 3-D rotating heads set on a tripod. The measurement procedure was specific for each measurement campaign but it consisted basically in two steps: first the BS and MS antenna orientations giving the maximum power were searched. Second, the BS antenna orientation and MS elevation were slightly changed around the maximum power direction (typically +/- 20 ° in azimuth or elevation) in order to find secondary paths. For each new BS antenna orientation or MS elevation, the channel was scanned over a 360° azimuth range at MS. This procedure did not guarantee that all paths were detected but most of them were probably detected. Distance between BS and MS was a few hundred meters but interesting results are given for distances less than 200 meters as the equipment was not able to measure attenuation higher than 150 dB/160 dB. Results related to the LOS configuration are not reported in this document as they agreed with the theoretical free space loss

Note: The definition of NLOS is sometimes very ambiguous. Usually the acronym NLOS is used to design situations when the BS has no optical visibility with the MS. In references [21-34], NLOS characterizes situations when the BS antenna and RX antenna are not aligned. It means that for each MS locations, several PL can be defined, one per BS-MS antenna orientation where power were detected. The definition of path, beam, lobe, cluster, peak is confusing too as there are not clearly defined except in one of the latest paper [31]. It is not straightforward that the same definition was used in all papers. From the understanding of the reader, it seems that the word path is often used to characterize specific direction of the MS and BS directive antenna where a power peak is detected (equivalent to a beam combination).

2.1.2.1 P2P measurement in Austin campus at 38 and 60 GHz

At 60 GHz, the NLOS PL ranged from 128 and 138 dB for BS-MS distances between 20 and 130 meters. The attenuation of secondary paths was between 15 and 40 dB higher than the free space. Around 5 secondary paths were found. At 38 GHz, the NLOS PL ranged from 113 dB and 145 dB. Paths are located around the line of sight with a +/-50° maximal azimuth deviation. The mean DS at 60 GHz is 7 ns (max 26 ns), at 38 GHz, the mean DS is 24 ns (max 120 ns) [32] [33].

2.1.2.2 Cellular measurement in Austin at 38 GHz

At these campaigns [34] [35] [36] [37] the TX antenna was at three antennas heights (8/23/36 m). The RX antenna directivity was either 8° (25 dBi) or 50° (13 dBi gain). NLOS path were between 10 and 30 dB weaker the LOS component. Partially obstructed LOS (vegetation, light diffraction) paths were 5 to 15 dB above the free space. A comparison with the environment showed than the secondary paths are created by reflection or low angle diffraction. Paths at BS are concentrated around the main direction (+/- 30°). The attenuation in cellular scenario is higher than the attenuation in peer-to-peer scenarios due to the 3-D distance and vegetation (thick foliage attenuates more than thin trunk). The NLOS PL is very little dependent with the distance. NLOS PL ranged between 125 and 145 dB with the 8° antenna. NLOS PL ranged between 115 and 130 dB with the 50° antenna between 40 m and 200 m.

The mean DS was 15 ns for both RX antenna configurations. 80 % of the DS were lower than 20 ns but maximal values raised up to 200 ns. Reference [38] proposes a path loss exponent less than 1 that illustrates the very small dependence of the path loss with the distance.

2.1.2.3 Measurement in New-York at 28 GHz and 72 GHz

At this measurement campaign [39] the antenna directivity was about 25 dBi and the BS antenna was set at three heights (7/17/40 m). At 28 GHz, the NLOS path attenuation is between 120 and 150 dB for a distance less than 50 meters. At distance above 50 meters, the NLOS path attenuation is between 130 and 165 dB. The path loss attenuation as a function of the distance is given by the equation $40*\log_{10}(d)+68$. The mean DS value is 40 ns and DS don't exceed 200 ns.

Compared to the averaged beam power (power with a specific TX and RX antenna orientation), the maximal beam power (best orientation) is 10 dB higher than the averaged beam power [40]. Combining coherently different beams (up to 4) can increase the power by 28 dB compared to the averaged beam power. No explanation is given on the combining algorithm applied to the measurement that could explain such a gain.

At 28 and 72 GHz, path can be grouped in about 3 or 4 clusters with an averaged azimuth spread of 10° [41]. The cluster seems to be defined as a group of paths in the angular domain. When 2 clusters exist, then the second includes 20 % of the total power. For an omnidirectional antenna (papers do not explain exactly how the omnidirectional data are deduced from the original data collected with directional antennas), the path loss is approximately 20/25 dB higher than the ITU UMi channels at 2 GHz and the following path loss model are given: at 28 GHz, $72+29.2*\log_{10}(d)$ and at 73 GHz, $86.6+25.5*\log_{10}(d)$. The standard deviation of the shadowing is between 8 and 9 dB.

Reference [42] focuses on penetration values at 28 GHz. For instance, outdoor tinted glass attenuates the signal by 40 dB whereas an indoor clear glass adds only 4 dB. The attenuation due to the brick wall (pillar) is 28 dB. The average penetration value is about 40 dB.

3 MiWEBA scenarios and environments

Work Package 1 "Scenarios and Use Cases, Architectures and Business Models" deliverable D1.1 "Definition of Scenarios and Use Cases access and backhauling and front hauling scenarios" proposes to explore separately access and backhaul/front-haul scenarios. The access scenarios are indoor, outdoor and multi-RAT HetNet. The backhaul/front haul scenarios are P2P/PMP and mobile multi-hop relay node.

Suggested exemplary indoor access environments are with isolated rooms (exhibition hall, office open space) and large indoor public areas (hotel lobbies, malls, shopping centers, sport facilities, airports, and railway stations, underground). Proposed exemplary outdoor access environments are ultra-high-rate hot-spots, high-rate areas and larger areas. Additionally a multi-RAT HetNet access environment has been recommended

to address the example of licensed and unlicensed spectrum use for indoor access. Several technical proposals are there for backhaul/front haul P2P/PMP (self-backhauling, adaptive and active antenna combined with mobility and locations) and mobile multi-hop relay node (MMR topologies and COMP MIMO processing, multi relay nodes).

D1.1 recommends to focus on outdoor environments and sees the following channel model parameters as important for the access PL, AoA distribution, DS, blocking margins (caused e.g. by passing pedestrians) and foliage attenuation.

3.1 MiWEBA access scenarios

3.1.1 Open area (University campus)

The outdoor access larger area environment example is chosen as a university campus scenario. This scenario describes a mix of use cases including data transfer between UEs and one or more BSs placed at campus' lampposts.

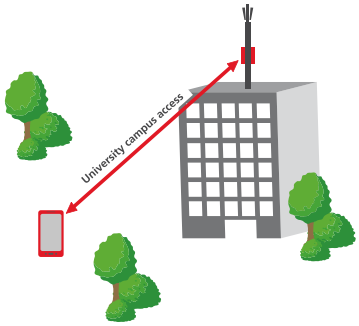

Figure 3–1: Open area (university campus)

3.1.2 Street canyon

The outdoor access ultra-high-rate hot-spots environment is represented by a street canyon street level urban scenario with a mix of use cases including data transfer between UEs and BSs placed at lampposts along the street.

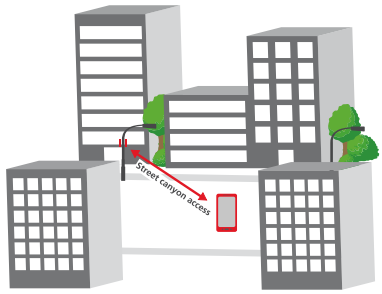

Figure 3–2: Street canyon access scenario

3.1.3 Hotel lobby

The Hotel lobby scenario is exemplary for the indoor access large public area environment assuming a mix of use cases including data transfer between stationary and nomadic UEs connected to BS placed near the hall ceiling.

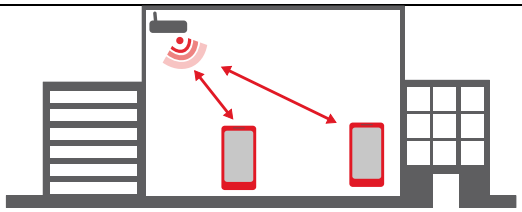

Figure 3–3: Hotel lobby scenario

3.2 MiWEBA backhaul/ front haul scenarios

3.2.1 Above Roof Top (ART)

The above roof top scenario is used as an example for the outdoor backhaul P2P environment using mmWave backhaul links between APs placed at building roof tops.

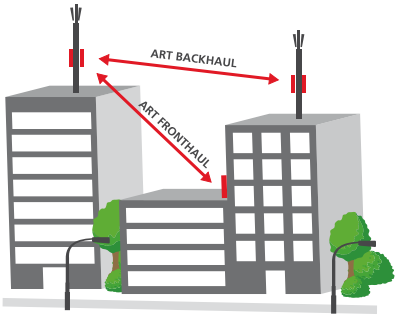

Figure 3–4: ART Backhaul and ART Fronthaul scenarios

3.2.2 Street canyon

The outdoor front haul P2P/P2M environment is represented by a canyon street level urban scenario. This scenario assumes a mix of use cases including data transfer between stationary, nomadic and mobile UEs and BSs placed at the roof top of surrounding buildings.

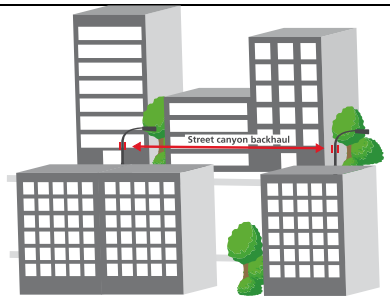

Figure 3–5: Street canyon backhaul scenario

3.3 MiWEBA Device to device (D2D) scenarios

3.3.1 Open area D2D scenario

The D2D interoperation may be organized in the outdoor area environment (university campus, see Figure 3–6). The Open area D2D scenario describes the data transfer between the UEs in the area.

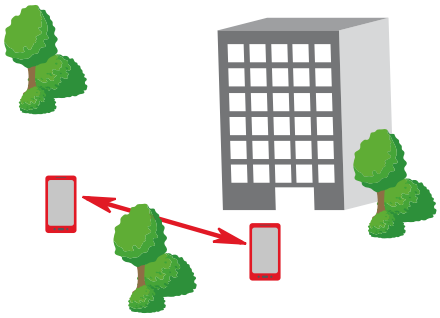

Figure 3–6: Open area D2D scenario

3.3.2 Street canyon D2D scenario

The Street canyon D2D scenario describes the direct data transfer between the UEs on the street, without the AP intermediation (Figure 3–7).

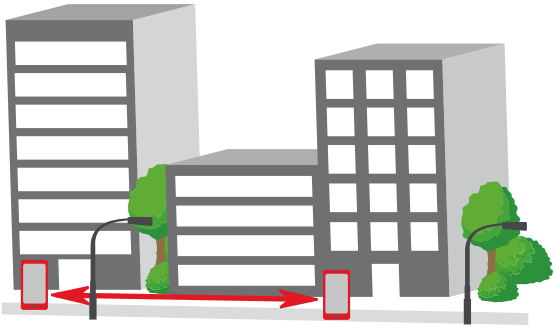

Figure 3–7: Street canyon D2D scenario

3.3.3 Hotel lobby D2D scenario

The Hotel lobby D2D scenario describes the direct data transfer between the UEs in the indoor environment, without the AP intermediation (Figure 3–8).

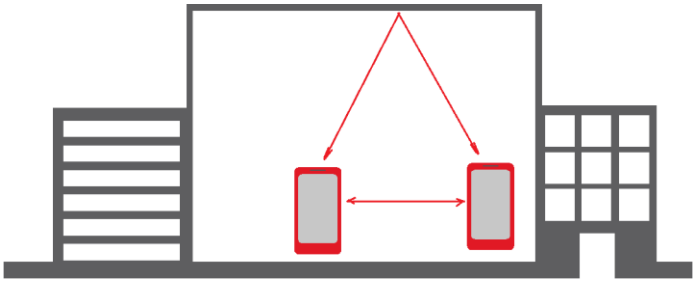

Figure 3–8: Hotel lobby D2D scenario

4 MmWave channel experimental measurements results and ray tracing modelling

A number of different scenarios have been defined as reference scenarios in the deliverable D1.1. As described in section 2 of this document the mmWave indoor channel has been under intensive research in the last years. Channel parameters and models for indoor applications can therefore be derived from literature.

The outdoor channel on the other hand is not yet well understood, when leaving unblocked line-of-sight connections aside. The outdoor access channel as described in the scenarios "Ultra high-rate hot-spots" and "High-rate areas" are the most challenging environments with very little reported knowledge. Therefore task 5.1 focus on the outdoor street canyon scenario.

Large scale measurement campaigns on a large number of sites that were done for the legacy cellular mobile frequency bands were outside of the scope of MiWEBA. To proof the feasibility of millimeter-wave outdoor access and to derive key performance numbers a hybrid approach has been selected. Based on the knowledge of the indoor propagation conditions the millimeter-wave frequencies exhibit much more "optical" behavior than the lower legacy frequency bands. Therefore ray tracing simulations can accurately predict the propagation paths. Simulations can easily be run on a large scale basis without the high effort of measurement campaigns. In this task we therefore chose a hybrid approach of combining ray tracing simulations with real world measurements. The ray tracing simulations are parameterized and verified with measurements on the same scenarios. In the following sections the measurements and the ray tracing simulations are detailed.

4.1 Experimental measurements with omnidirectional antennas

This section describes the experimental measurements and results that have been performed by the project partner HHI as a basis for the outdoor access channel model.

4.1.1 Experimental setup description

The urban access small cell scenario was selected for the measurements. The Potsdamer Straße in Berlin, Germany, was chosen as measurement environment. It is a street canyon of 51.5 meters width as can be seen in Figure 4–1. The buildings on both sides are of modern type with mixed glass and stone facades. There are three car lanes per direction that are separated by a pedestrian walkway. Medium sized trees

(around 4 to 5 meters) and street furniture such as bus stops, bicycle stands and seats are placed on the sidewalks.

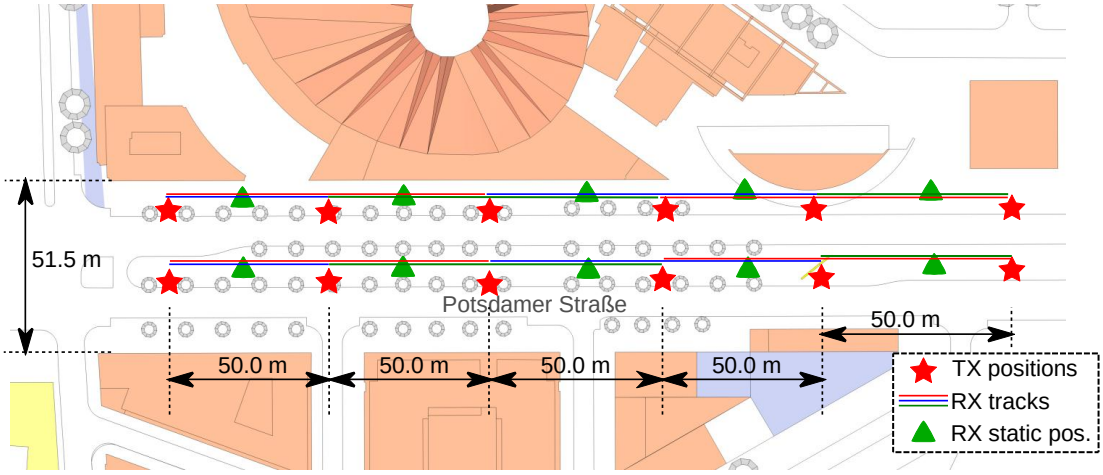

Figure 4–1: Outdoor access measurement scenario

The transmitter was placed on several locations at the edge of the sidewalk, aligned to existing lamp posts as indicated in the Figure 4–1. The transmit antenna was mounted on a tripod at a height of 3.5 meter to represent a typical position of small cells being added to existing street furniture. The receiver was mounted on a mobile cart with an antenna height of 1.5 meter to represent a mobile handheld user device. Multiple measurements were performed at static receiver positions 25 meters separated to the transmitter as indicated. Mobile measurements were conducted as well, where the receiver was moved at a constant speed on a straight line on the sidewalk, passing the transmitter up to 50 meter to each side.

The measurement system itself is based on a self-developed FPGA platform [43]. The key parameters are listed in Table 4-1. One measurement run contains 62,500 snapshots and took 50 seconds. During the measurement campaign a total of 3.75 million snapshots have been recorded with the mobile receiver, and 2 million snapshots have been recorded at static positions. The usage of omnidirectional antennas at both the transmitter and receiver side is very important to gather comprehensive results in the chosen time variant environment.

Table 4-1: Channel sounder parameter

Type	**Value**
Frequency	60 GHz
Bandwidth	250 MHz
Output power	15 dBm
Snapshot measurement duration	64 µs
Temporal separation of snapshots	800 µs
Antenna gain	2 dBi
Antenna pattern	Omnidirectional

Maximum instantaneous dynamic range	45 dB

The measurement environment is also available as a detailed three-dimensional computer model. This model can be used to repeat the measurements with a ray tracing tool. Spatial information on the propagation environment can then be found by matching the simulated paths to the measurement results on the propagation delay axis. The limited measurement bandwidth can then also be neglected as the ray tracing results are generally frequency-independent. This procedure permits a complete view of the time variant 3D mmWave propagation environment that can serve as a basis for the generation of valid channel models.

4.1.2 Main results

The primary output of the channel sounder is a channel impulse response (CIR) for each measurement snapshot taken every 800 µs. This CIR shows the delay and magnitude of each multi-path component (MPC) reaching the receive antenna. As the transmit and receive antenna have almost omnidirectional radiation patterns, no spatial filtering of the MPCs occurs. An exemplary plot of 100 snapshots of the CIR with static transmitter and receiver is shown in Figure 4–2: Example of channel impulse response for static setup. The delay of the first MPC is approximately 83 ns, being caused by the 25 meter line-of-sight distance between transmitter and receiver. The following MPCs then form a limited but distinctive number of peaks. The channel length observed in all measurements is in the order of multiple hundreds of nanoseconds.

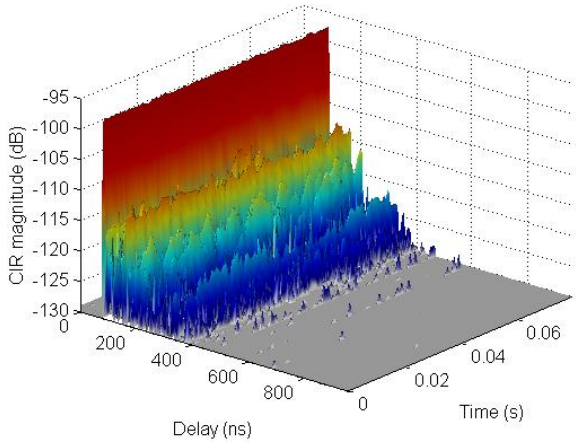

Figure 4–2: Example of channel impulse response for static setup

The following interpretation of the measurement results concentrates on these multipath components. It is important to note that the observed MPC at a certain delay can be caused by one or more waves arriving at the receiver from different angles of arrival, e.g. coming from different reflecting surfaces with the same total path length between transmitter and receiver. Due to the limited bandwidth of the measurement the CIR is susceptible to large and small scale channel effects.

4.1.2.1 Mobile Measurements

For the mobile measurements, the transmitter was placed at fixed locations and the receiver was moved along the sidewalk along a distance of 50 meter to each side of the transmitter. A number of 40 measurements with 62.500 CIR snapshots each, giving a total of 2,500,000 snapshots was used for the following analysis. An exemplary average power delay profile of a mobile measurement is shown in Figure 4–3.

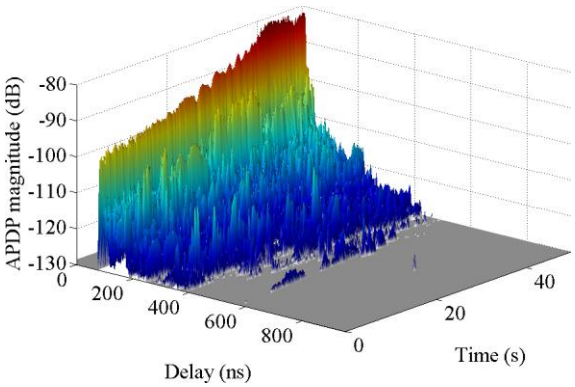

Figure 4–3: APDP of mobile measurement

The limited bandwidth of the measurement can cause fading effects on multipath components due to interference of multiple propagation paths with the same length. These fading effects can indeed be observed within the measured data. To circumvent problems arising from this effect the average power delay profile (APDP) was used instead of the CIR. The i-th APDP can be calculated from the CIR by

$$APDP_i = {}^{1}/_{N} \sum_{k=1}^{N} [CIR_{iN+k}(\tau)]^2 \qquad (4\text{–}1)$$

The APDPs shown here were generated with an averaging factor N set to 250.

Figure 4–4 shows the individual path loss for the five strongest multipath components of each APDP snapshot and linear regressions plotted against the line-of-sight (LOS) distance between transmitter and receiver. The different MPCs exhibit different path loss exponents, with the exponent of the strongest MPC being the largest. From the measurement setup it can be assumed that the strongest MPC in most cases was the LOS path. The increased variance towards larger distances can be attributed to higher chances of objects blocking this LOS path during the measurement.

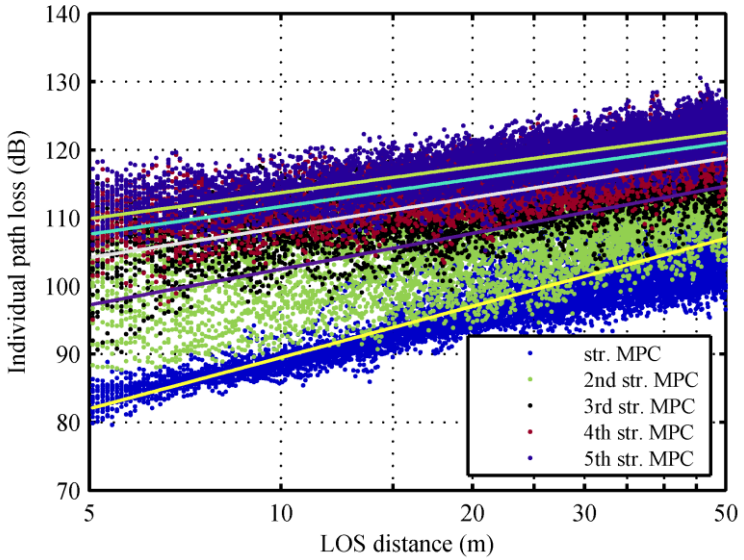

Figure 4–4: Individual path loss of multipath components

These path loss results were generated with omnidirectional antennas, as stated before. When directive antennas are taken into account, some of these MPC will amplified and others will be attenuated, depending on the antenna pointing and its radiation pattern. Assuming medium gain antennas at the transmitter and receiver (in the order of 20-25 dBi) the observed individual path loss, even for the MPCs besides the first one, would give a link budget allowing fast communication with standard OFDM schemes for example.

The statistical distribution of the individual path loss (PL) is shown in Figure 4–5. For every measurement snapshot the free space path loss is calculated from the known distance and subtracted from the individual PL. The cumulative distribution function then allows deriving the typical behaviour of the path loss in the propagation environment. The magnitude of the second strongest MPC for example is less than 13 dB weaker than the free space path loss in 50 % of the measured snapshots.

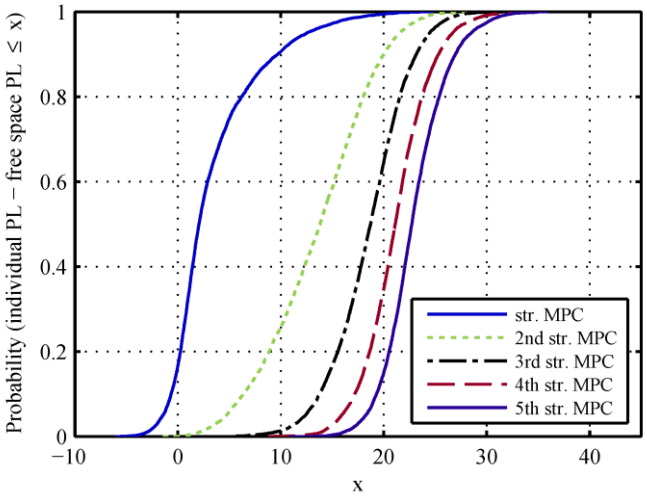

Figure 4–5: Empirical cumulative distribution function of MPC individual path loss

4.1.2.2 Static Measurements

The static measurements have been performed with stationary transmitter and receiver at a distance of 25 meter. Figure 4–6 shows 100 snapshots of the channel impulse response of such a measurement. As noted before, the first peak occurs at 83 ns delay, representing the delay caused by the 25 meter separation distance. The following peaks on the delay axis exhibit a strong time varying behaviour even in the small observation window shown.

A further analysis of the behaviour of the multipath components over the time axis becomes necessary. In each of the 62,500 snapshots of a measurement the two strongest peaks have been identified. Based on a histogram analysis of the position of these peaks, the four most frequent delays have been selected. The first of these delays belongs to the LOS path that was unblocked, at least most of the time, in all measurements.

The time evolution for one measurement of these four selected MPCs is shown in Figure 4–6: Time evolution of static measurement. To suppress small scale effects and focus on large scale behaviour, the average power delay profile was used as evaluation basis. The delays selected were:

$$\tau = \{83, 92, 105, 161\} \text{ ns.} \quad (4–2)$$

As can be seen, the magnitude of the first MPC is very stable while the magnitudes of the other three MPCs vary significantly over time.

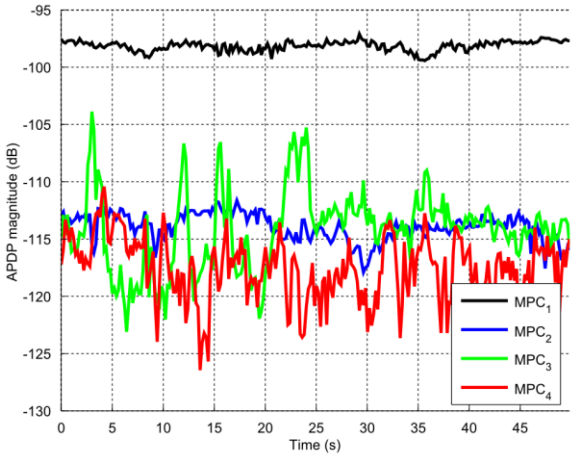

Figure 4–6: Time evolution of static measurement

Figure 4–7 shows the cumulative distribution function (CDF) of the four selected multipath components. The first MPC can be attributed to the line-of-sight path that was constantly present throughout the measurement, causing the steep transition of the CDF around its mean value. The same observation can be made for multipath component 2, indicating that it is caused by one or multiple static reflectors. The other two MPCs exhibit a more smooth transition indicating a stronger variation of their magnitude throughout the measurement.

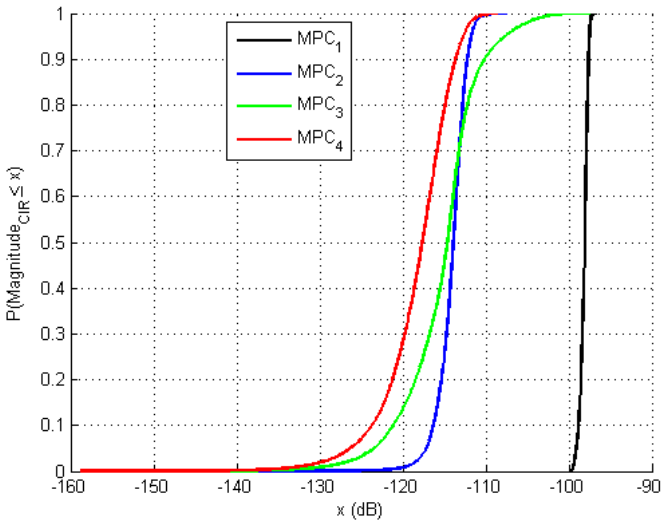

Figure 4–7: Empirical cumulative distribution function of MPC strength in static measurement

4.1.2.3 Human Body Shadowing

In the investigated mmWave street canyon outdoor access scenario the effects of pedestrians are very relevant [44]. They can temporarily block the line-of-sight connection between the terminal and the base station, thus severely affecting the received signal. Measurements have been performed where the transmitter and receiver were 50 meters apart. The transmit antenna was mounted at 3.5 meter height and the receive antenna was mounted at 1.25 meter height. A single or multiple persons then moved adjacent to the LOS path in the vicinity of the receiver, thus temporarily fully blocking the line-of-sight path. The line-of-sight multipath

component based on the channel impulse response for such a measurement is shown in Figure 4–8. The plot exhibits the typical behaviour of the LOS path that was previously described and modelled with the double knife edge model. The observed line-of-sight MPC attenuation during shadowing events is in the order of 10 to 15 dB on average but can increase up to 40 dB or more.

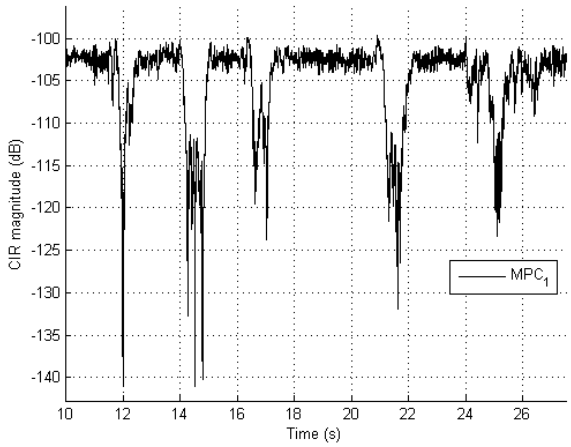

Figure 4–8: LOS multipath component under temporary human body shadowing

A more detailed plot of a single shadowing event is shown in Figure 4–9

Figure 4–9: Human body shadowing event. Additionally to the line-of-sight MPC (delay of 164 ns), two other multipath components with delays of 244 ns and 172 ns are shown. It can be seen that these MPCs are not affected when the shadowing event occurs. This indicates that the propagation paths associated to these MPCs arrive from different directions than the LOS MPC.

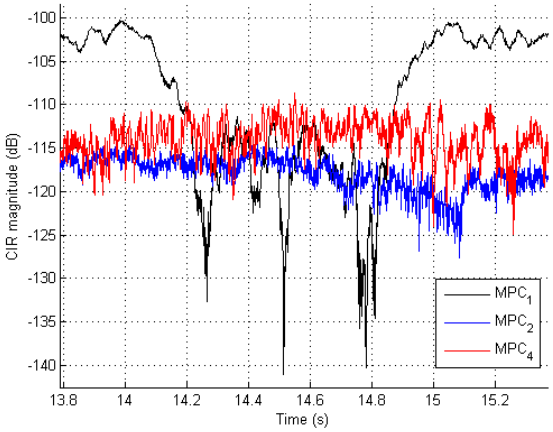

Figure 4–9: Human body shadowing event

4.1.2.4 Path loss parameters

Based on the measurement campaign a path loss model was derived. The derivation and the parameters of this model are described in section 5.9.1.

4.2 Broadband experimental measurements with directional antennas

This section describes measurement results carried out by the IMC project partner to investigate more in detail the effect of fast fading in broadband mmWave channel.

4.2.1 Experimental setup description

The open-space area (university campus) experimental scenario was used for that study. The general experimental measurement setup is shown in Figure 4–10. The transmitter (TX) antenna was mounted on the vestibule of the university campus building at the height of 6.2 m. The receiver (RX) antenna was mounted on a moving platform with an antenna height of 1.5 m.

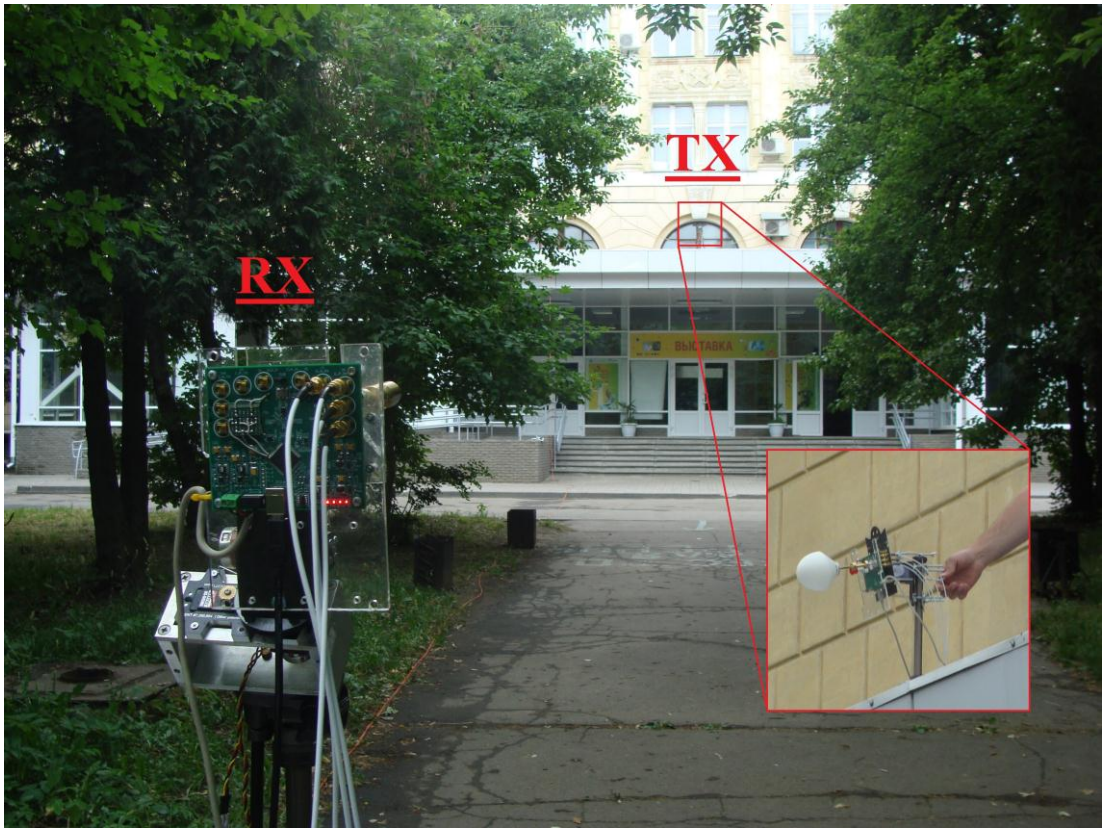

Figure 4–10: Snapshot of the university campus experimental scenario

A schematic illustration of this scenario is shown in Figure 4–11, where the following main parameters are used: D0 is the direct LOS distance between the TX and RX antennas; L0 is the horizontal distance between the transmitter and receiver, H1 and H2 is the height of transmitter and receiver, respectively.

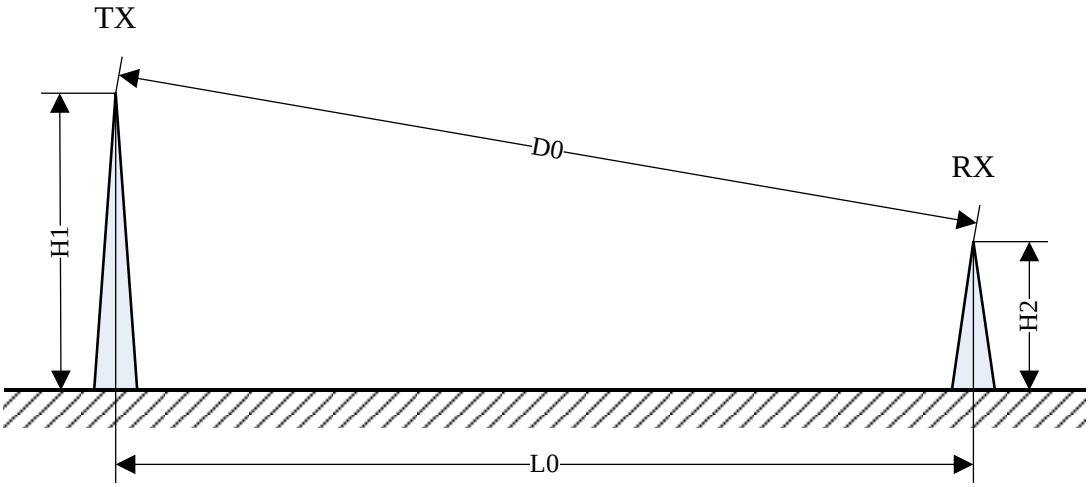

Figure 4–11: Experimental set up for studying the fast fading in broadband mmWave channel

For the experimental data acquisition and processing, a specially designed measurement platform was used with the key technical parameters listed in Table 4-2.

Table 4-2: Key technical parameters of the measurement platform developed to study the fast channel fading

Type	Value
Frequency	60 GHz
Bandwidth	800 MHz
Output power	2.4 dBm
Platform sensitivity	-75 dBm

It should be stressed that the sounding signal bandwidth used in these experiments was equal to 800 MHz which provided the highest time resolution of 1.25 ns. This is more than three times better than in the experiments with omnidirectional antennas described in previous section 4.1.

Depending on the distance L0, the transmitter was equipped with antennas of different gain (see Table 4-3). For distances less than 35 m the rectangular horn antenna 14×18 mm^2 with 19.8 dBi gain was exploited, for greater distances the highly directive lens antenna with large aperture (100 mm) and 34.5 dBi gain was used. The receiver were equipped with the round horn antenna with the diameter d = 14 mm and 12.3 dBi gain (see Figure 4–10).

Table 4-3: Key parameters of antennas used for the measurements

Type	Antenna gain	HPBW
Lens, d = 100 mm	34.5 dBi	3°

Rectangular horn 14×18 mm^2 (261E-20/387)	19.8 dBi	18° (H-plane), 14° (V-plane)
Round horn, d = 14 mm (QSH-14125D0)	12.3 dBi	30°

4.2.2 Main results

The use of directional antennas at both TX and RX assisted to discover that the considered experimental scenario was characterized by only two strongest propagation paths (or rays). The first path corresponded to the LOS component and the second path corresponded to the reflection from the ground (asphalt) surface. All other propagation paths caused by reflections from surrounding objects were more than 15-20 dB lower than these two strongest components.

For detailed investigation of the fast fading effects in broadband (800 MHz) mmWave channel caused by the motion of mobile user we should had minimized the impact of antenna patterns. To achieve that, the TX and RX antenna patterns had an initial orientation in 3D space to provide equal gains for the direct and reflected rays as illustrated in Figure 4–12. This configuration allowed keeping almost constant the amplitudes of the direct and ground-reflected rays during the motion of the receiver.

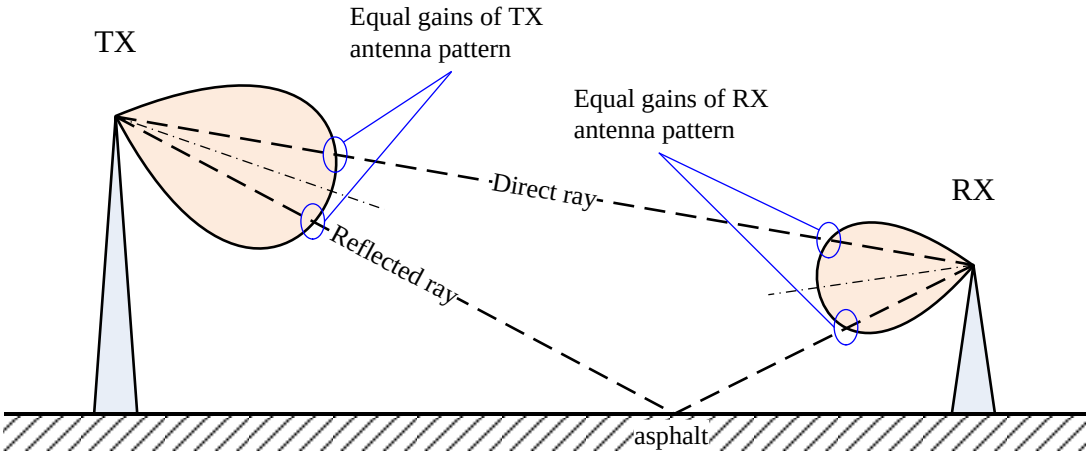

Figure 4–12: The orientation of TX and RX antenna patterns in the experimental scenario

An example of the measured channel impulse response with two clearly distinguishable peaks is presented in Figure 4–13. The peaks corresponded to the LOS and ground-reflected components are found 2.5 ns apart from each other. The power difference between those two peaks is approximately equal to the ground reflection coefficient (-6 dB). This is in line with the given scenario geometry where the horizontal distance between the transmitter and receiver is 30.6 m.

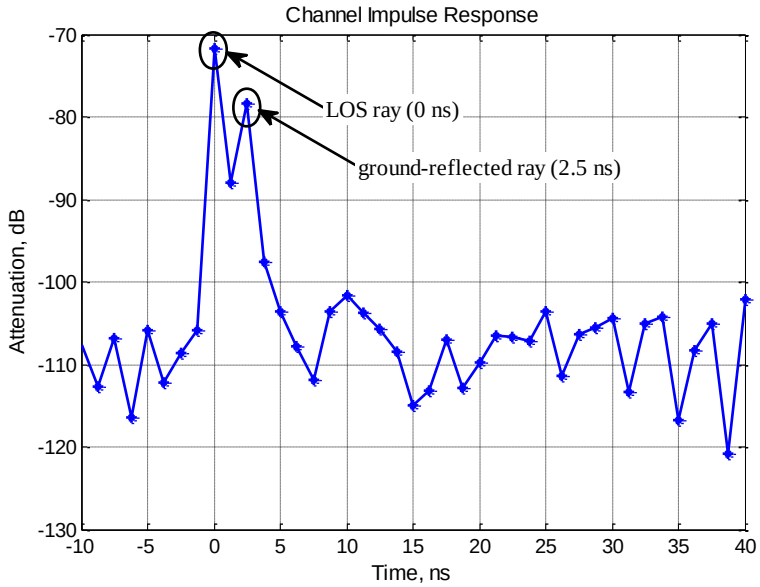

Figure 4–13: Channel impulse response, L0 = 30.6 m

Initially, the dependency of channel transfer function (CTF) on the RX vertical motion was investigated for distance L0 = 30.6 m. In Figure 4–14 the CTF of 800 MHz bandwidth is presented when the RX height changes from 1.34 m to 1.5 m. A few separate CTF samples are given in Figure 4–15. In these experiments the Horizontal-to-Horizontal (H-H) antenna polarization configuration was used at both TX and RX antennas. The measurements for other polarization configurations were also carried out, but the use of H-H configuration allowed us to exclude additional effects associated with the Brewster angle impact. As can be observed from the figures, the channel has high frequency selectivity in 800 MHz bandwidth. But the most important outcome from these results is the very fast variations of the mmWave channel when the RX height is changing. Just RX moving in the vertical direction by 2-3 cm produces significant variations of the channel.

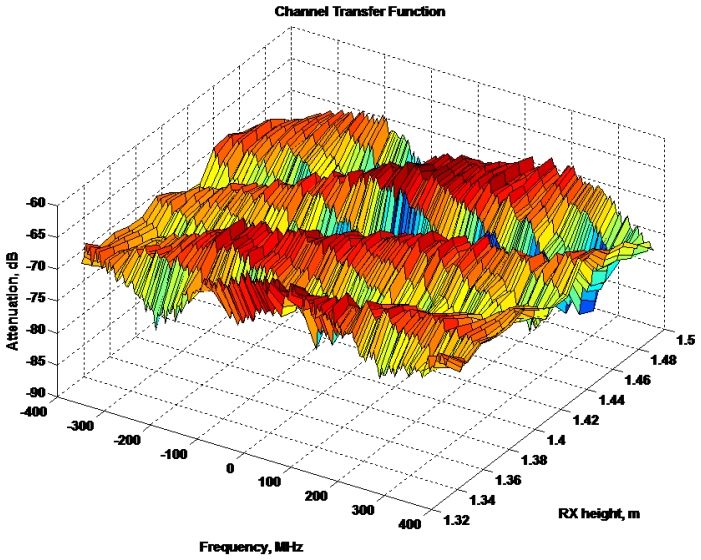

Figure 4–14: Scenario H-H, L0 = 30.6 m, H1 = 6.2 m. CTF dependency on the RX height H2

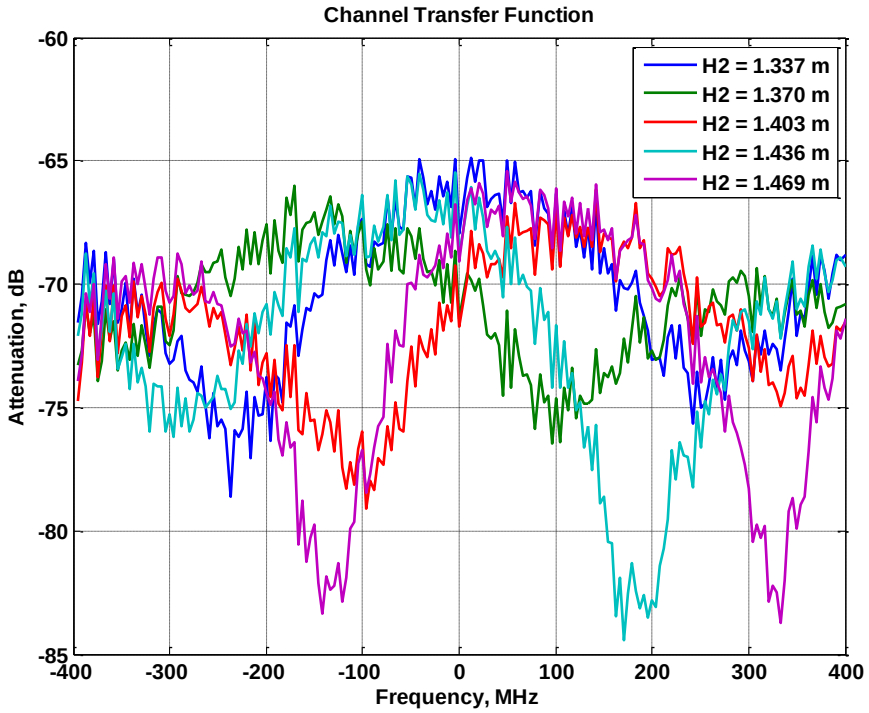

Figure 4–15: Scenario H-H, L0 = 30.6 m, H1 = 6.2 m. Sample CTFs for different RX heights

The dependency of CTF variations on the RX motion in the horizontal plane was also studied. In Figure 4–16 the CTF is presented when the horizontal distance between the TX and RX changes from L0 = 30.6 m to L0 = 31.6 m.

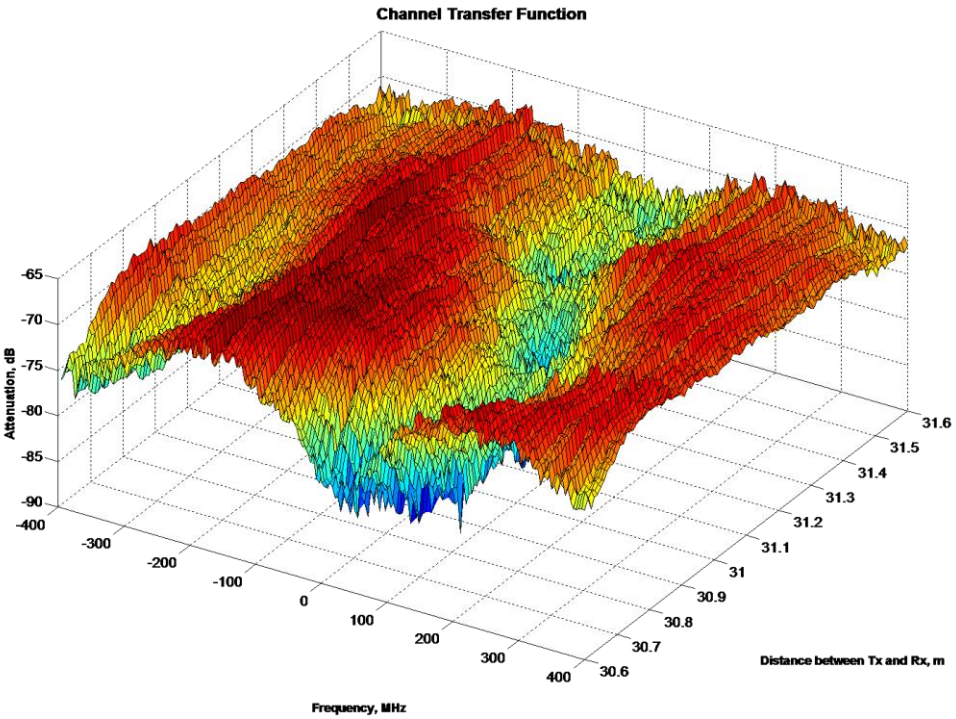

Figure 4–16: Scenario H-H, H1 = 6.2 m, H2 = 1.5 m. CTF dependency on the horizontal distance L0 between the TX and RX

Comparing these results with Figure 4–14, it can be seen that the horizontal motion of the mobile user has less impact on the CTF. The significant variations of the channel are observed only for distance changing about one meter for the considered system configuration.

The cross-polarization ratio (XPR) was also measured for the ground-reflected ray in the considered experimental scenario. For that purpose, orthogonal antenna polarization configurations were used at the transmitter and receiver. According to the obtained experimental results, the value of XPR was less than -25 dB.

Broadband experimental measurements with directional antennas have revealed the fine structure of the mmWave channel in outdoor open-area environment. It was identified that typical (not very high-directional) mobile user antenna will receive two rays (the direct LOS ray and the ground-reflected ray) with rather small time delay (2.5 ns for 30 m). It should be noted, that as the distance between the TX and RX sites increases, the time delay and angle of arrival between these rays decreases. The interference of the direct and the ground-reflected rays explains the fast fading effects observed in the experiments with omnidirectional antennas in Section 4.1 and should be addressed in the channel modelling methodology.

4.3 Ray tracing

To support the omnidirectional measurements and to generate a complete understanding of the spatial channel properties ray tracing simulations have been set up.

The measurement environment is also available as a detailed three-dimensional computer model. This model can be used to repeat the measurements with a ray tracing tool. Spatial information on the propagation environment can then be found by matching the simulated paths to the measurement results on the propagation delay axis. The limited measurement bandwidth can then also be neglected as the ray tracing results are generally frequency-independent. This procedure permits a complete view of the time variant 3D mmWave propagation environment that can serve as a basis for the generation of valid channel models.

4.3.1 Ray tracing approach description

The ray tracing tool was developed by Fraunhofer HHI. It relies on hardware accelerated operation on the graphics boards (GPU) [45]. This tool utilizes ray forward tracing and may use back tracing via the imaging method to efficiently and accurately compute the radio channel for a given scenario. The transmitter (TX) is modelled as a point source while the receiver (Rx) is modelled as a sphere with a radius according to the path length and the dimensions of the surroundings. Both are placed into the scene of the regarded 3D model.

The homogeneously distributed launching angles of the rays on the TX side are determined by minimizing the energy on the surface of a sphere according to the method of generalized spiral points. The launched rays are traced forward along occurring intersections until a receiver sphere is hit. All of those rays gather the indices of the intersected primitives to identify their path through the scene. The indices are then used to identify and delete duplicate paths to ensure the uniqueness of a single path. Those paths are then traced back via the imaging method. This is done by mirroring the TX at all surfaces on which the intersections of a single path occurred and tracing back the correct path starting from the RX side. This gets us the correct phase of the propagation path and also eliminates paths which are found to be irregular after the mirroring.

Although the ray approach leads inevitably to aliasing-effects (due to finite small solid angles for the ray launching), the parallelization advantage of the GPU allows us to launch a very large number of rays, resulting in a very high spatial resolution, yet costing few computation time. Launching for example 10,000,000 rays results in a solid angle of $1.1 \cdot 10^{-3}$ rad. As we concentrate our analysis on frequencies around 60 GHz resulting in 5 mm wavelength we have to assume that errors due to the aforementioned aliasing-effects may occur when modelling the propagation environment properly according to the wavelength. Nevertheless, this will only happen for very long path lengths. As those paths get highly attenuated first and foremost due to free space path loss and the reflection losses due to realistic material parameters we may still assume that simulations using the approach with OptiX will lead to accurate results. Previous measurements and simulations for indoor environments at 60 GHz have shown a good agreement between the ray tracing results and the measured channel [46].

4.3.2 Implemented scenarios and simulation results

As mentioned before the location that was used for the channel measurement is also available as a 3D model. This model was equipped with more objects, such as trees,

benches and street lights according to the environment at the time of the measurement campaign.

The dynamic nature of the busy outdoor environment however is challenging when setting up simulations. Cars and busses of different sizes and models drive by and pedestrians and cyclists pass along the sidewalks. Modelling these objects accurately is a very challenging task and goes far beyond the scope of this deliverable.

Figure 4–17: Exemplary set of receiver positions and rays and Figure 4–18: Exemplary set of receiver positions and rays (details) show an overview and a detailed view of a simulated track. The transmitter is placed to the right in Figure 4–18 and a series of receivers was placed on a linear track to the left in order to simulate a measurement run of 25 meters in parallel. As can be seen the line of sight path, the ground reflection and reflecting paths from objects to both sides are identified.

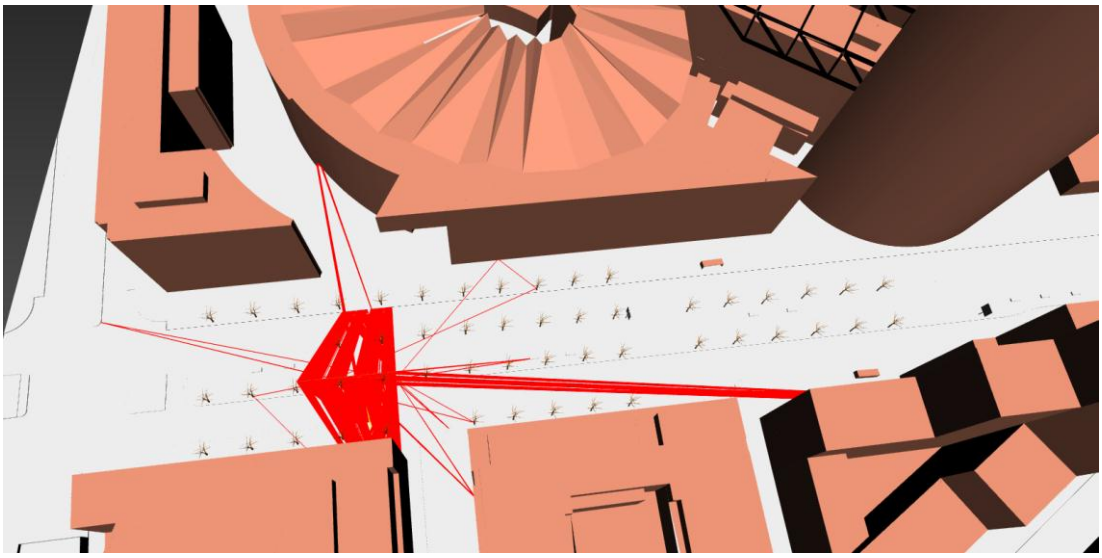

Figure 4–17: Exemplary set of receiver positions and rays

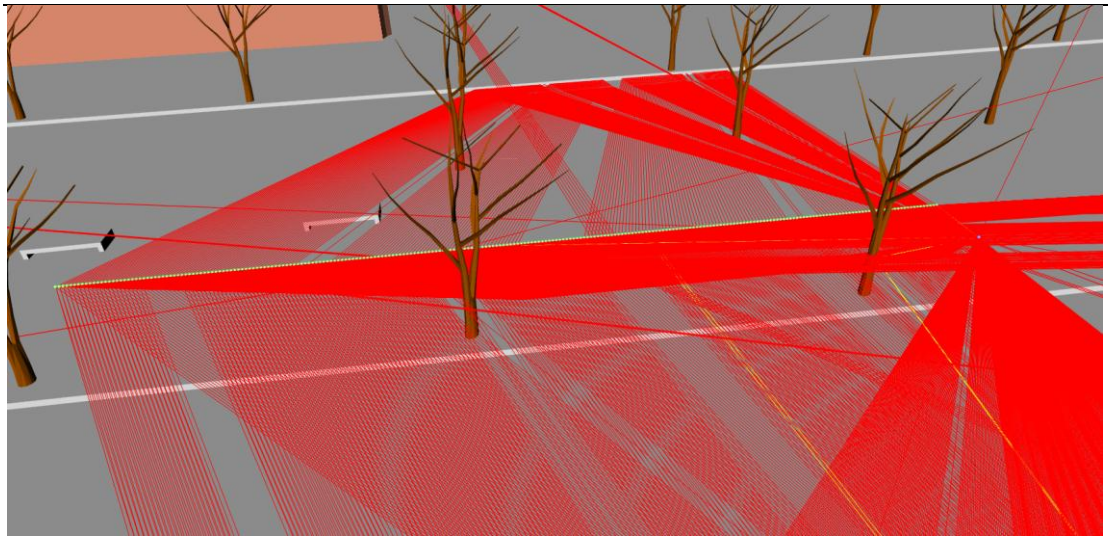

Figure 4–18: Exemplary set of receiver positions and rays (details)

The average power delay profile (APDP) from measurement and simulation are shown in Figure 4–19 and Figure 4–20. The APDP is calculated from the individual channel impulse responses (CIR) in order to eliminate small scale effects (fading):

$$APDP_i = \frac{1}{N}\sum_{k=1}^{N}\left[CIR_{(iN+k)}(\tau)\right]^2 \qquad (4\text{–}3)$$

The averaging factor N was chosen so that the spatial averaging is larger than the fading effects that can occur.

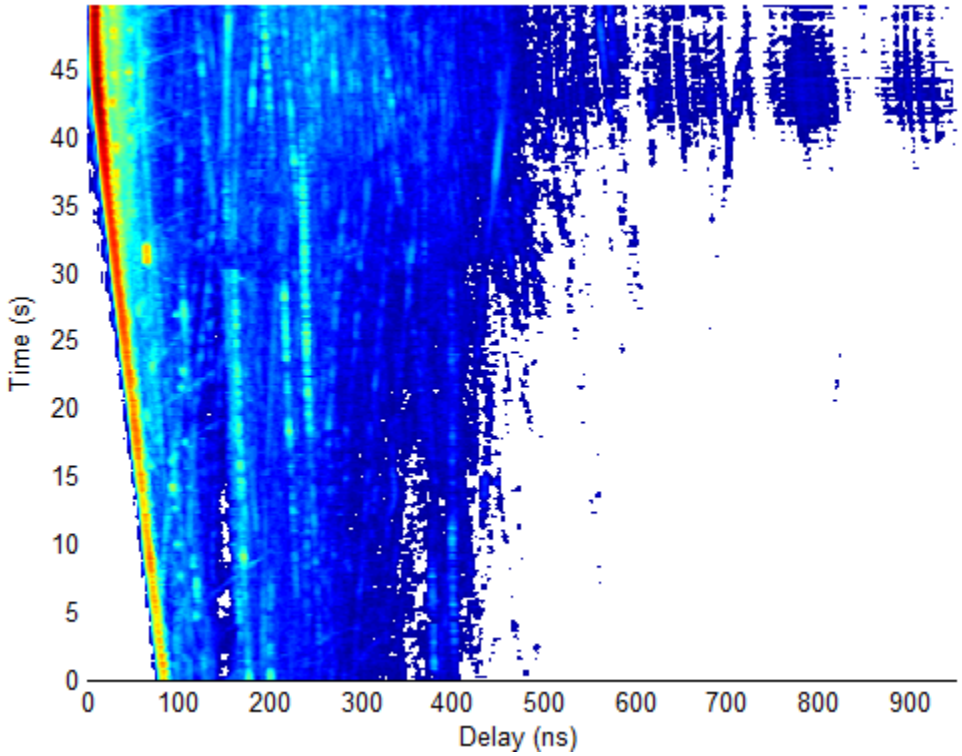

Figure 4–19: Measured APDP

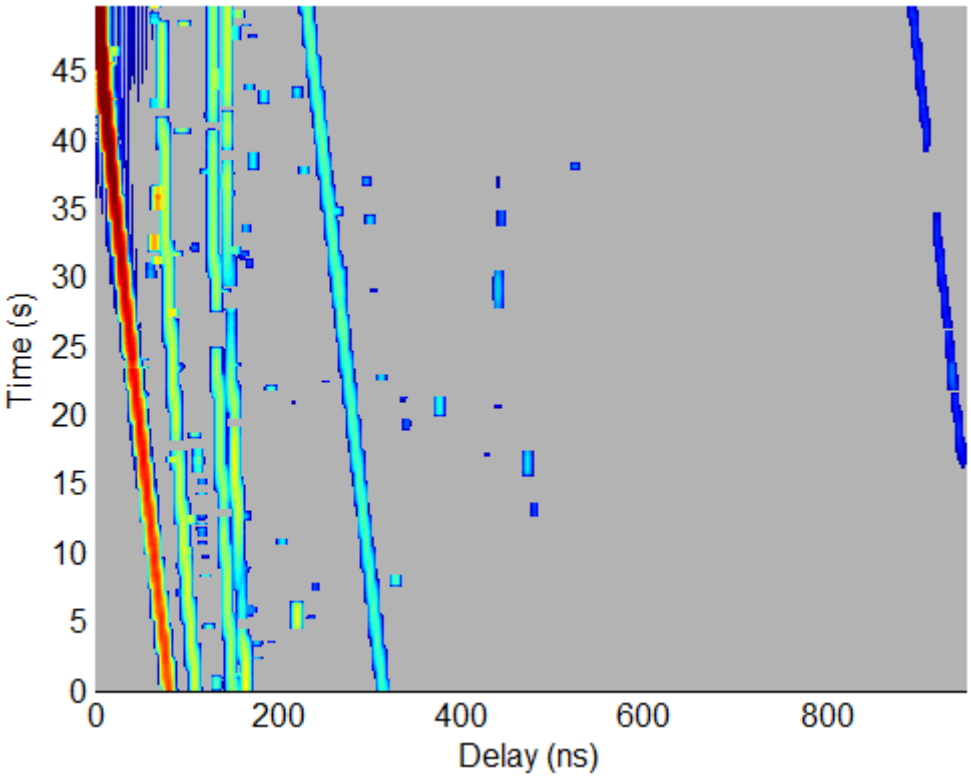

Figure 4–20: Simulated APDP

Comparing the simulated APDP with the APDP from measurement shows similar behavior on the strong line-of-sight multipath components. Most of the strong reflecting multipath components can also be identified. As mentioned before the dynamic nature of the environment has a visible impact on the measured APDP that is not present in the simulated one.

A verification of the simulated results was performed with a set of control measurements with a directional antenna at the receiver side that was rotated to identify reflection objects. Large static reflectors such as buildings were identified by the ray tracer without problems. Smaller, irregular objects, such as trees can be problematic as they produce measureable reflections. In the simulation they were not always identified due to their small size and discretization into discrete surfaces.

Within work package 5.3 the ray tracing model will be further refined and parameterized. It will then be used to gather information on the spatial distribution and the strength of the multipath components.

5 MiWEBA 3D Channel model

5.1 MiWEBA channel model requirements

Signal propagation in the bands traditionally used for wireless networking such as 2.4, 3.5 and 5 GHz is relatively well studied; a number of accurate and realistic modeling approaches exist, making possible both link level and system level investigation of communication systems working in that bands.

The millimeter-wave (mmWave) frequency band is less studied in this respect because it is less commonly used for multi-vendor networking, typically seeing less standardization efforts, and on the other hand due to certain difficulty in gathering representative signal propagation statistics, which is caused by several aspects. The 10x increase of the carrier frequency of mmWave systems in comparison with 2.4 GHz and 5 GHz legacy systems leads to qualitative changes of the signal propagation properties.

Firstly, small wavelength of the mmWave band results in significantly higher propagation loss (PL) according the Friis transmission equation. As a consequence, high directional transmit and receive antennas have to be used to compensate for the larger propagation loss to sustain operation over typical outdoor distances of up to several hundreds of meters. Support for mobile users requires the antennas to be electronically steerable. Hence, the channel model should take into account spatial (angular) coordinates of the channel rays at transmit and receive sides and also support application of any type of the antenna technology (i.e. non-steerable antennas, sector-switching antennas, antenna arrays).

Secondly, as confirmed by a number of works [4], [29], [33], [35], the 60 GHz propagation channel has a quasi-optical nature. The propagation due to diffraction is not significant and not practically viable. Most of the transmission power is propagated between the transmitter and the receiver through the LOS and low-order reflected paths. To establish a communication link, the steerable directional antennas have to be used pointed along the LOS path (if available) or one of the reflected paths. An additional consequence of the quasi-optical propagation nature is that image based ray tracing can be an effective means for prediction of spatial and temporal analysis of the channel paths and may be used to assist the channel modeling.

Thirdly, it should be noted that with ideal reflections, each propagation path would include only a single ray. However, as demonstrated by experimental investigations [43], [47], [48] each reflected path actually consists of a number of rays closely spaced to each other in the time and angular domains due to fine structure of the reflecting surfaces. Hence, the clustering approach is directly applicable to channel models for 60 GHz indoor WLAN systems with each cluster of the model corresponding to the LOS or NLOS reflected path.

Fourthly, another important aspect of the 60 GHz propagation that should be adequately taken into account in the channel modeling is polarization characteristics. As demonstrated by experimental studies with 60 GHz WLAN prototypes, the power degradation due to polarization characteristics mismatch between the antennas and the channel can be as high as 10-20 db. The physical reason for high polarization impact is that with application of high directional steerable antennas typically only one strong LOS or reflected component will be essentially used for signal transmission and even reflected signals remain strongly polarized at the receiver.

Summarizing the all above, the 3D channel model for mmWave band shall in particular:

- Provide accurate space-time characteristics of the propagation channel (basic requirement) for main usage models of interest;

- Support beam forming with steerable directional antennas on both TX and RX sides with no limitation on the antenna technology;
- Account for polarization characteristics of antennas and signals;
- Support non-stationary characteristics of the propagation channel.

5.2 Channel modeling methodology

State of the art mobile communications channel characterizations include separate description of the path loss models and spatial channel models, typically comprised of the clustered channel impulse responses and angular spread statistics [49]. Latest works for mmWave channel models also follow such approach [35] [50] [51] and apply different cluster analysis techniques to the experimental data. However, such approaches work well for NLOS conditions only, which is not the main usage case for the mmWave communication system. At the same time, the propagation loss specifics of millimeter-wave signals lead to the weakness of the distant reflections and dominance of the rays that are close to the direct path. This requires new approaches to characterize channel mobility and Doppler effects.

To provide adequate modeling of the channel propagation aspects mentioned above, the methodology of Quasi-Deterministic (Q-D) channel modeling is proposed and developed. Under this approach for each of the channel propagation scenario first, several strongest propagation paths (rays which produce the substantial part of the received useful signal power) are determined, and signal propagation over them is calculated based on the geometry of the deployment, locations of Base Stations (BS) and User Equipment (UE) in a deterministic manner. Signal power delivered over each of the rays is calculated in accordance to theoretical formulas taking into account free space losses reflections, polarization properties and UE mobility effects: Doppler shift and user displacement.

Some of the parameters in these calculations may be considered as random values (e.g., reflection coefficients) or even as random processes (e.g., UEs motion). It should be noted, that the number of such quasi-deterministic rays (D-rays), which should be taken into account, depends on the considered scenario. Depending on the considered scenario the number of the strongest rays may be different. In this respect, for outdoor open space scenarios it has been shown, that signal propagation properties are mostly determined by two D-rays – the LOS ray and the one reflected from the ground. For outdoor street canyon scenario the propagation is determined mostly by 4 D-rays – the LOS, the one reflected from the nearest wall and the one reflected from the ground and the nearest wall. For the hotel lobby (indoor access large public area) scenario more D-rays need to be modeled. For this scenario it is proposed to consider all rays with up to second order reflections as D-rays (in similar way as was adopted in the IEEE 802.11ad evaluation methodology for indoor scenarios.

In real environment, in addition to the strong D-rays a lot of other reflected waves are coming to the receiver from different directions. For example, there are cars, trees, lampposts, benches, far big reflectors as houses, etc. All these rays are considered in the Q-D channel models as secondary random rays (R-rays) and are described as random clusters with specified statistical parameters extracted from

available experimental data or more detail ray tracing modeling. The accuracy of the proposed approach is illustrated by its fit of analysis data to real experimental data.

The experimental measurements data for different open area (squares and broad street) environments shows that the channel may be well-described with the two-ray channel model, considering only the direct ray and first (ground) reflected ray. For example, Figure 5–1 depicts the experimental measurement results (provided by HHI, see chapter 4) versus two-ray model approximation. It can be seen that this simple model is in great coincidence with experimental data.

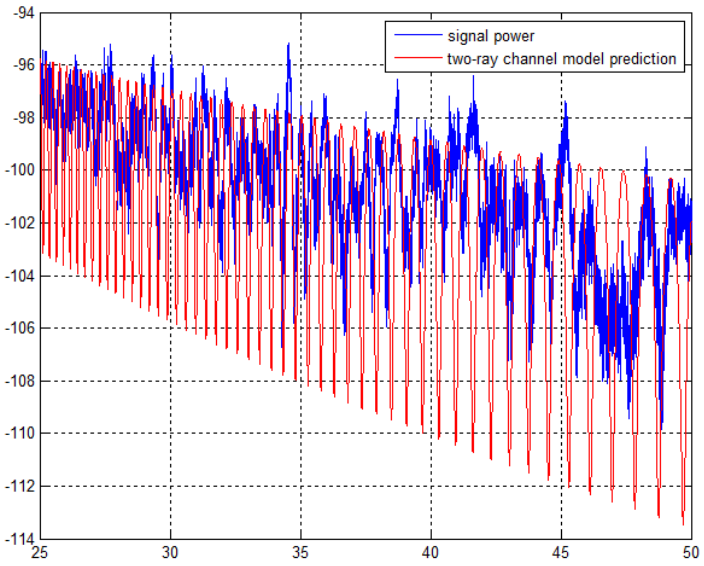

Figure 5–1: Fraunhofer HHI Street canyon experimental measurement results (blue) versus two-ray model results for same parameters

Another example, which presents the strong prediction capability of the proposed Q-D approach, is given in Figure 5–2. The figure shows one CTF realization from Figure 4–15, and the corresponding channel transfer function based on the two-ray model approximation.

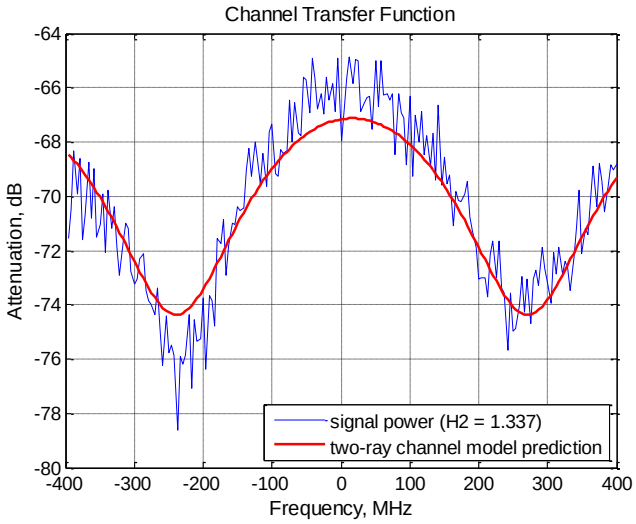

Figure 5–2: IMC open area experimental measurements results (blue) versus two-ray model prediction (red)

So, the combination of such deterministic approach with the statistical description of the random signal components is the key to meeting MiWEBA channel model requirements.

5.3 General structure of channel model

In the 802.11ad channel modeling document [4] the generalized description of channel impulse response is given by:

$$h(t,\varphi_{tx},\theta_{tx},\varphi_{rx},\theta_{rx}) = \sum_i A^{(i)} C^{(i)}\left(t - T^{(i)}, \varphi_{tx} - \Phi_{tx}^{(i)}, \theta_{tx} - \Theta_{tx}^{(i)}, \varphi_{rx} - \Phi_{rx}^{(i)}, \theta_{rx} - \Theta_{rx}^{(i)}\right)$$
$$C^{(i)}(t,\varphi_{tx},\theta_{tx},\varphi_{rx},\theta_{rx}) = \sum_k \alpha^{(i,k)} \delta\left(t - \tau^{(i,k)}\right)\delta\left(\varphi_{tx} - \varphi_{tx}^{(i,k)}\right)\delta\left(\theta_{tx} - \theta_{tx}^{(i,k)}\right)\delta\left(\varphi_{rx} - \varphi_{rx}^{(i,k)}\right)\delta\left(\theta_{rx} - \theta_{rx}^{(i,k)}\right) \quad (5\text{–}1)$$

where:

- h is a generated channel impulse response.
- t, φ_{tx}, θ_{tx}, φ_{rx}, θ_{rx} are time and azimuth and elevation angles at the transmitter and receiver, respectively.
- $A^{(i)}$ and $C^{(i)}$ are the gain and the channel impulse response for i-th cluster respectively.
- $\delta(\ )$- is the Dirac delta function.
- $T^{(i)}$, $\Phi_{tx}^{(i)}$, $\Theta_{tx}^{(i)}$, $\Phi_{rx}^{(i)}$, $\Theta_{rx}^{(i)}$ are time-angular coordinates of i-th cluster.
- $\alpha^{(i,k)}$ is the amplitude of the k-th ray of i-th cluster
- $\tau^{(i,k)}$, $\varphi_{tx}^{(i,k)}$, $\theta_{tx}^{(i,k)}$, $\varphi_{rx}^{(i,k)}$, $\theta_{rx}^{(i,k)}$ are relative time-angular coordinates of k-th ray of i-th cluster.

The generalized channel impulse response description may be rewritten in a more specific form, following the proposed semi-deterministic, semi-stochastic methodology. The channel impulse response can be represented as set of D-rays (direct ray, ground reflection, etc.) for which the power and angular characteristics

are directly calculated, and set of random rays, for which power and angular characteristics are generated in accordance with some specific to modelling scenario statistics. Note, that direct and first order reflection rays may also have some random components, to take into account reflection from the rough surfaces (for reflected rays) and partial blockage of one or several Fresnel zones for the LOS ray.

5.3.1 Deterministic rays (D-rays)

The quasi-deterministic rays are explicitly calculated in accordance with scenario parameters, geometry and propagation conditions.

5.3.1.1 Rough surface reflection

Important part of the proposed Q-D approach to the channel modelling is the calculation of the reflected ray parameters. The calculations are based on the method of images for determining the angular characteristics of the first and higher order reflections (see Figure 5–3) and on the Fresnel equations for calculation reflected rays power for different polarization components:

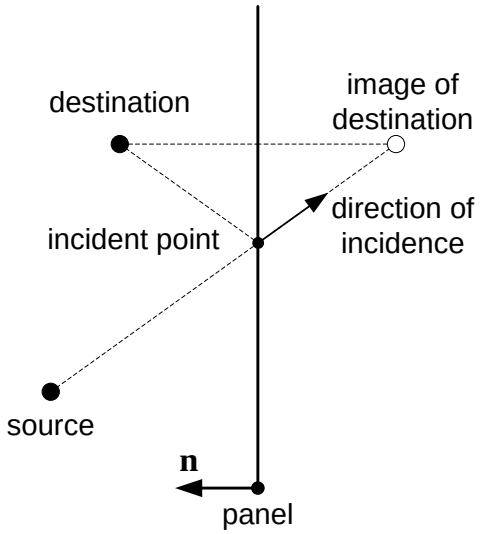

Figure 5–3: Method of images

$$R = 20\log 10\left(\frac{\sin\phi - \sqrt{B}}{\sin\phi + \sqrt{B}}\right), \qquad (5\text{–}2)$$

Where ϕ is the grazing angle and:

$$B = \varepsilon_r - \cos^2\phi \text{ for horizontal polarization}$$

$$B = \left(\varepsilon_r - \cos^2\phi\right)/\varepsilon_r^2 \text{ for vertical polarization}$$

However, the Fresnel equation describes only specular reflection from the ideal surface, while in reality most surfaces can be treated as “rough” comparing to the signal wavelength in accordance with Rayleigh roughness criterion [ITU Report 1008-1]:

$$g = 4\pi\sigma_h \sin\phi / \lambda , \quad (5–3)$$

where:

σ_h is standard deviation of the surface height about the local mean value within first Fresnel zone,

λ is the free-space wavelength,

ϕ is the grazing angle measured with respect to tangent to the surface.

The surface can be considered smooth for g<0.3. When the surface is rough, the reflected signal has two components: specular component which is coherent to the incident signal, the other is a diffuse component which fluctuates in amplitude and phase with a Rayleigh distribution.

For example, asphalt with surface deviations about 0.5 mm can be considered as smooth surface for grazing angle 10˚ (g = 0.2).

The specular component reflection coefficient is different from the one given by the Fresnel equations by constant multiplier: $R_s = \rho_s R$, where

$$\rho_s = \exp(-1/2\ g^2) \quad (5–4)$$

The feasibility of the proposed approach to the prediction of the signal power in outdoor microcell environments [52] and for intervehicle communication modelling [53]

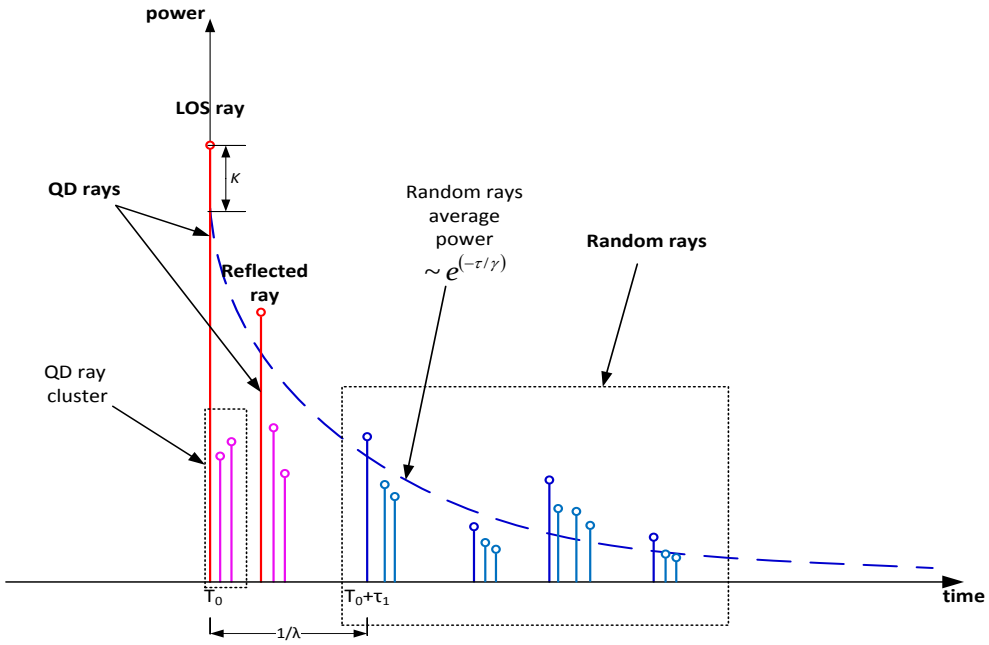

Figure 5–4: Channel impulse response structure

5.3.2 Random rays (R-rays)

In the proposed methodology some rays with lower power (reflected from far walls, random objects (cars, lampposts etc.) and second-order reflected rays are considered as secondary, and are described as random clusters.

5.3.2.1 R-rays power-delay profile

The clusters arrive according to Poisson process and have inter-arrival times that are exponentially distributed. The cluster amplitudes are independent Rayleigh random variables and the corresponding phase angles are independent uniform random variables over $[0,2\pi]$

The random rays' component of the channel impulse response (see Figure 5–4) is given by

$$h_{cluster}(t) = \sum_{k=1}^{N_{cluster}} \beta_k e^{j\theta_k} \delta(t-\tau_k), \qquad (5\text{–}5)$$

where τ_k is the arrival time of the *k*-th cluster measured from the arrival time of the LOS ray, β_k and θ_k are the gain and phase of the *k*-th cluster. The mean square values of the gain are given by

$$\begin{aligned} \overline{\beta_k^2} &\equiv \overline{\beta^2(\tau_k)} = \overline{\beta^2(0)} e^{-\tau_k/\gamma} \\ \overline{\beta^2(0)} &= \beta_{LOS}^2 - K \end{aligned}, \qquad (5\text{–}6)$$

where β_{LOS}^2 is the power gain of the LOS ray, K is the maximal ratio of LOS to NLOS component and γ is power-decay constant for the clusters.

τ_k is described by the independent interarrival exponential probability density function

$$p(\tau_k \mid \tau_{k-1}) = \lambda e^{-\lambda(\tau_k - \tau_{k-1})} \quad (5\text{–}7)$$

where λ is the random ray arrival rate.

The specific values of PDP parameters are defined in the channel models description sections per given scenario.

5.3.2.2 R-rays Angular characteristics

The angular characteristics of the random rays depend on the scenario and defined in corresponding sections. Typically, the azimuth and elevation components of the AoA and AoD have uniform distribution within pre-defined limits.

5.3.3 Intra-cluster structure

In additional to micro surface roughness, there may be larger irregular objects on the considered reflecting surfaces: road borders, manholes, stairs on the street, windows, advertisement boards on the walls, irregularities inside the reflecting surfaces, etc. Such additional reflections lead to the appearance of the additional rays with close delays and angles: a cluster. The mechanism of the cluster formation on the surface with large-scale irregularities is illustrated in Figure 5–5. It can be seen that the reflection from the rough surfaces additionally leading to spreading the signal by angle.

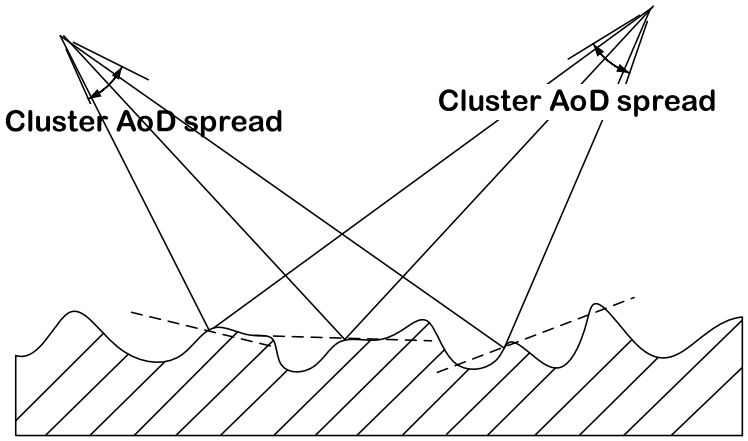

Figure 5–5: Reflection scattering mechanism

The intra cluster parameters of the channel model were estimated from the measurement data [48]. The individual rays were identified in the time domain, and statistical characteristics including average number of rays, ray arrival rate, and ray power decay time were measured.

Based on the obtained results, the statistical model for the cluster time domain parameters is given. The structure of the model is schematically shown in Figure 5–6.

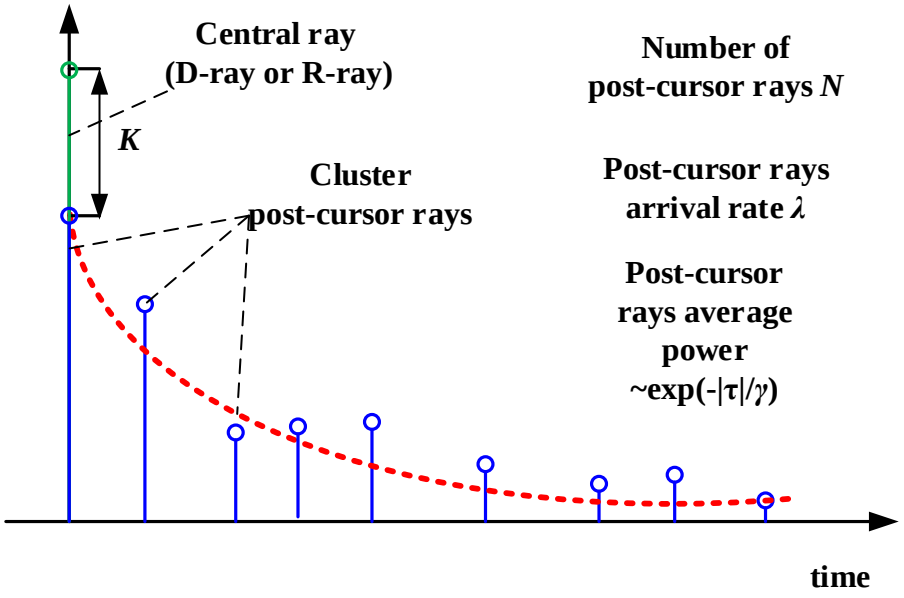

Figure 5–6: Time domain model of the intra-cluster structure

5.3.3.1 Cluster Power-delay profile

The cluster consists of a central ray $\alpha^{(i,0)}$ with fixed amplitude and post-cursor rays $\alpha^{(i,1)} \ldots \alpha^{(i,N)}$. The number of cluster post-cursor rays varies for different scenarios and specified in corresponding sections. Post-cursor rays appearance is modelled as Poisson process with arrival rate λ. The average amplitude A of the post-cursor rays decay exponentially with power decay time γ:

$$A(\tau) = A(0)e^{-|\tau|/\gamma} \tag{5–8}$$

The individual post-cursor rays $\alpha^{(i,k)}$ have random uniformly distributed phases and Rayleigh distributed amplitudes with average A.

The amplitudes of the pre-cursor rays are coupled with the amplitude of the central ray of the cluster $\alpha^{(i,0)}$ by K-factor that is defined as:

$$K = 20\log_{10}\left|\frac{\alpha^{(i,0)}}{A(0)}\right| \tag{5–9}$$

The cluster amplitudes are independent Rayleigh random variables and the corresponding phase angles are independent uniform random variables over $[0,2\pi]$

5.3.3.2 Cluster Angular characteristics

The identification of rays inside of the cluster in the angular domain requires an increase of the angular resolution by using directional antennas with very high gain.

Another approach, the application of the "virtual antenna array" technique where low directional antenna element is used to perform measurements in multiple positions along the virtual antenna array to form an effective antenna aperture were used in MEDIAN project [54]. These results were processed in [55], deriving the recommendation to model the intra-cluster angle spread for azimuth and elevation angles for both transmitter and receiver as independent normally distributed random variables with zero mean and RMS equal to 5^0: N(0, 5^0).

Note that it is reasonable to assume that different types of clusters may have distinctive intra cluster structure. For example, properties of the clusters reflected from the road surface be different from the properties of the clusters reflected from brock walls because of the different materials surface structure. Also one may assume the properties of the first and second order reflected clusters to be different, with the second order reflected clusters having larger spreads in temporal and angular domains. All these effects are understood to be reasonable. However since the number of available experimental results was limited, a common intra cluster model for all types of clusters was developed. Modifications with different intra cluster models for different types of clusters may be a subject of the future channel model enhancements.

5.3.4 Polarization Characteristics Support

5.3.4.1 General polarization description

Polarization is a property of EM waves describing the orientation of electric field **E** and magnetic intensity **H** orientation in space and time. The vector **H** due to properties of EM waves can always be unambiguously found if **E** orientation and the direction of propagation are known. So the polarization properties are usually described for **E** vector only. In the present channel modelling methodology we will follow approach to the polarization effects simulation which was successfully applied in the 802.11ad channel modelling methodology [4].

The emitted radio signal polarization is determined by the polarization properties of the antenna. In the far field zone of the EM field radiated by the antenna, the electric vector **E** is a function of the radiation direction (defined by the azimuth angle φ and elevation angle θ in the reference coordinate system). An illustration of the transmitted **E** vector in the far field zone is shown in Figure 5–7.

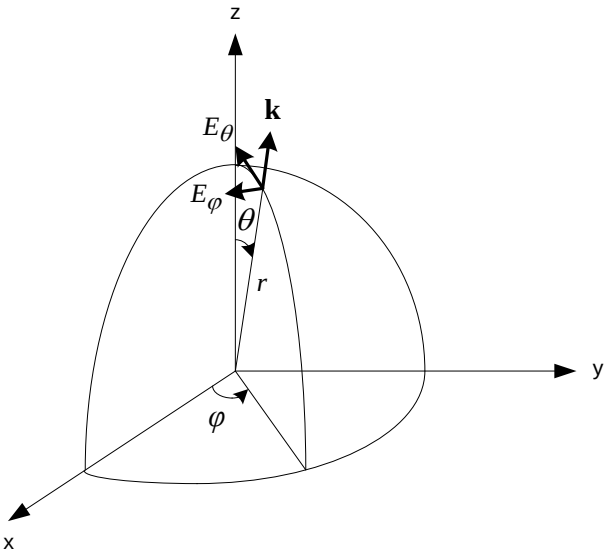

Figure 5–7: Transmitted E vector in the far field zone

Vector **E** is perpendicular to the propagation direction **k** and can be decomposed into two orthogonal components: E_θ and E_φ that belong to the planes of constant φ and constant θ angles respectively. Knowledge of E_θ and E_φ of the radiated signal (which may be functions of φ and θ) fully describes polarization characteristics of the antenna in the far field zone. The polarization direction may be described by normalised vector **e,** so called Jones vector.

5.3.4.2 Polarization Properties Description Using Jones Vector

Wave polarization can be described using *Jones calculus* introduced in optics for description of the polarized light. In the general case, a Jones vector is composed from two components of the electric field of the EM wave. The Jones vector **e** is defined as the normalized two-dimensional electrical field vector **E**. The first element of the Jones vector may be reduced to a real number. The second element of this vector is complex and, in the general case, defines phase difference between orthogonal components of the **E** field.

With the selected **E** field bases (E_θ and E_φ components) for the TX and RX antennas, the polarization characteristics of each ray of the propagation channel may be described by channel polarization matrix **H**.

In this case, the transmission equation for a single ray channel may be written as:

$$y = \mathbf{e}_{RX}^{H} \mathbf{H} \mathbf{e}_{TX} x \qquad (5\text{–}10)$$

where x and y are the transmitted and received signals, $\mathbf{e}_{TX}$ and $\mathbf{e}_{RX}$ are the polarization (Jones) vectors for the TX and RX antennas respectively. Components of polarization matrix **H** define gain coefficients between the E_θ and E_φ components at the TX and RX antennas.

For the LOS signal path, matrix $\mathbf{H}_{LOS}$ is close to the identity matrix (non-diagonal components may be non-zero but significantly smaller than diagonal elements) multiplied by the corresponding gain coefficient due to path loss. LOS propagation does not change polarization characteristics of the signals. However, polarization

characteristics of the signals are changed upon reflections. The change of the polarization characteristics upon reflection is defined by the type of the surface and the incident angle. Thus, polarization characteristics may be different for different clusters but are similar for the rays comprising one cluster. For this reason, the polarization impact was modelled at the cluster level with all rays inside one cluster having the same polarization properties. Modelling polarization impact at the level of individual rays would unnecessary complicate the model and would not provide any essential increase of the model accuracy

5.3.4.3 Polarization channel matrix for first and higher order reflections

It is known that reflection coefficients are different for **E** field components parallel and perpendicular to the plane of incidence and depend on the incident angle. Theoretical coupling between parallel and perpendicular components of the reflected signal is zero for plane media interfaces (boundaries). But due to non-idealities (roughness) of the surfaces some coupling always exists in the real channels.

An example of a first order reflected signal path is shown in Figure 5–8.

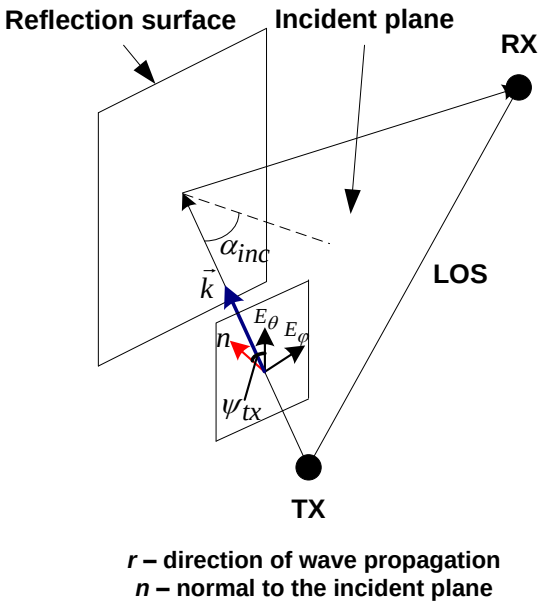

Figure 5–8: First order reflected signal path

The polarization matrix for the first order reflected signal path may be found as a product of the matrix that rotates **E** vector components from the coordinate system associated with the TX antenna to the coordinate system associated with the incident plane. Next, reflection matrix **R** with reflection coefficients and cross-polarization coupling coefficients is applied, followed by a rotation to the coordinate system associated with the RX antenna. Thus, the channel propagation matrix for the case of the first order reflected signals may be defined as:

$$\mathbf{H}_{ref\,1} = \underbrace{\begin{bmatrix} \cos(\psi_{rx}) & \sin(\psi_{rx}) \\ -\sin(\psi_{rx}) & \cos(\psi_{rx}) \end{bmatrix}}_{\substack{\text{recalculation of polarization vector from the plane of incidence basis to RX coordinates}}} \times \underbrace{\begin{bmatrix} R_{\perp}(\alpha_{inc}) & \xi_1 \\ \xi_2 & R_{\parallel}(\alpha_{inc}) \end{bmatrix}}_{\substack{\text{reflection matrix } \mathbf{R}}} \times \underbrace{\begin{bmatrix} \cos(\psi_{tx}) & \sin(\psi_{tx}) \\ -\sin(\psi_{tx}) & \cos(\psi_{tx}) \end{bmatrix}}_{\substack{\text{recalculation of TX polarization vector to the plane of incidence basis}}} \quad (5\text{–}11)$$

The reflection matrix **R** includes the reflection coefficients $R_{\perp}$ and $R_{\parallel}$ for the perpendicular and parallel components of the electric field $E_{\perp}$ and $E_{\parallel}$ respectively. Elements ξ_1 and ξ_2 in the matrix **R** are cross-polarization coupling coefficients.

Note that the structure of matrix **H** given in (5–12) does not include the propagation loss along the corresponding reflected path, which should be taken into account in the final model, but does not impact polarization properties.

Similar to (5–12), the structure of polarization matrix **H** for a second order reflection is given in (5–13) and includes additional rotation and reflection matrices.

$$\begin{aligned} \mathbf{H}_{ref\,2} = &\begin{bmatrix} \cos(\psi_{rx}) & \sin(\psi_{rx}) \\ -\sin(\psi_{rx}) & \cos(\psi_{rx}) \end{bmatrix} \times \underbrace{\begin{bmatrix} R_{\perp}(\alpha_{2inc}) & \xi_1 \\ \xi_2 & R_{\parallel}(\alpha_{2inc}) \end{bmatrix}}_{\text{2nd reflection}} \times \\ &\times \begin{bmatrix} \cos(\psi_{p}) & \sin(\psi_{p}) \\ -\sin(\psi_{p}) & \cos(\psi_{p}) \end{bmatrix} \times \underbrace{\begin{bmatrix} R_{\perp}(\alpha_{1inc}) & \xi_1 \\ \xi_2 & R_{\parallel}(\alpha_{1inc}) \end{bmatrix}}_{\text{1st reflection}} \times \begin{bmatrix} \cos(\psi_{tx}) & \sin(\psi_{tx}) \\ -\sin(\psi_{tx}) & \cos(\psi_{tx}) \end{bmatrix} \end{aligned} \quad (5\text{–}12)$$

Note that in general case the first incident plane dose not coincide with the second incident plane. Therefore the additional recalculation from coordinate system associated with the first incident plane to the coordinate system associated with the second incident plane is required.

To obtain statistical models for different types of reflected clusters, the following methodology was proposed. First, (statistical) models for the elements of the reflection matrix **R** are defined. This may be accomplished by using available experimental data (e.g. [56]) or theoretical Fresnel formulas. Then ray-tracing of interesting environments (conference room, cubicle environment, and living room) is performed with taking into account geometry and polarization characteristics of the propagation channel. After that multiple realizations of the channel polarization matrices **H** for different types of clusters are found and their statistical models are derived by approximation of the calculated empirical distributions.

Note that there are generally two mechanisms for depolarization (coupling between orthogonal components of the **E** vector at the TX and RX sides). These are reflection coupling (coupling between parallel and perpendicular **E** vector components at the reflection) and geometrical coupling (coupling because of the different relative orientations of the TX and RX antennas). It may be seen that the proposed approach allows accounting for both mechanisms to create an accurate polarization impact model.

5.3.4.4 Polarization for D-rays

Following the proposed channel modelling methodology, all properties of quasi-deterministic rays are explicitly calculated. The channel matrix H contains all polarization characteristics of the ray and calculated on the base of the reflection from the defined in the scenario surfaces.

For the cluster rays with the main D ray, the polarization matrix is the same as the D ray.

5.3.4.5 Polarization for R-rays

Random rays defined by the power-delay profile and angular characteristics and generated by producing those parameters with the pre-defined distributions. Random rays models far-away reflections and reflection from various random objects in the area. The most of random rays may be considered as second (or higher) order reflections, with corresponding polarization statistics. The channel polarization matrix distribution for second-order rays is investigated in [4] and the distribution approximations are proposed. Figure 5–9 shows the distributions of the polarization matrix **H** components for the second order reflections and corresponding approximations.

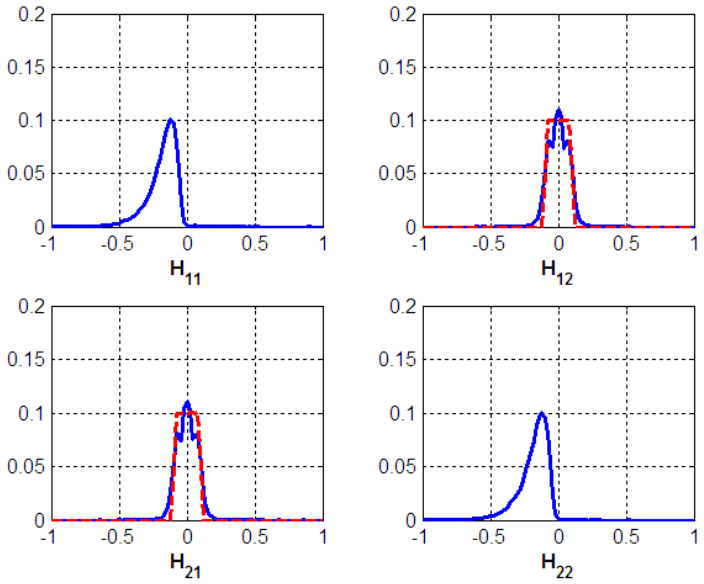

Figure 5–9: Distributions of the polarization matrix H components for the second order reflections. Solid curves show distributions obtained by ray-tracing, dashed curves show proposed approximations. For the components H_{11}, H_{22}, the proposed approximations provide very close matching to the simulated distributions and dashed curves are not plotted.

The distributions for $|H_{11}|$ and $|H_{22}|$ are truncated log-normal distributions (i.e. truncated normal distributions in dB scale) with the mean value equal to -16 dB, the standard deviation equal to 5 dB, and truncation level -2 dB. H_{11} and H_{22} have the same sign and are both negative.

Statistical distributions of the cross-coupling components H_{12} and H_{21} are approximated by random variables, uniformly distributed in the [-0.1, 0.1] interval.

For the cluster rays with the main random ray, the polarization matrix is the same as the random ray.

5.3.5 Blockage modelling

In all environment scenarios, considered in MiWEBA project, the signal propagation paths are subject to the blockage – by humans or vehicles interrupting the rays with static positions of the AP and UE, or by UE movement in the areas where some rays are shadowed. The necessity of introduction of the blockage into the 3D channel model is proven by experimental measurements (see Section 4.1.2.3)

Another similar effect that should be considered is appearance of the new rays for a short time – for example reflections from passing vehicles and other moving reflecting objects.

Both effects can be observed in the experimental measurement results with omni-directional antennas (Section 4.1)

To illustrate that, we have considered several static measurements in the street environment, with TX-RX distance about 25m. The total measurement duration was 50s, with 625000 snapshots each 0.8ms (4.1.2).

The measured channel impulse responses were processed by simple peak detection algorithm:

The point at PDP graph $P(t_k)$ is identified as peak if:

$$P(t_{k-1}) < P(t_k) > P(t_{k+1}) \text{ and}$$

$$P(t_k) > \text{estimated noise level} + 10\ dB$$

The work of peak detection algorithm is illustrated in Figure 5–10:

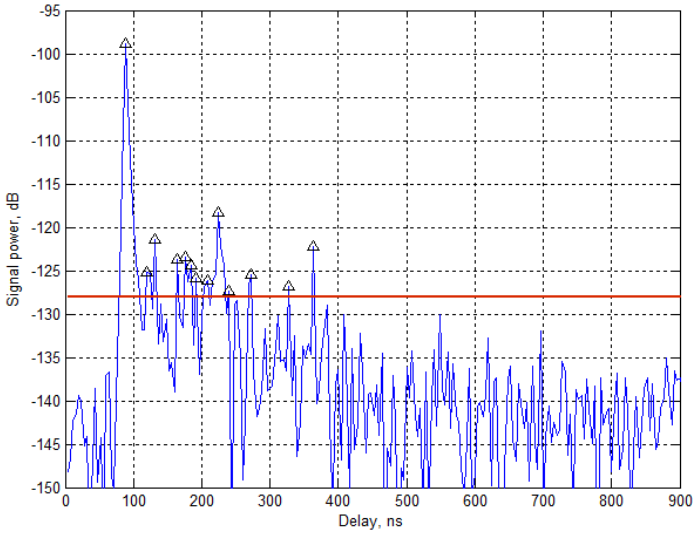

Figure 5–10: Peak detection algorithm results

After processing the whole set of channel snapshots, we can plot the ray delay vs. time diagram showing the blockage of existing rays and appearance of the new rays in a graphical representation. Figure 5–11 shows the rays diagram for measurement position close to the building walls (see Figure 4–1). The nearest wall reflected rays

can be identified close to LOS component. Figure 5–12 shows the rays diagram for measurement position in the middle of boulevard, far from walls, with roads on the both sides.

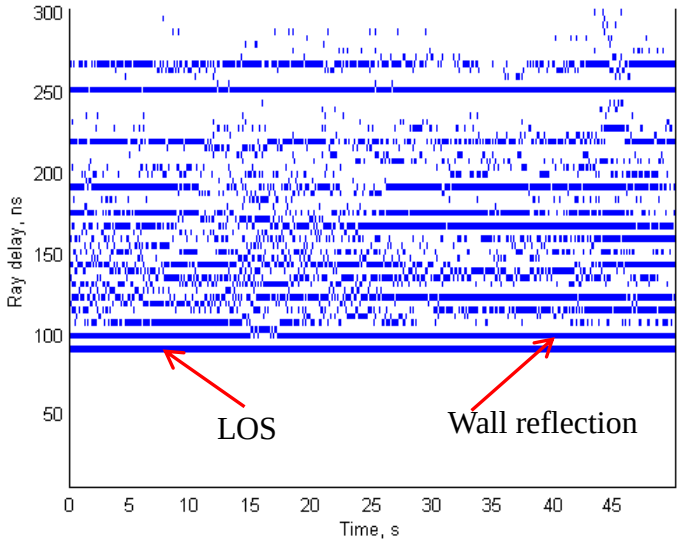

Figure 5–11: Rays diagram for measurement position close to the walls

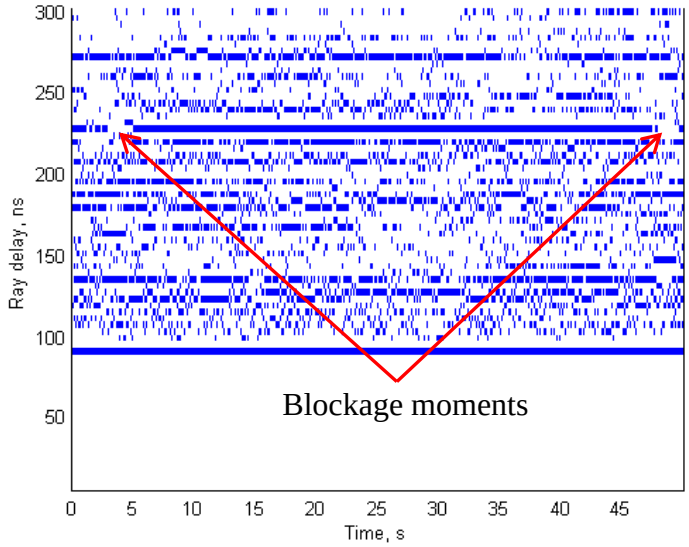

Figure 5–12: Rays diagram for middle-street measurement position

It can be seen that some steady rays in Figure 5–12 are interrupted. The same can be seen in the signal power graph – Figure 5–13

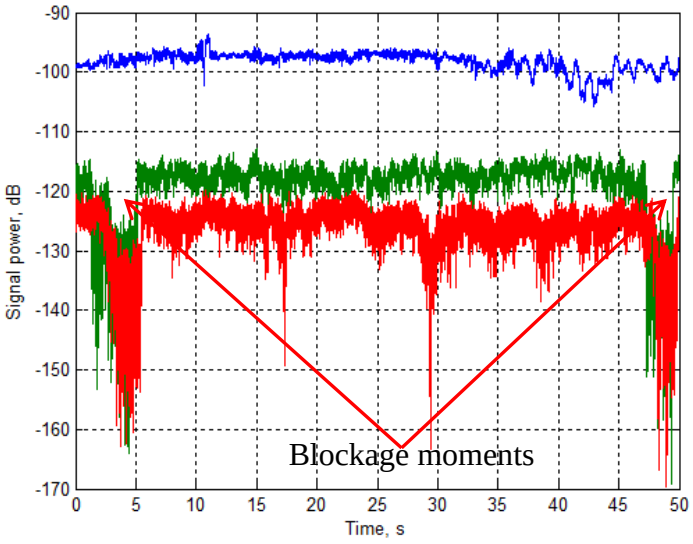

Figure 5–13: Ray blockage moments in the experimental measurements

The percentage of the "ray activity" may be estimated from the ray diagrams. Assuming ergodic properties of the blockage random process, the percentage of activity in time may be used as estimation of the blockage probability in statistical ensemble. Figure 5–14 shows the bar chart of ray activity for the Street canyon measurements scenario (near-wall position).

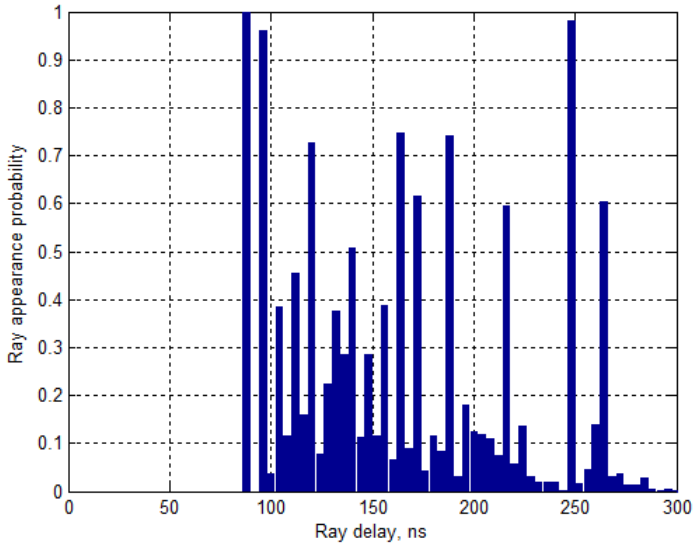

Figure 5–14: Ray appearance probability for Street canyon measurements (near-wall position)

The Figure 5–14 allows classifying the rays and identifying its place within the Q-D channel modeling approach:

- The rays with activity percentage above 80-90% are the **D-rays**: strong and always present, until blocked. The blockage percentage for D-rays may be estimated around 2-4%
- The rays with activity percentage about 40-70% are the **R-rays**: the reflections from far-away static objects, weaker and more susceptible to blockage due to longer travel distance.

- The rays with activity percentage below 30% are the **R-rays** of another type: the flashing reflection from random moving objects. Such rays are not "blocked", they actually "appearing".

Figure 5–15 illustrates the mechanism of the ray blockage and ray appearance. Following the picture, the average duration of blockage and duration of flashing reflections:

$T_{blockage}$ ~ 0.5 m (human diameter) / 1 m/s (average speed) ~ 0.5-1s
T_{flash} ~ 4.5 m (car length) / 15 m/s (average speed) ~ 0.2-0.3s

The analysis of the experimental data in ray diagrams Figure 5–11 and Figure 5–12 gives approximately the same values.

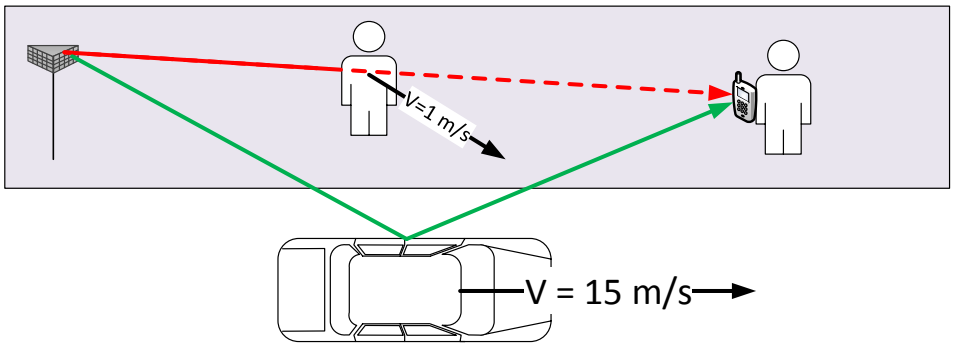

Figure 5–15: Ray blockage and random ray appearance illustration

The average service period (SP) of the mmWave communication systems is equal to 1-3ms (802.11ad).This means that for the blockage or flashing period thousands service periods and tens of thousands frames will pass. The system level simulations rarely include more than thousand frames, so the blockage may be modeled as static event, instead of dynamic process. The derived from the analysis parameters are summarized in Table 5-1. The blockage determined once per channel snapshot and stays the same in time evolution.

For VoIP and video streaming simulations, which require analysis of the longer periods of time, the blockage moments may be introduced as Poisson process with corresponding parameters, shown in Table 5-2.

Table 5-1: Blockage parameters for system level simulation

Parameter	Value
D-ray blockage probability, P_D	0.03
R-ray blockage probability, P_R	0.3
*Flashing R-ray appearance probability, P_F	0.2

Table 5-2: Blockage parameters for VoIP and video streaming simulations

Parameter	Value
D-ray blockage rate , λ_D	0.05 s^{-1}

R-ray blockage rate , λ_R	0.3 s^{-1}
D-ray and R-ray blockage duration, T	1 s
*Flashing R-ray appearance rate, λ_F	0.2 s^{-1}
*Flashing R-ray appearance duration, T_F	0.25 s

*It should be noted that for the considered outdoor scenarios (open area and street canyon) we have developed channel models on the base of static reflcetions only (D-rays and R-rays). The models with flashing R-rays require additional investigations and may be used for special studies, with the more specific vehicle/human traffic models.

5.3.6 Mobility effects

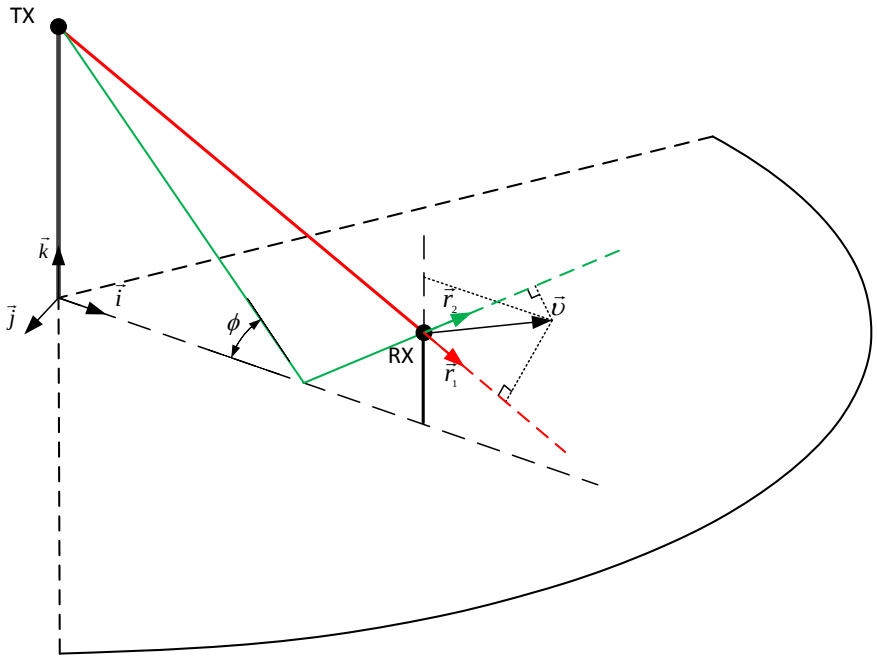

Figure 5–16: Model for mobility effects in 3D channel model

The mobility effects in our 3D channel model will be described by introducing the velocity vector for each UE). Then, for each ray (both Q-D and random) the phase rotation may be simply calculated in accordance with the next expressions:

the phase rotation for *i*-th ray caused by Doppler shifts is defined as

$$\Delta\varphi_i(t) = 2\pi f_i^D t\,, \tag{5–13}$$

where f_i^D is the Doppler shift of *i*-th ray. Its values can be calculated as

$$f_i^D = (\vec{\upsilon}, \vec{r}_i) F_c / c\,, \tag{5–14}$$

where $\vec{\upsilon}$ is the vector of RX motion and $\vec{r}_i$ is the direction of *i*-th ray arrival. The vector $\vec{\upsilon}$ can be decomposed as

$$\vec{\upsilon} = \upsilon_x \vec{i} + \upsilon_y \vec{j} + \upsilon_z \vec{k} \quad (5\text{–}15)$$

It is assumed that the horizontal components of $\vec{\upsilon}$ are normally distributed random values with appropriate mean and standard deviation values

$$P(\upsilon_x) = \frac{1}{\sigma_x \sqrt{2\pi}} e^{-\frac{(m_x - \upsilon_x)^2}{2\sigma_x^2}}, P(\upsilon_y) = \frac{1}{\sigma_y \sqrt{2\pi}} e^{-\frac{(m_y - \upsilon_y)^2}{2\sigma_y^2}} \quad (5\text{–}16)$$

Vertical component of $\vec{\upsilon}$ is defined as

$$\upsilon_z = \frac{dz}{dt}, \quad (5\text{–}17)$$

where $z(t)$ is a stationary Gaussian random process with correlation function equal to

$$K_z(\tau) = \sigma_z^2 e^{\frac{-\tau^2}{\tau_z^2}} \quad (5\text{–}18)$$

For this vertical motion correlation function the one-side power spectral density function of υ_z can be calculated as

$$G_{\upsilon_z}(f) = 8\pi^{5/2} \sigma_z^2 \tau_z f^2 e^{-(\pi \tau_z f)^2} \quad (5\text{–}19)$$

Figure 5–17: demonstrates the power spectral density of vertical speed for $\sigma_z = 0.05m$ and $\tau_z = 0.5s$

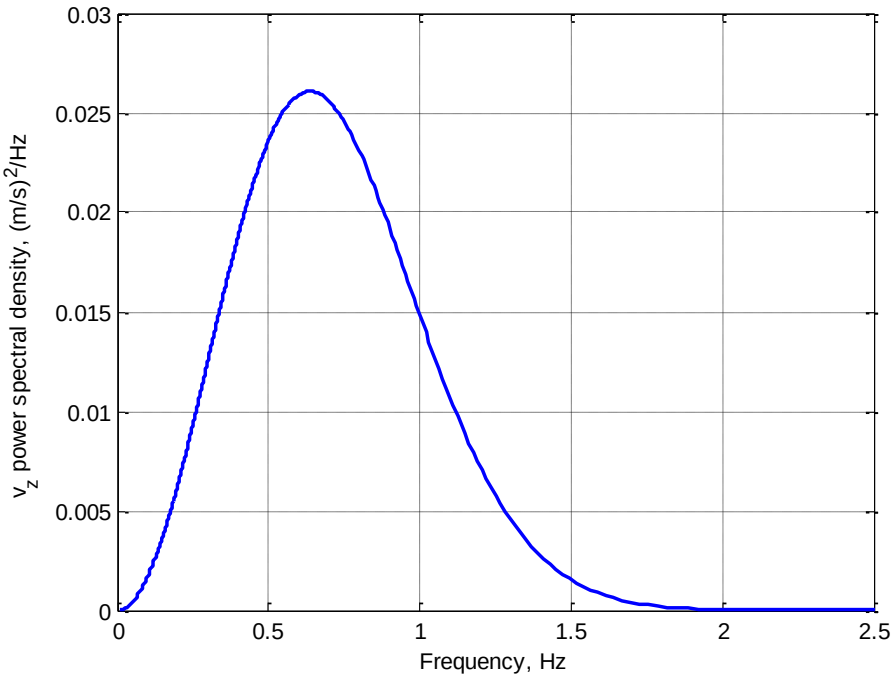

Figure 5–17: Power spectral density of vertical speed ($\sigma_z = 0.05m, \tau_z = 0.5s$)

5.3.7 3D Antenna models

5.3.7.1 Isotropic Radiator

An isotropic radiator is a simplistic antenna model which is used as a convenient theoretical model to describe channel behaviour. It has spherical radiation pattern and equal antenna gain for all spatial directions. Since it does not have any spatial selectivity, it does not require any beam forming algorithm and captures all existing channel rays between transmitter and receiver.

The isotropic radiator is supported in the current channel model for analytical purposes.

5.3.7.2 Steerable Antenna Model with Gaussian Main Lobe Profile

The real world antenna design may have quite sophisticated radiation pattern which complicates simulations of the channel. Especially this is true for the phased antenna arrays with very high number of radiation elements such as Modular Antenna Arrays (MAA). In order to simplify channel modelling and at the same time take into account the essential characteristics of the real world antennas the following antenna model is introduced. This antenna has a main lobe with Gaussian profile in linear scale (or parabolic profile in decibel scale) and constant level of side lobes.

The main lobe gain function is defined using two-dimensional Gaussian function as follows:

$$G(\varphi,\theta) = G_0 \exp\left(-\alpha\varphi^2\right)\exp\left(-\beta\theta^2\right) \tag{5–20}$$

where φ is azimuth angle in the range {-π, π}, θ is elevation angle in the range {-π/2, π/2}, G_0 is a maximum gain corresponding to direction (φ =0, θ = 0) and α and β are constants which are determined by the half power beam widths φ_{-3dB} and θ_{-3dB} accordingly. Figure 5–18 (a) illustrates the system of coordinates and angles definitions.

Half power beam width for azimuth angle φ_{-3dB} is defined for θ = 0 and θ_{-3dB} for φ = 0 as follows:

$$\begin{aligned} \frac{G(\varphi,\theta)}{G_0} &= \exp\left(-\alpha\left(\varphi_{-3dB}/2\right)^2\right) = \frac{1}{2} \\ \frac{G(\varphi,\theta)}{G_0} &= \exp\left(-\beta\left(\theta_{-3dB}/2\right)^2\right) = \frac{1}{2} \end{aligned} \tag{5–21}$$

Hence, α and β constants may be expressed as follows:

$$\alpha = \frac{4\ln(2)}{\varphi_{-3dB}^2} \quad \beta = \frac{4\ln(2)}{\theta_{-3dB}^2} \tag{5–22}$$

Figure 5–18b shows half power beam width definition for elevation angle. A similar picture may be plotted for azimuth angle in X-Y axes.

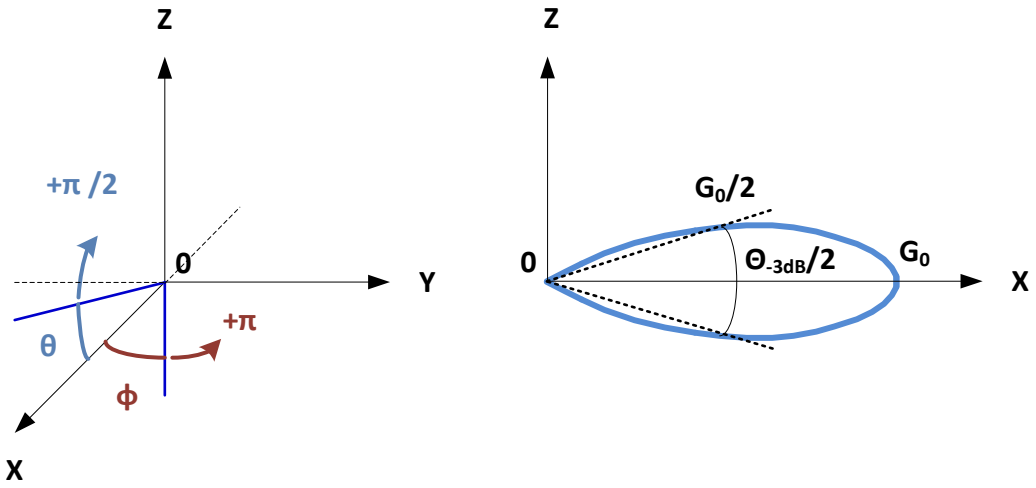

(a) Coordinates **(b) Half power beam width definition**

Figure 5–18: Illustration of coordinates and half power beam width definition.

Substituting from the equations above one can obtain:

$$G(\varphi,\theta) = G_0 \exp\left(-4\ln(2)\frac{\varphi^2}{\varphi_{-3dB}^2}\right)\exp\left(-4\ln(2)\frac{\theta^2}{\theta_{-3dB}^2}\right) \qquad (5\text{–}23)$$

In decibel scale it may be rewritten as follows:

$$G_{dB}(\varphi,\theta) = G_{0,dB} - 12\cdot\left(\frac{\varphi}{\varphi_{-3dB}}\right)^2 - 12\cdot\left(\frac{\theta}{\theta_{-3dB}}\right)^2 \qquad (5\text{–}24)$$
$$10\lg(e)\cdot 4\ln(2) \approx 12$$

The main lobe beam widths φ_{ML} and θ_{ML} are defined for the gain -20 dB relatively to the maximum gain value G_0. Using (5–24) one can obtain the relation between φ_{ML} and φ_{-3dB} for $\theta = 0$ and θ_{ML} and θ_{-3dB} for $\varphi = 0$ as follows:

$$\begin{aligned} \theta_{ML} &\approx 2.6\cdot\theta_{-3dB}, \quad \varphi = 0 \\ \varphi_{ML} &\approx 2.6\cdot\varphi_{-3dB}, \quad \theta = 0 \end{aligned} \qquad (5\text{–}25)$$

The maximum gain G_0 may be calculated using its relation with the aperture size as follows: $G_0 = \dfrac{4\pi\cdot S}{\lambda^2}$ (5–26)

where S is an aperture size measured in square meters and λ is a wavelength.

Note that the beam width of the main lobe may be simply related with the rectangular antenna aperture physical dimensions using the following equations:

$$\varphi_{ML} = \frac{2\lambda}{D_y} \quad \theta_{ML} = \frac{2\lambda}{D_x} \qquad (5\text{–}27)$$

where D_x and D_y are dimensions of antenna aperture along x and y axes accordingly. Assuming that

$$S = D_x \cdot D_y \tag{5–28}$$

and deriving D_x and D_y one can obtain:

$$S = \frac{4\lambda^2}{\varphi_{ML} \cdot \theta_{ML}} \tag{5–29}$$

Substituting (5–29) into (5–26) the equation for the maximum gain G_0 may be rewritten as follows:

$$G_0 = \frac{16\pi}{\varphi_{ML} \cdot \theta_{ML}} \tag{5–30}$$

Using relation in eq. (5-22) the maximum gain may be represented as a function of half power beam widths as follows:

$$G_0 = \frac{16\pi}{6.76 \cdot \varphi_{-3dB} \cdot \theta_{-3dB}} \tag{5–31}$$

The final formula for the main lobe gain function is written as follows:

$$G_{dB}(\varphi,\theta) = 10\lg\left(\frac{16\pi}{6.76 \cdot \varphi_{-3dB} \cdot \theta_{-3dB}}\right) - 12 \cdot \left(\frac{\varphi}{\varphi_{-3dB}}\right)^2 - 12 \cdot \left(\frac{\theta}{\theta_{-3dB}}\right)^2 \tag{5–32}$$

The gain for the angles outside of the main lobe is defined so that integration over total solid angle 4π gives unity (normalization condition). In that case the total radiated power of directive antenna pattern is equal to the total radiated power in isotropic case.

Therefore, the pair of parameters (φ_{-3dB},θ_{-3dB}) fully define the radiation pattern of the considered antenna model.

Figure 5–19 shows an example of the antenna pattern plotted with parameters ($\varphi_{-3dB}=15^0$,$\theta_{-3dB}=15^0$). Note that this radiation pattern has an axial symmetry (see X-Y plane in Figure 5–19).

The maximum gain G_0 in that case in is equal to:

$$G_{0,dB} \approx 20.4\text{dBi} \tag{5–33}$$

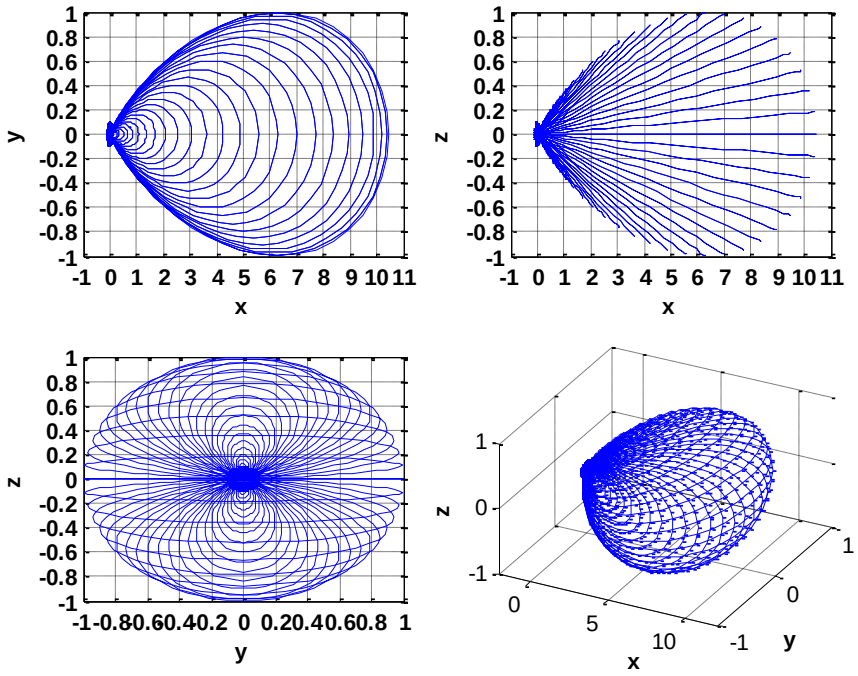

Figure 5–19: Example of antenna pattern with parameters ($\varphi_{-3dB}=15^0$,$\theta_{-3dB}=15^0$).

Figure 5–20 shows antenna pattern without axial symmetry with parameters ($\varphi_{-3dB}=15^0$,$\theta_{-3dB}=60^0$). The maximum gain G_0 in that case is equal to:

$$G_{0,dB} \approx 14.3\text{dBi} \tag{5–34}$$

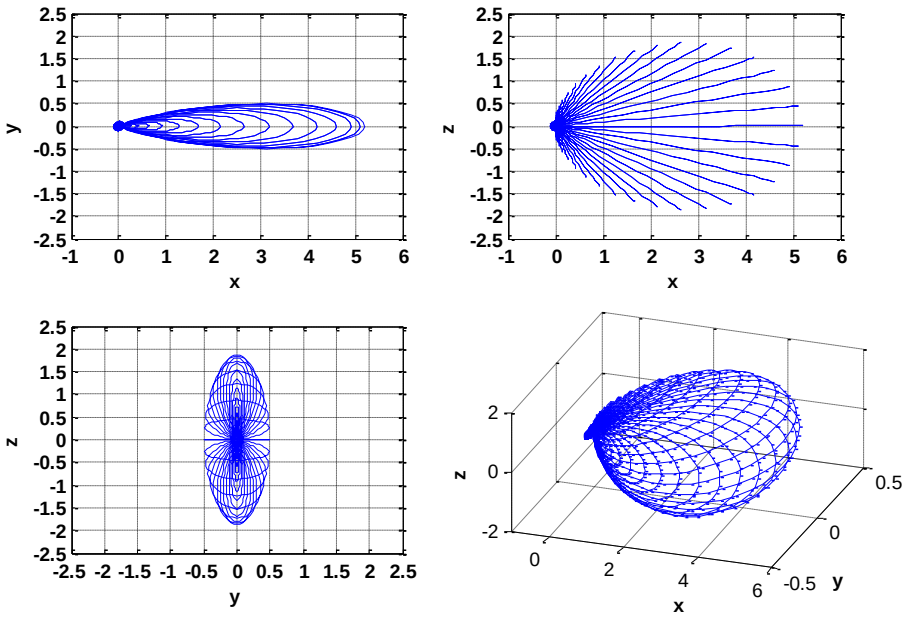

Figure 5–20: Example of antenna pattern with parameters ($\theta_{-3dB}=15^0$,$\varphi_{-3dB}=60^0$).

5.3.7.3 Phased Antenna Array Model

Phased antenna array is used as a primary solution in antenna design in WPAN / WLAN 60 GHz communication systems, such as IEEE 802.15.3c or IEEE 802.11ad. Exploiting of phased antenna array allows efficient implementation of beamforming algorithms and protocols requiring several micro seconds to find LOS path or best reflection in NLOS environment and set up directional link. Therefore this type of antenna model is highly important and should be supported in the current channel model.

In this document planar phased antenna arrays are considered only. The antenna array may be composed of an arbitrary number of elements, but the rectangular geometry is assumed. Figure 5–21 shows an example of the target phased antenna array geometry.

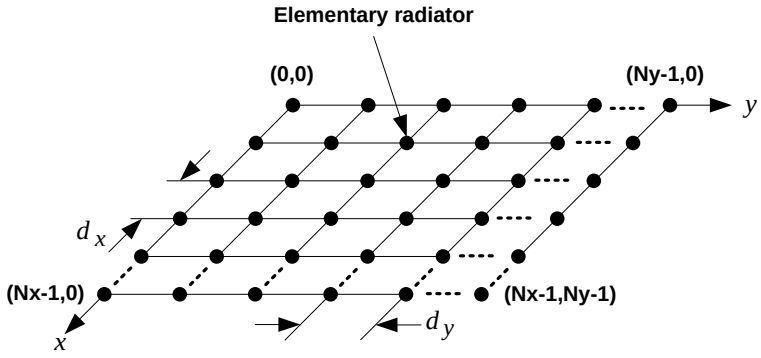

Figure 5–21: Illustration of planar rectangular phased antenna array geometry.

The elementary radiators are placed along X and Y directions (normal to each other) with equidistant paces d_x and d_y accordingly. Note, that the d_x may be chosen not equal to d_y in general case. The number of radiators along X and Y axes N_x and N_y may be selected not equal to each other as well. It is assumed that all elementary radiators have the same radiation pattern and the considered array is homogeneous in that sense.

The gain function for the phased antenna array may be written as follows:

$$G(\varphi,\theta)=\left|\sum_{n_x=0}^{N_x-1}\sum_{n_y=0}^{N_y-1} f(\varphi,\theta)\cdot W_{nx,ny}\cdot\exp\left(j\Delta\varphi_{nx,ny}\right)\right|^2 \qquad (5\text{–}35)$$

where $f(\varphi,\theta)$ is a radiation pattern of a single elementary radiator, $W_{nx,ny}$ are complex weights defining elementary radiators excitation, and $\Delta\varphi_{nx,ny}$ is a phase shift due to geometry placement with coordinates (n_x,n_y) relative to the phase of the radiator with coordinates (0,0).

Due to the fact that all elementary radiators have the same radiation pattern, the gain function may be simplified and represented as a product of the gain of elementary radiator and array factor as follows:

$$G(\varphi,\theta) = |f(\varphi,\theta)|^2 \cdot \left| \underbrace{\sum_{n_x=0}^{N_x-1}\sum_{n_y=0}^{N_y-1} W_{nx,ny} \cdot \exp\left(j\Delta\varphi_{nx,ny}\right)}_{Array\ factor} \right|^2 \quad (5\text{–}36)$$

The elementary radiator may have isotropic or any other radiation pattern. Figure 5–22 below shows antenna pattern of elementary radiator used for planar arrays in our evaluation.

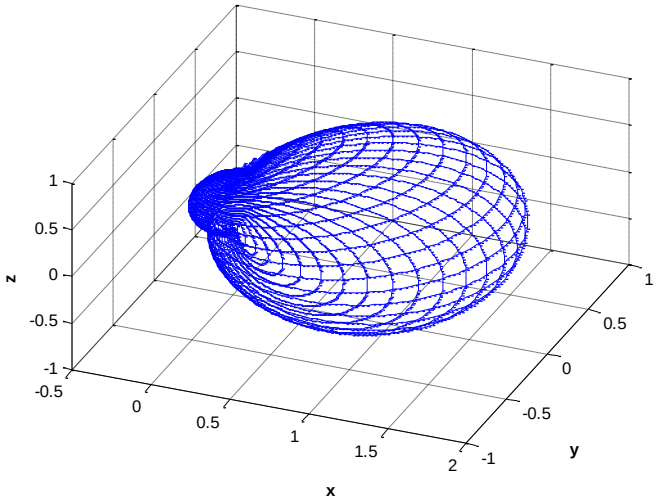

Figure 5–22: Antenna pattern of elementary radiator.

The practical example implemented in the channel model is a phased antenna array with (N_x=2, N_y =8) geometry. Its 3D antenna pattern and projections into the azimuthal and elevation (φ = 0 and θ = 0) planes are shown in Figure 5–23.

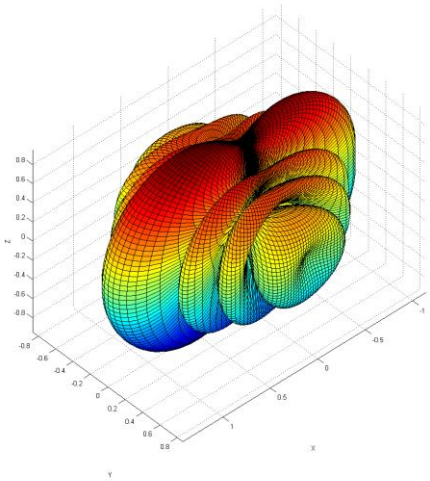

(a) 3D planar phased antenna array radiation pattern with (N_x=2, N_y=8) geometry

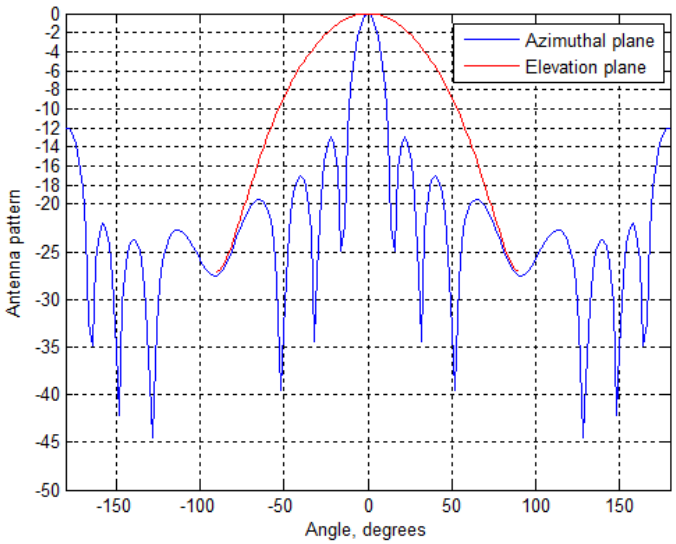

(b) Projections of antenna pattern into azimuthal and elevation planes

Figure 5–23: Planar phased antenna array radiation pattern with (N_x=2, N_y=8) geometry.

5.3.7.4 Modular Antenna Array Model

The main idea behind partially adaptive Modular Antenna Array (MAA) is constructing a large-aperture array from a several low-cost sub-array modules. Each sub-array module consists of small phased antenna array with built-in RF-IC, so each module has capability of independent beamsteering with help of phase shifters control. All antenna modules are connected to the central beamforming unit typically implemented in the base band. RF phase control in sub-array modules provides relatively coarse beamforming, which is then refined in the baseband [57]. Figure 5–24 shows a schematic diagram for Modular Antenna Array architecture.

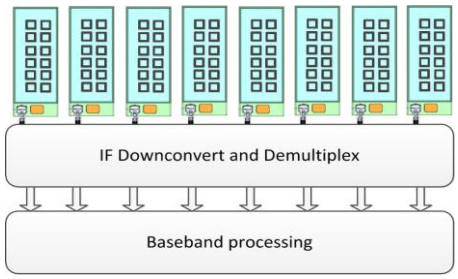

Figure 5–24: Modular Antenna Array architecture

Sub-array module design may substantially decrease the feeding lines power losses (due to their short lengths in each sub-array) and reduce the cost of large aperture antenna because of unified cheap modules usage. 8x2=16 elements (vertical x horizontal) phased antenna array described in Section 5.9.3 can be used as sub-array module.

For the evaluation purposes MAA can be replaced with Full Adaptive Arrays (FAA). In the FAA concept, signal from each antenna element can be processed (weighted) independently via its own RF chain. Therefore, the number of the degrees of freedom in the FAA is equal to the number of antenna elements and the two-dimensional FAA has no limitations in beam forming in both vertical and horizontal planes.

From the link budget point of view, the FAA and MAA antennas with equal number of antenna elements will provide the same TX power output and antenna gain in the broad side direction. Hence, their performance in single-user mode should be nearly the same, since the MAA can create single beam almost as effective as more flexible precise weighting (beam forming) in the FAA. However, in the case of simultaneously served group of users in MU-MIMO mode the situation changes. Partially adaptive structure of MAA due to specific constraints in degrees of freedom will not be able to form beams with maximal gains towards arbitrary located group of users.

5.3.8 3D Channel model generation

The generation of the 3D channel model in accordance with present methodology consists of the following steps:

- Scenario and model parameters definition
- Calculation of the deterministic components data in accordance with selected scenario recommendations
- Calculation of random components data in accordance with selected scenario recommendations
- Apply path blockage in accordance with scenario requirements to the selected clusters
- Apply antenna TX and RX antenna patterns and beamforming algorithms
- Conversion of the raw channel impulse response data into the discrete time required by the simulations

The channel modelling generation flow is illustrated in Figure 5–25

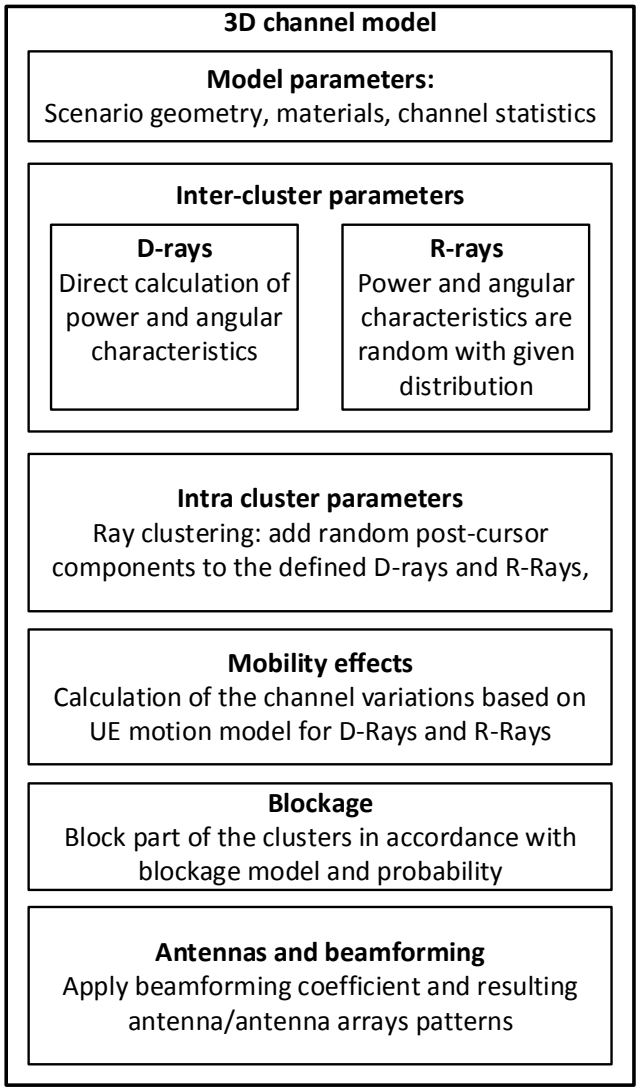

Figure 5–25: 3D channel model generation

5.3.9 Common channel model parameters

The parameters required for calculation of the channel model are summarized in the Table 5-3. This notation will be used further for the specific scenarios description.

Table 5-3: General parameters of the 3D channel model

Parameter	Description
F_c	Carrier frequency, Hz
c	Lightspeed, c=299792458 m/s
A_0	Oxygen absorption, dB/km, (0.015 dB/m for 60 GHz)

Htx	Transmitter height above ground, m (see Figure 5–26)
Hrx	Receiver height above ground, m
L	Horizontal distance between TX and RX, m
$A_{tx}(\varphi,\theta,\varphi_0,\theta_0)$	TX antenna pattern (as function or interpolation table)
$Arx(\varphi,\theta,\varphi_0,\theta_0)$	RX antenna pattern (as function or interpolation table)
ε_r	Relative permittivity of the ground surface at F_c,
σ	Surface roughness: heights standard deviation

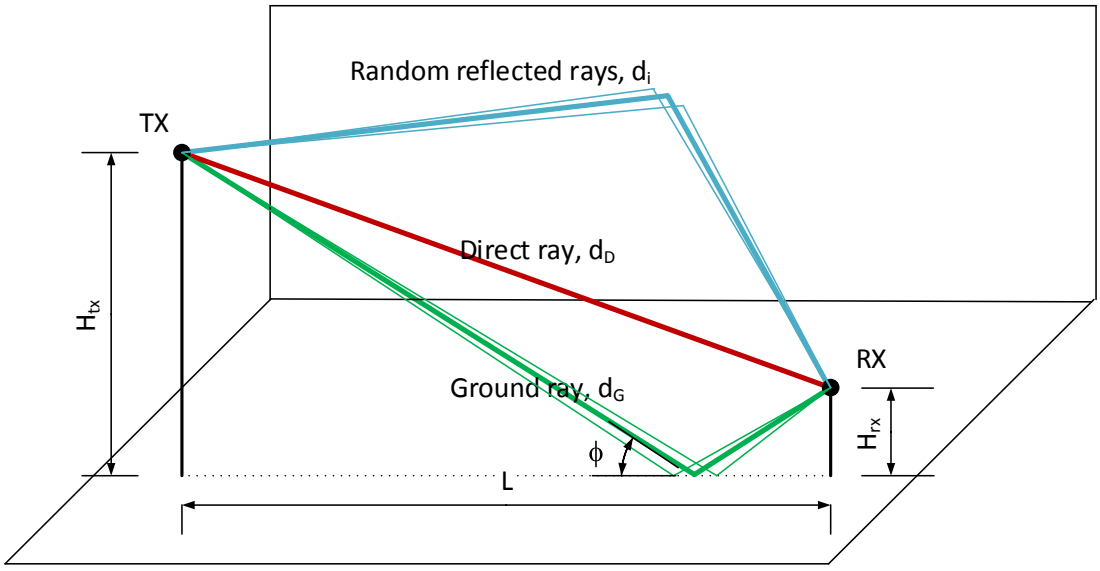

Figure 5–26: Channel model geometry

5.4 University campus access channel model

The university campus channel model represents the scenario with large open areas with low and rare buildings like university campus, park areas, city squares.

5.4.1 Modeling Scenarios: geometry and UE deployment

The geometry for Open area scenario is based on 3GPP Heterogeneous network scenario [58]. That scenario represents the deployment with hexagonal layout for LTE Macro nodes and a number of uniformly dropped within each macro geographical area hot zones served by LTE low power nodes. The scenario is extended by adding mmWave BSs into the hot zones. Considering the use of directional antennas (see Section 5.3.7) several differently oriented mmWave BSs should be placed into the hot zone.

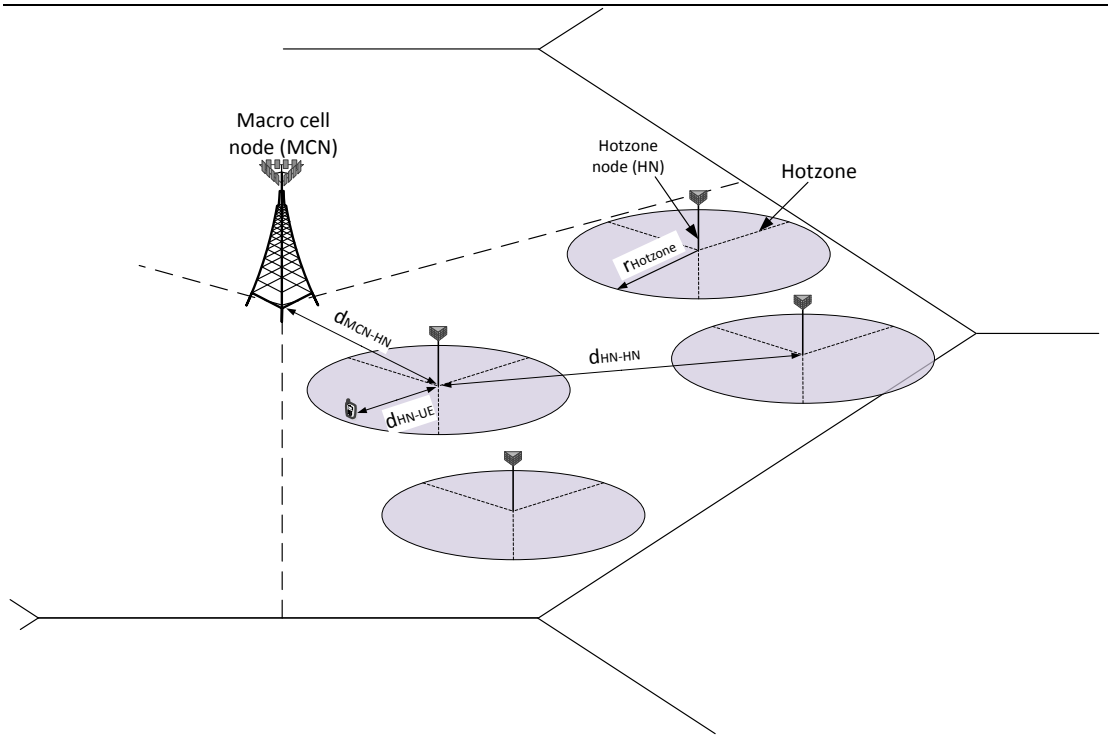

Figure 5–27: 3GPP HetNet scenario with small cells

Table 5-4: Open-area model parameters

Parameter	Value
Inter-site distance	500m
Number of Macro cells per site	3
Number of hotzones per macro cell, N_{HN}	4
$d_{MCN\text{-}HN\_min}$	75m
$d_{HN\text{-}HN\_min}$	40 m
Hotzone node height, H_{HN}	6 m
UE dropping	Clustered*
Number of users per macro cell, N_{users}	>100
Fraction of hotspot users, $P^{hotspot}$	9/10
$r_{Hotzone}$	40m
$d_{HN\text{-}UE\_min}$	5m
$d_{MCN\text{-}UE\_min}$	35m
UE height, H_{UE}	1.5m
Number of mmWave BS per hotzone	3
Surface material	asphalt

Surface ε_r	4 + 0.2j
Surface roughness (standard deviation)	3 mm

*Clustered UE dropping:

- Fix the total number of users, N_{users}, dropped within each macro geographical area.
- Randomly and uniformly drop the configured number of hotzone nodes, N_{HN}, within each macro geographical area (the same number N_{HN} for every macro geographical area).
- Randomly and uniformly drop N_{users_HN} users within $r_{Hotzone}$ radius of each hotzone node, where $N_{users\_HN} = \lfloor P^{hotspot} \cdot N_{users} / N_{HN} \rfloor$
- Randomly and uniformly drop the remaining users, $N_{users} - N_{users\_HN} \cdot N_{HN}$ to the entire macro geographical area of the given macro cell (including the hotzone area).

5.4.2 Model Development Methodology

In the university campus (outdoor access larger area) scenario deployment the UEs have only two dominant rays: the direct ray and the ground reflected ray (Figure 5–28). These rays are counted as deterministic and explicitly calculated during the channel modeling. In addition to deterministic components the direct and reflected rays, there are random components that represent reflection scattering. The reflection from the distant walls and second-order reflection are taken into account as random components.

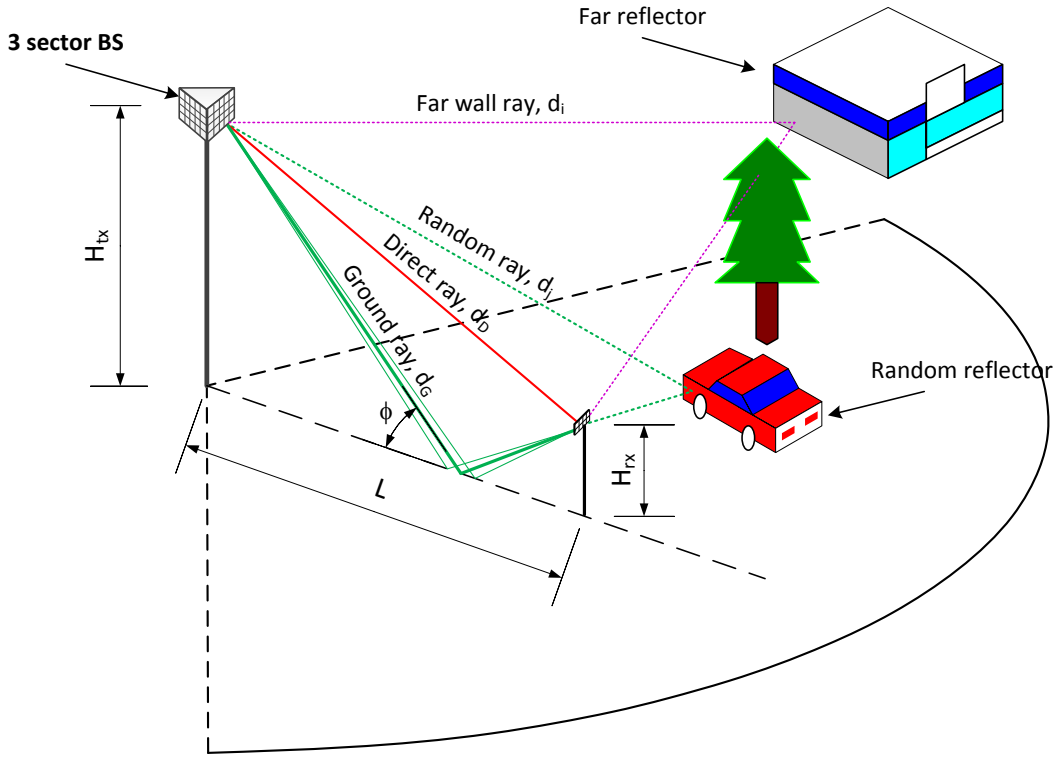

Figure 5–28: University campus (outdoor access larger area) mmWave small cell environment

5.4.3 3D channel model description

5.4.3.1 Direct ray

Direct ray consists of deterministic component D0 and additional intra-cluster component, D1 which describes random obstacles of the direct ray with blockage several Fresnel zones. The intra-cluster components are described in the corresponding section.

Table 5-5: University campus (outdoor access larger area) direct ray parameters

Component	Parameter	Value
D0	Delay	Direct ray delay is calculated from the model geometry: $\tau_{D0} = d_D / c$ $d_D = \sqrt{L^2 + (H_{tx} - H_{rx})^2}$
	Power	Direct ray power calculated as free-space pathloss with oxygen absorption $P_{D0} = 20\log 10\left(\lambda / 4\pi d_0\right) - A_0 d_0$, in dB
	AoD	0° azimuth and elevation

	AoA	0° azimuth and elevation

5.4.3.2 Ground-reflected ray

Ground-reflected ray consists of deterministic component G0 and random cluster component G1 which describes signal scattering from the rough surface

Table 5-6: University campus (outdoor access larger area) model ground-reflected ray parameters

Component	**Parameter**	**Value**
G0	Delay	Ground-reflected ray delay is calculated from the model geometry: $\tau_{G0} = d_G / c$ $d_G = \sqrt{L^2 + (H_{tx} + H_{rx})^2}$
	Power	Ground-reflected power calculated as free-space pathloss with oxygen absorption, with additional reflection loss calculated on the base of Fresnel equations $P_{G0} = 20\log 10\left(\lambda / 4\pi d_G\right) - A_0 d_G + R + F$ $R = 20\log 10\left(\frac{\sin\phi - \sqrt{B}}{\sin\phi + \sqrt{B}}\right)$ $B = \varepsilon_r - \cos^2\phi$ for horizontal polarization $B = \left(\varepsilon_r - \cos^2\phi\right)/\varepsilon_r^2$ for vertical polarization and ϕ is a grazing angle, see Figure 5–26 $\tan(\phi) = (H_{tx} + H_{rx})/L$ $F = -\frac{80}{\log 10}\left(\frac{\pi \sin\phi \sigma_g}{\lambda}\right)^2$, in dB
	AoD	Azimuth: 0° Elevation: $\theta_{AoD} = \arctan\left[L/(H_{tx} - H_{rx})\right] - \arctan\left[L/(H_{tx} + H_{rx})\right]$
	AoA	Azimuth: 0° Elevation: $\theta_{AoA} = \arctan\left[(H_{tx} + H_{rx})/L\right] + \arctan\left[(H_{tx} + H_{rx})/L\right]$

5.4.3.3 Random rays*

Table 5-7: University campus (outdoor access larger area) model inter-cluster parameters

Parameter	Value
Number of clusters, $N_{cluster}$	3
Cluster arrival rate, λ	$0.05ns^{-1}$
Cluster power-decay constant, γ	15ns
K-factor	6dB
AOA	Elevation: U[AOA_{G0}:AOA_{D0}] Azimuth: U[-60:60°]
AOD	Elevation: U[AOD_{G0}:AOD_{D0}] Azimuth: U[-60:60°]

*Some values can be corrected due to further measurements

5.4.3.3 Intra-cluster parameters

Table 5-8: University campus (outdoor access larger area) model intra-cluster parameters

Parameter	Value
Post-cursor rays *K*-factor, *K*	6 dB for LOS ray, 4 dB for NLOS*
Post-cursor rays power decay time, γ	4.5 ns
Post-cursor arrival rate, λ	$0.31\ ns^{-1}$
Post-cursor rays amplitude distribution	Rayleigh
Number of post-cursor rays, *N*	4

*The cluster post-cursor ray K-factor is derived from the experimental measurement described in Section 4.1.2.2 – static measurements on the broad street. The dominant rays were identified and time domain signal variations served as a base for K-factor evaluation.

5.5 Street canyon access channel model

The street canyon (outdoor access ultra-high-rate hot-spots) channel model represents typical urban scenario: city Street with pedestrians' sidewalks along the tall long buildings. The access link between the APs on the lampposts and the UEs at human hands is modeled in this scenario.

5.5.1 Modeling Scenarios: geometry and UE deployment

The geometry of the Street canyon access scenario that is used for channel model parameters evaluation via ray-tracing simulations is shown in Figure 5–29. The corresponding numerical parameters are summarized in Table 5-9.

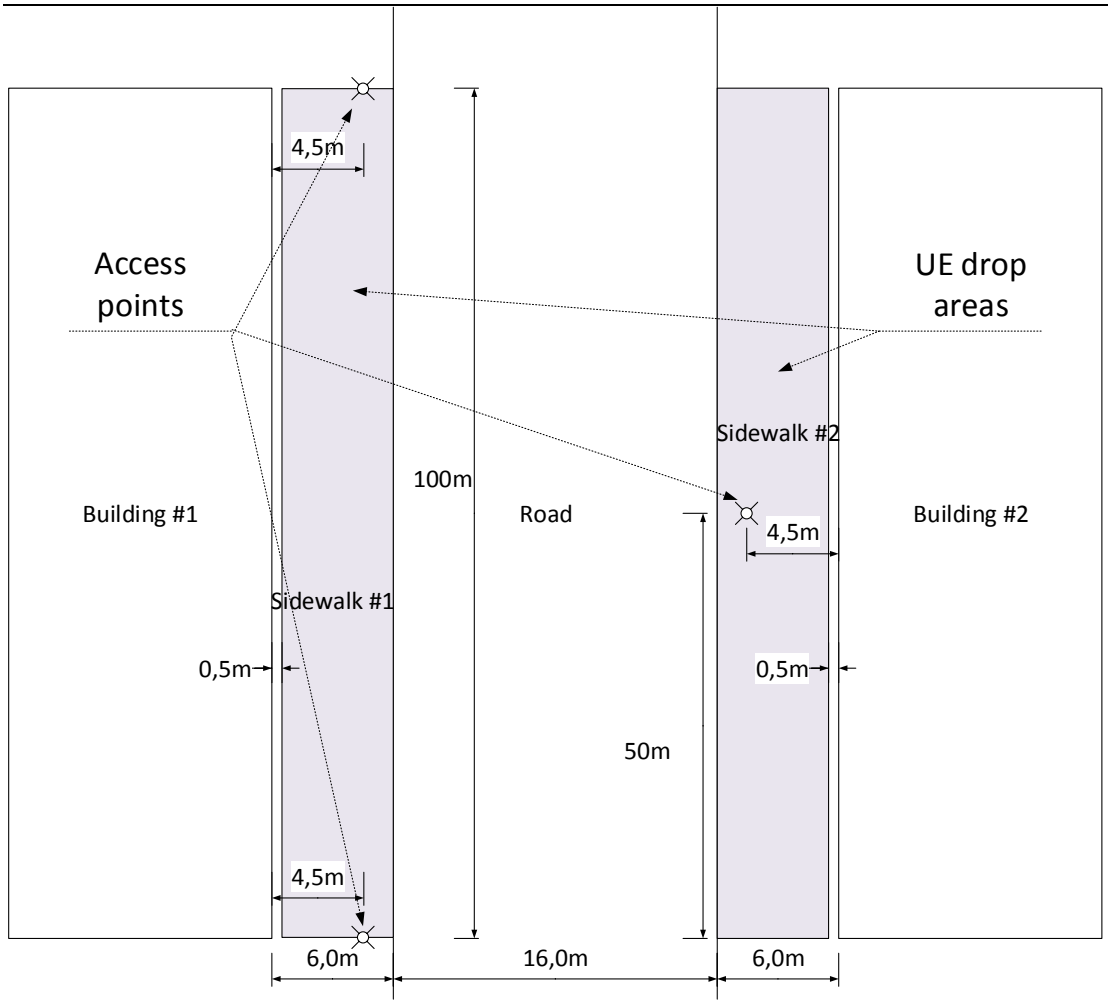

Figure 5–29: Street canyon (outdoor access ultra-high-rate hot-spots) scenario

Table 5-9: Street canyon (outdoor access ultra-high-rate hot-spots) scenario parameters

Parameter	**Value**
AP height, H_{tx}	6 m
UE height, H_{rx}	1.5m
AP distance from nearest wall, D_{tx}	4.5 m
Sidewalk width	6 m
Road width	16 m
Street length	100 m
AP-AP distance, same side	100 m
AP-AP distance, different sides	50 m
Road and sidewalk material	asphalt
Road and sidewalk ε_r	4+0.2j
Road and sidewalk roughness σ_g	0.2 mm

(standard deviation)	
Building walls material	concrete
Building walls ε_r	6.25+0.3j
Building walls roughness σ_w (standard deviation)	0.5 mm

5.5.2 Model Development Methodology

In the street canyon (outdoor access ultra-high-rate hot-spots) scenario deployment the UEs grouped on a relatively narrow path, and with two dominant reflected rays in addition to the direct: the ground reflected ray and the wall-reflected ray. All those rays are counted as deterministic and explicitly calculated during the channel modeling. In addition to deterministic components the direct and reflected rays, there are random components that represent reflection scattering. The reflection from the distant walls and second-order reflection are taken into account as random components.

To evaluate the distributions of the power, delays and angular characteristics of clusters counted as stochastic in our model, the street canyon scenario was implemented within the ray-tracing platform in accordance with the description in previous section.

Figure 5–30 shows the example of UE in the area and the result of the ray tracing from the AP position to one UE location.

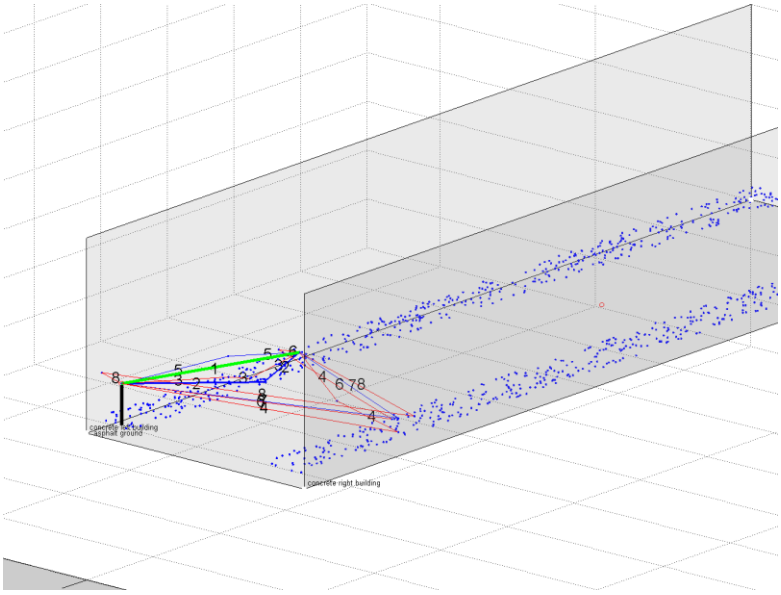

Figure 5–30: Street canyon (outdoor access ultra-high-rate hot-spots) scenario in the ray-tracing platform

To evaluate stochastic rays' parameters distributions, 100000 channel realizations for uniformly distributed UEs were calculated and analyzed.

The distributions of reflected rays' power (ratio of the direct ray power to the chosen reflected ray power in dB) for vertical, horizontal, and circular polarizations are shown in

Figure 5–31, Figure 5–32 and Figure 5–33:

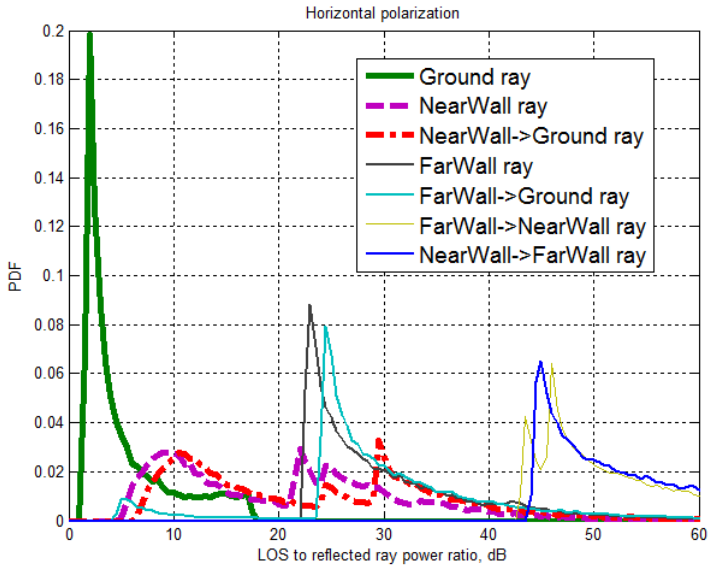

Figure 5–31: Reflected rays power distribution for street canyon (outdoor access ultra-high-rate hot-spots) scenario (Horizontal polarization)

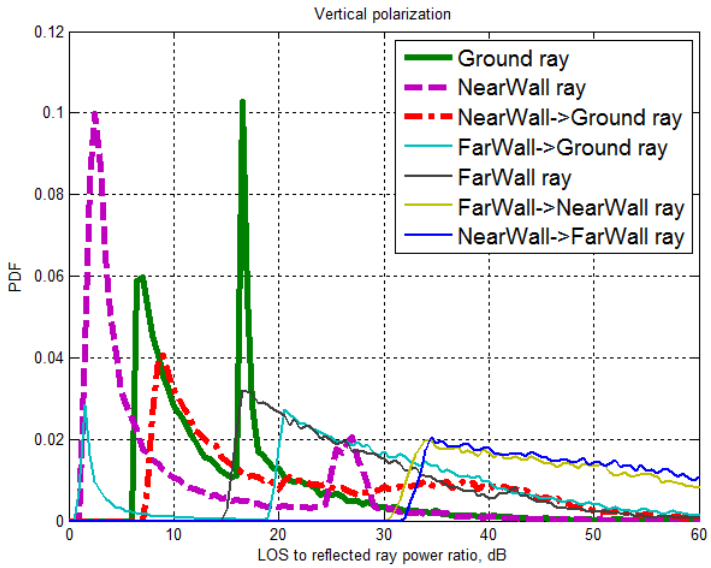

Figure 5–32: Reflected rays power distribution for street canyon (outdoor access ultra-high-rate hot-spots) scenario (Vertical polarization)

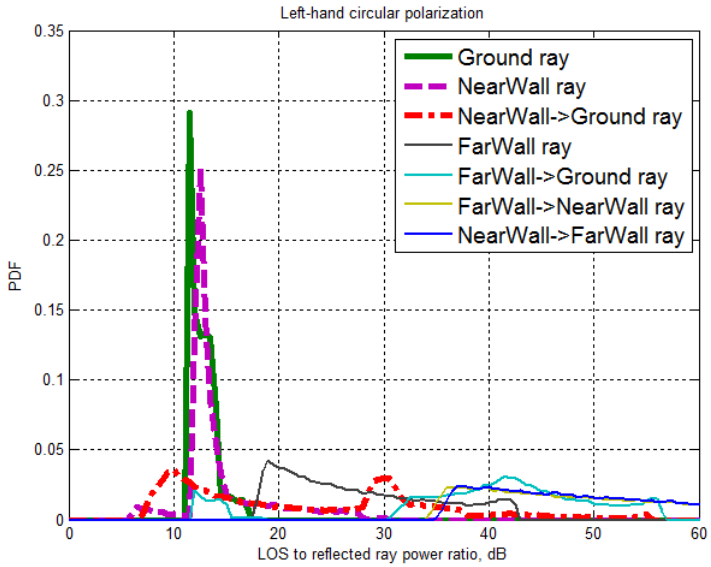

Figure 5–33: Reflected rays power distribution for street canyon (outdoor access ultra-high-rate hot-spots) scenario (Circular polarization)

It can be seen that for all three cases the three reflected rays are dominant: the ground ray, the ray reflected from the nearest wall and combined reflection from the nearest wall and ground. The other components are more than 20 dB below the LOS ray.

Figure 5–34 shows the PDF of the ratio of all but three selected rays power to the total power in the all NLOS rays. It can be seen that more than 90% of the NLOS components power is accumulated within ground ray, wall-reflected ray and combined ground-wall reflection.

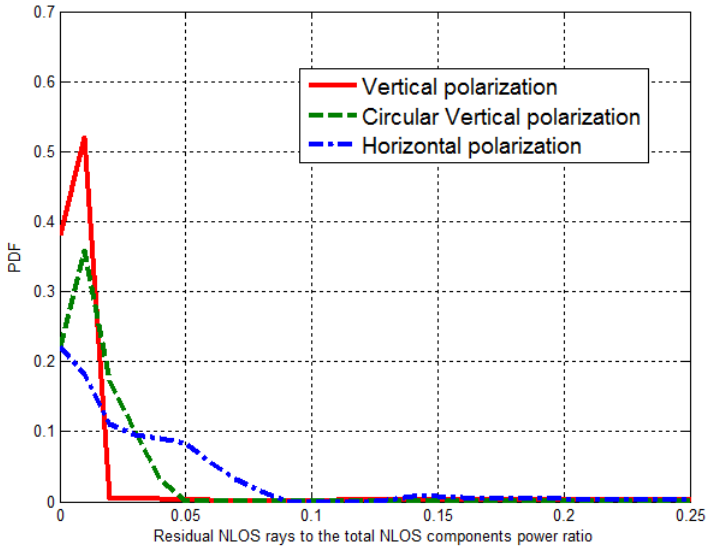

Figure 5–34: PDF of residual reflected rays' power to the total NLOS power.

So, for street canyon (outdoor access ultra-high-rate hot-spots) 3D channel model we propose to take into account three dominant rays as deterministic, and the other rays as random. The random component should not only include the reflections from

simple two-wall model, but also reflections from bus stops, cars, trucks and other street objects.

Next Figure 5–35 shows the distribution of the delays for the street canyon (outdoor access ultra-high-rate hot-spots) scenario. It can be seen that the selected deterministic rays grouped together with delays less than 20 ns, while the other have almost uniform distribution from 60 to 180 ns. Since we plan to take into account reflections from the all random street objects, the possible delays may be in range [0,200ns]. Assuming the exponential PDP and Poisson rays arrival model, the cluster arrival rate may be estimated equal to 0.03 ns^{-1}.

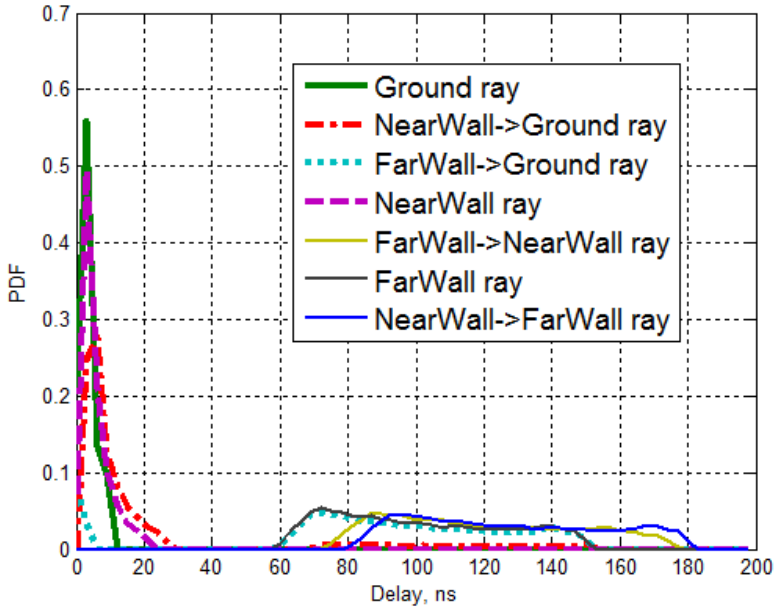

Figure 5–35: Delay PDF for Street canyon scenarios

5.5.3 3D channel model description

The main parameters relevant to the street canyon (outdoor access ultra-high-rate hot-spots) 3D channel model are shown in Figure 5–36.

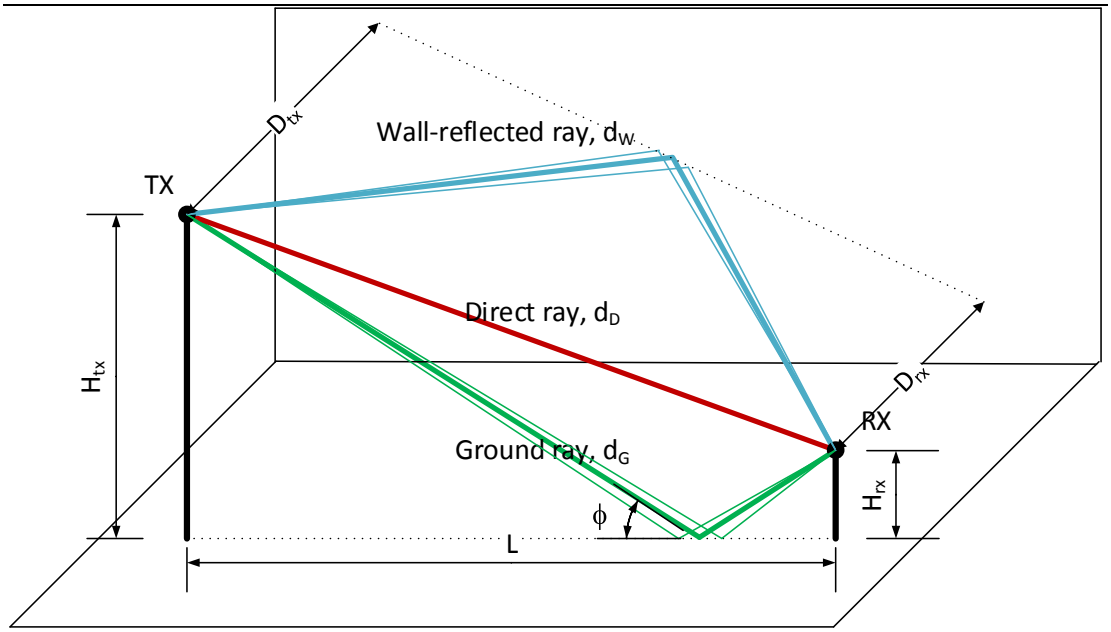

Figure 5–36: Street canyon (outdoor access ultra-high-rate hot-spots) scenario reflected rays illustration

5.5.3.1 Direct ray

Direct ray consists of deterministic component D0 and additional intra-cluster component, D1 which describes random obstacles of the direct ray with blockage several Fresnel zones. The intra-cluster components are described in the corresponding section.

Table 5-10: Street canyon (outdoor access ultra-high-rate hot-spots) model direct ray parameters

Component	Parameter	Value
D0	Delay	Direct ray delay is calculated from the model geometry: $\tau_{D0} = d_D / c$ $d_D = \sqrt{L^2 + (H_{tx} - H_{rx})^2}$
	Power	Direct ray power calculated as free-space pathloss with oxygen absorption $P_{D0} = 20\log 10\left(\lambda / 4\pi d_0\right) - A_0 d_0$, in dB
	AoD	0° azimuth and elevation
	AoA	0° azimuth and elevation

5.5.3.2 Ground-reflected ray

Ground-reflected ray consists of deterministic component G0 and random cluster component G1 which describes signal scattering from the rough surface

Component	Parameter	Value
G0	Delay	Ground-reflected ray delay is calculated from the model geometry: $\tau_{G0} = d_G / c$ $d_G = \sqrt{L^2 + (H_{tx} + H_{rx})^2}$
	Power	Ground-reflected power calculated as free-space pathloss with oxygen absorption, with additional reflection loss calculated on the base of Fresnel equations $P_{G0} = 20\log 10\left(\lambda / 4\pi d_G\right) - A_0 d_G + R + F$ $R = 20\log 10\left(\frac{\sin\phi - \sqrt{B}}{\sin\phi + \sqrt{B}}\right)$ $B = \varepsilon_r - \cos^2\phi$ for horizontal polarization $B = \left(\varepsilon_r - \cos^2\phi\right)/\varepsilon_r^2$ for vertical polarization and ϕ is a grazing angle, see Figure 5–26 $\tan(\phi) = (H_{tx} + H_{rx})/L$ $F = -\frac{80}{\log 10}\left(\frac{\pi \sin\phi \sigma_g}{\lambda}\right)^2$, in dB
	AoD	Azimuth: 0° Elevation: $\theta_{AoD} = \arctan[L/(H_{tx} - H_{rx})] - \arctan[L/(H_{tx} + H_{rx})]$
	AoA	Azimuth: 0° Elevation: $\theta_{AoA} = \arctan[(H_{tx} + H_{rx})/L] + \arctan[(H_{tx} + H_{rx})/L]$

Table 5-11: Street canyon (outdoor access ultra-high-rate hot-spots) model ground-reflected ray parameters

5.5.3.3 Wall-reflected ray

Wall-reflected ray consists of deterministic component W0 and random cluster component W1 which describes signal scattering from the rough surface.

Table 5-12: Street canyon (outdoor access ultra-high-rate hot-spots) model wall-reflected ray parameters

Component	Parameter	Value
W0	Delay	Wall-reflected ray delay is calculated from the model geometry: $\tau_{W0} = d_W / c$ $d_W = \sqrt{d_D{}^2 + (D_{tx} + D_{rx})^2}$
	Power	Ground-reflected power calculated as free-space pathloss with oxygen absorption, with additional reflection loss calculated on the base of Fresnel equations $P_{W0} = 20\log 10\left(\lambda / 4\pi d_W\right) - A_0 d_W + R + F$ $R = 20\log 10\left(\frac{\sin\phi - \sqrt{B}}{\sin\phi + \sqrt{B}}\right)$ $B = \varepsilon_r - \cos^2\phi$ for vertical polarization $B = \left(\varepsilon_r - \cos^2\phi\right)/\varepsilon_r^2$ for horizontal polarization and ϕ is a grazing angle, see Figure 5–26 $\tan(\phi) = (D_{tx} + D_{rx})/d_D$ $F = -\frac{80}{\log 10}\left(\frac{\pi \sin\phi \sigma_w}{\lambda}\right)^2$, in dB
	AoD	Azimuth: $\theta_{AoD} = \arctan[d_D/(D_{tx} - D_{rx})] - \arctan[d_D/(D_{tx} + D_{rx})]$ Elevation: 0°
	AoA	Azimuth: $\theta_{AoA} = \arctan[(D_{tx} + D_{rx})/d_D] + \arctan[(D_{tx} + D_{rx})/d_D]$ Elevation: 0°

5.5.3.4 Combined Wall-ground-reflected ray

The second-order reflection ray from the nearest wall and ground (WG) can be calculated nearly in the same way as ground and wall reflections, employing the "method of images" illustrated in Figure 5–37.

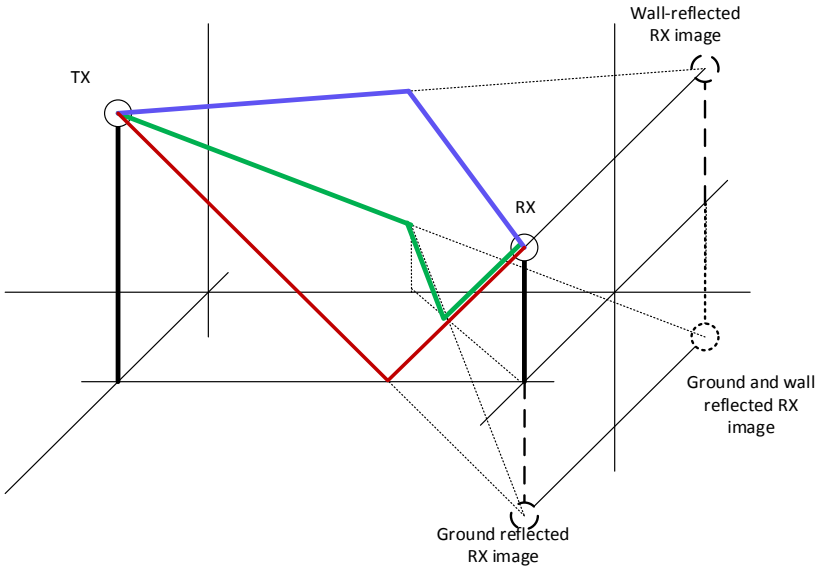

Figure 5–37: Method of images in application to combined wall-ground ray calculation

5.5.3.5 Random rays

The random components of channel impulse response statistics derived from the street canyon (outdoor access ultra-high-rate hot-spots ray-tracing modeling in previous section and from the measurement data.

Table 5-13: Street canyon (outdoor access ultra-high-rate hot-spots) model random rays parameters

Parameter	**Value**
Number of clusters, $N_{cluster}$	5
Cluster arrival rate, λ	$0.03ns^{-1}$
Cluster power-decay constant, γ	20ns
Ray K-factor	10 dB
AoA	Elevation: U[-20:20°] Azimuth: U[-180:180°]
AoD	Elevation: U[-20:20°] Azimuth: U[-180:180°]

*Some values can be corrected due to further measurements

5.5.3.6 Intra-cluster parameters

Table 5-14: Street canyon (outdoor access ultra-high-rate hot-spots) model intra-cluster parameters

Parameter	Value
Post-cursor rays *K*-factor, *K*	6 dB for LOS ray, 4 dB for NLOS*
Post-cursor rays power decay time, γ	4.5 ns
Post-cursor arrival rate, λ	0.31 ns^{-1}
Post-cursor rays amplitude distribution	Rayleigh
Number of post-cursor rays, *N*	4

*The cluster post-cursor ray K-factor is derived from the experimental measurement described in Section 4.1.2.2 – static measurements on the broad street. The dominant rays were identified and time domain signal variations served as a base for K-factor evaluation.

5.6 Hotel lobby access channel model

The hotel lobby (indoor access large public area) channel model represents typical indoor scenario: large hall with multiple users within. Similar indoor channel models were considered in the [4], with statistical approach to the channel modeling, suitable for link layer simulations. The proposed here quasi-deterministic approach based on the specified UE location and may be used also for the system level simulations.

5.6.1 Modeling Scenarios: geometry and UE deployment

The basic parameters and geometry are summarized in Table 5-15 and illustrated in Figure 5–38:

Table 5-15: Hotel lobby (indoor access large public area) scenario parameters

Parameter	Value
AP height, H_{tx}	3.5 m
AP position	Middle of the nearest wall (see Figure 5–38)
UE height, H_{rx}	1.5m
Room height	4 m
Room width	10 m
Room length	15 m
Floor material	Concrete
Floor ε_{rf}	4 + 0.2j

Floor roughness σ_f (standard deviation)	0.1 mm
Walls material	Concrete
Walls ε_{rw}	4 + 0.2j
Walls roughness σ_w (standard deviation)	0.2 mm
Ceiling material	Plasterboard
Ceiling ε_{rc}	6.25+0.3j
Ceiling roughness σ_c (standard deviation)	0.2 mm

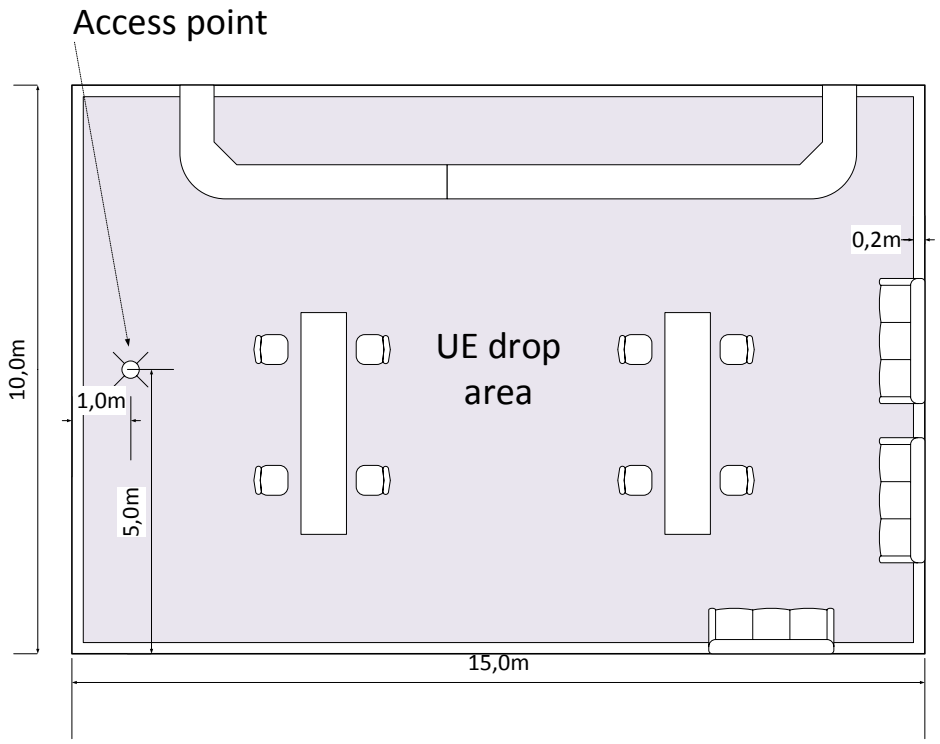

Figure 5–38: Hotel lobby (indoor access large public area) scenario

5.6.2 Model Development Methodology

To analyze the properties of the hotel lobby (indoor access large public area) scenario, the scenario environment were implemented on the base of the ray-tracing platform. The deployment and ray-tracing results are show in Figure 5–39.

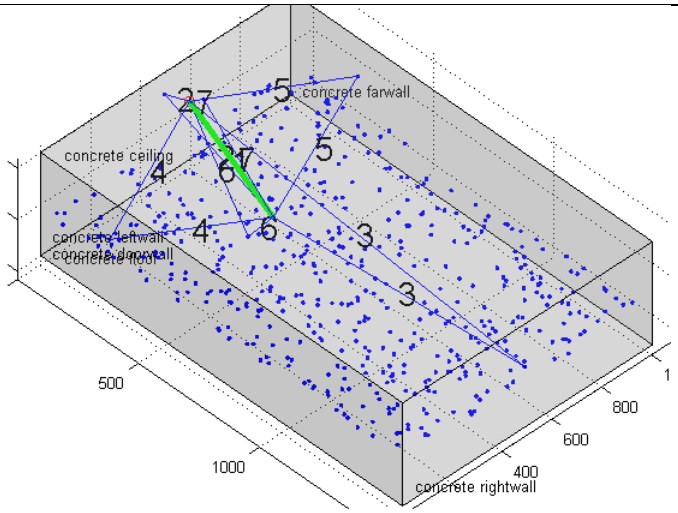

Figure 5–39: Hotel lobby (indoor access large public area) scenario in the ray-tracing platform (only 1st order reflections shown)

To evaluate ray power distribution, 10000 random UE position were generated within the area and rays up to the second reflection order were calculated and then rays power PDFs were plotted for selected ray. As it can be seen from Figure 5–40 and Figure 5–41 (vertical and circular antennas polarizations), there are no dominant rays for the Hotel lobby scenarios and even second-order rays may have significant power and cannot be neglected. Thus, for Hotel lobby scenario, we propose to take into account all rays up to second reflections order (on and two reflections) as deterministic rays.

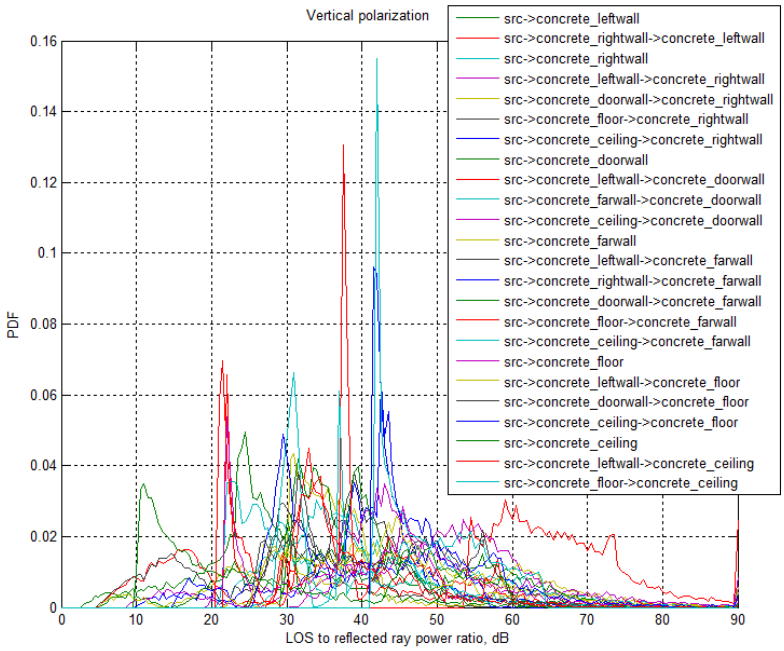

Figure 5–40. Reflected rays power distribution for hotel lobby (indoor access large public area) scenario (Vertical polarization)

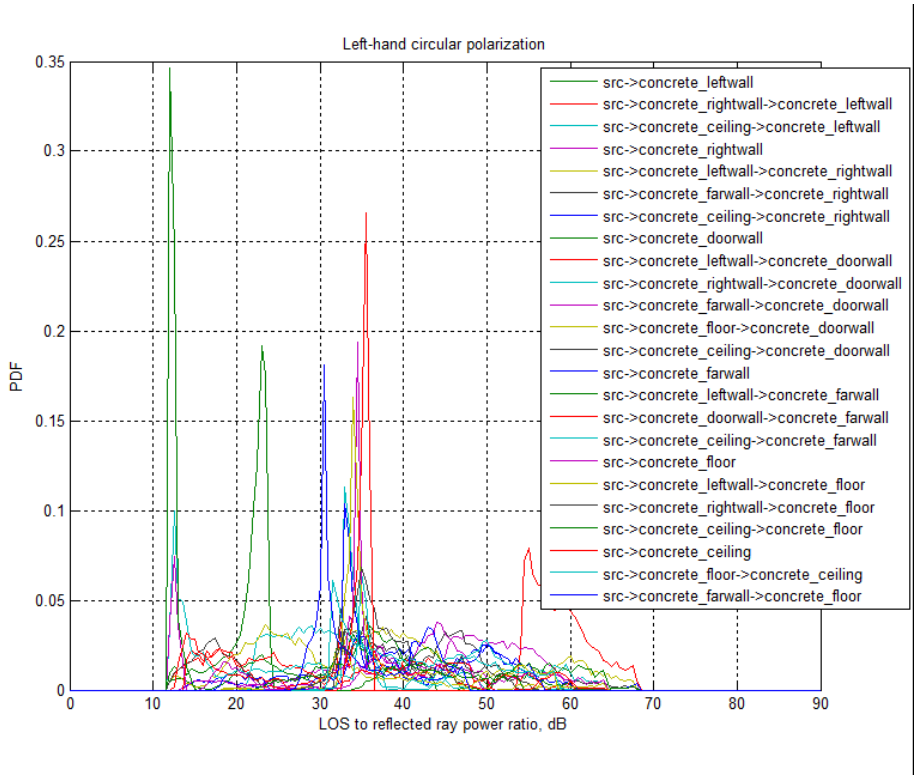

Figure 5–41. Reflected rays power distribution for hotel lobby (indoor access large public area) scenario (circular polarization)

5.6.3 3D channel model description

The 3D channel model for hotel lobby (indoor access large public area) scenario include up to second order reflection rays, calculated by some ray-tracing algorithm on the base of method of images. Rays powers are calculated using the Fresnel equation. Additional losses due to oxygen absorption and reflection from the rough surfaces are also counted.

Table 5-16: Hotel lobby (indoor access large public area) model parameters

Parameter	Value
Delay	Delay for each individual ray is calculated from the model geometry on the base of path lengths: $\tau = d/c$
Power	Power for each ray is calculated from the Fresnel equations $P = 20\log 10\left(\lambda/4\pi d\right) - A_0 d + R + F$ $R = 20\log 10\left(\frac{\sin\phi - \sqrt{B}}{\sin\phi + \sqrt{B}}\right)$ $B = \varepsilon_r - \cos^2\phi$ for horizontal polarization $B = \left(\varepsilon_r - \cos^2\phi\right)/\varepsilon_r^2$ for vertical polarization and ϕ is a grazing angle $F = -\frac{80}{\log 10}\left(\frac{\pi \sin\phi \sigma_g}{\lambda}\right)^2$, in dB
AoD	Calculated from model geometry for each UE position
AoA	Calculated from model geometry for each UE position

5.6.3.1 Intra-cluster parameters

The intra cluster parameters for indoor access scenario are taken directly from the corresponding indoor scenario, developed in [4] and are based on the experimental measurements [48].

Table 5-17: Hotel lobby (indoor access large public area) model intra-cluster parameters

Parameter	Value
Post-cursor rays *K*-factor, K	10 dB
Post-cursor rays power decay time, γ	4.5 ns
Post-cursor arrival rate, λ	0.31 ns^{-1}
Post-cursor rays amplitude distribution	Rayleigh
Number of post-cursor rays, N	6

5.7 Backhaul channel models

5.7.1 ART backhaul channel model

Above rooftop backhauling scenario (see Figure 3–4) models the backhaul link between two ART access points, typically with very high gain and high directionality antennas. This leads to the absolute dominance of the direct LOS ray, and the other rays (which may present in this environment) are much weaker.

So, the ART backhaul channel model consists only from the single LOS ray:

Table 5-18: ART backhaul channel model

Component	Parameter	Value
D0	Delay	Direct ray delay is calculated from the model geometry: $\tau_{D0} = d_D / c$, $d_D = \sqrt{L^2 + \Delta H^2}$, where L – horizontal distance between antennas, ΔH – antenna heights difference.
	Power	Direct ray power calculated as free-space pathloss with oxygen absorption $P_{D0} = 20\log 10\left(\lambda / 4\pi d_0\right) - A_0 d_0$, in dB
	AoD	0° azimuth and elevation
	AoA	0° azimuth and elevation

Intra Cluster Parameters

Although the LOS ray between to ART AP doesn't encounter reflection and scattering, the ray may have some random components due to partial blockage of the first Fresnel zone or environmental changes (temperature, air density, etc.). This is modeled by adding a cluster to the direct ray. Cluster parameters are shown in

Table 5-19: Cluster parameters for ART backhaul scenario

Parameter	Value
Post-cursor rays *K*-factor, *K*	10 dB
Post-cursor rays power decay time, γ	4.5 ns

Post-cursor arrival rate, λ	0.31 ns^{-1}
Post-cursor rays amplitude distribution	Rayleigh
Number of post-cursor rays, N	4

5.7.2 Street canyon front haul channel model

The only difference between the Street canyon front haul channel model and Street canyon access model (See Section 5.5) it is the height of the RX side (UE or another AP), with the both AP heights equal to 6 m. The other parameters and calculations are the same.

5.8 Device to device channel models

The Q-D approach to the channel modeling with explicit calculation of the major rays and statistical description of the rays with minor impact once defined for one scenario can be easily extended to the scenarios with similar geometries, but slightly different parameters. For example the model for access scenarios (with the TX height about 6 m and RX height about 1.5) can be successfully applied for backhauling scenarios (see 5.7.2) and for D2D scenarios (both TX and RX have 1.5m height)

5.8.1 Open area D2D channel model

The Open area D2D scenario is described by the same model as Open area access environment (see Section 5.4). The height of both TX and RX are set to 1.5m, the other parameters are not changed.

5.8.2 Street canyon D2D scenario

The Street canyon D2D scenario is described by the same model as Street canyon access (see Section 5.5). The height of both TX and RX are set to 1.5m, the other parameters are not changed.

5.8.3 Hotel lobby D2D scenario

The Hotel lobby D2D scenario is described by the same model as Hotel lobby access environment (see Section 5.6). The height of both TX and RX are set to 1.5m, the other parameters are not changed.

5.9 MiWEBA path loss models

Development of path-loss models for usage in system level simulation and link budget evaluations integrating rain fall effects, oxygen absorption and bandwidth impact shall be done in future work.

5.9.1 Street canyon access path loss model

The street canyon access path loss model is based on the measurement campaign described in chapter 4. The measurement snapshots were taken using omnidirectional antennas. When calculating the path loss on this basis all possible propagation paths between transmitter and receiver are taken into account. This is somewhat unrealistic as real millimeter-wave communication systems will most probably employ

directional antennas to improve their link budget. Directional antennas imply that a spatial filtering of signals propagating towards the antenna is performed, depending on its orientation and antenna pattern. In order to replicate this behavior, a filter was applied to each channel impulse response from the measurement, before it was used to calculate the instantaneous path loss.

The filter attenuates all components in the channel impulse response that are a certain number of samples away from the line-of-sight distance on the delay axis. This way only the line-of-sight component, the ground reflection and reflections from other objects very close to the line-of-sight path are taken into account. It is assumed that this filter on the delay axis is a good approximation of a spatial filtering around the line-of-sight between transmitter and receiver.

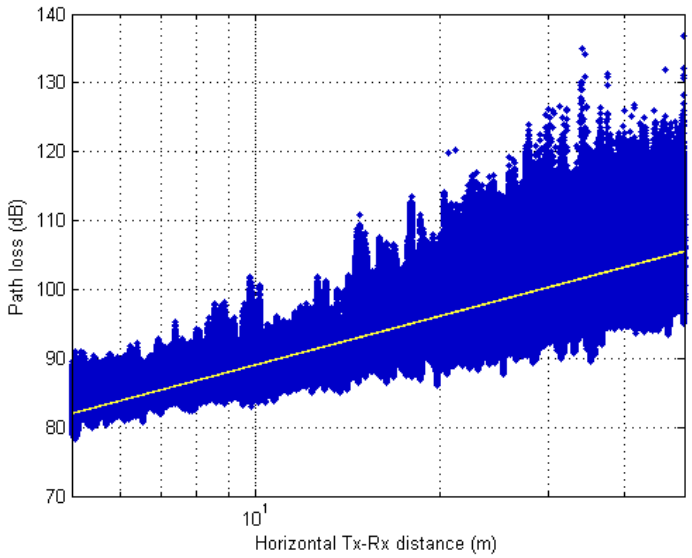

Figure 5–42: Measured path loss

In Figure 5–42 the path loss for all distances from 5 to 50 meter distance is shown as a scatter plot (blue). The yellow line is a linear fit to the data in the form of:

$$PL = \alpha + n10\log\left(\frac{d}{d_0}\right) \quad (5\text{–}37)$$

The parameters identified for this path loss model can be found in

.

Table 5-20: Path loss parameters

Type	Value
$\boldsymbol{PL_0}$	82.02 dB
$\boldsymbol{n}$	2.36
$\boldsymbol{d_0}$	5 m

The path loss exponent n is close to that of free space propagation. The spread of the path loss, as can be seen in Figure 5–43 however is not negligible. This spread can have several causes but small scale fading due to a strong ground reflection is assumed to be a major contributor. Other causes can be short obstructions of the line-of-sight path by small objects or pedestrians.

To derive a model for the instantaneous path loss in the measured environment the data in Figure 5–42 were normalized with the identified path loss exponent. Then the relative amplitude of each snapshot was calculated and probability distributions for bins of 5 meter distance were generated. For each of these distributions a Rician distribution was fit onto the data. Figure 5–43 exemplary shows the distribution and the Rician fit for the bins from 5 to 10 meter (left) and from 45 to 50 meter (right).

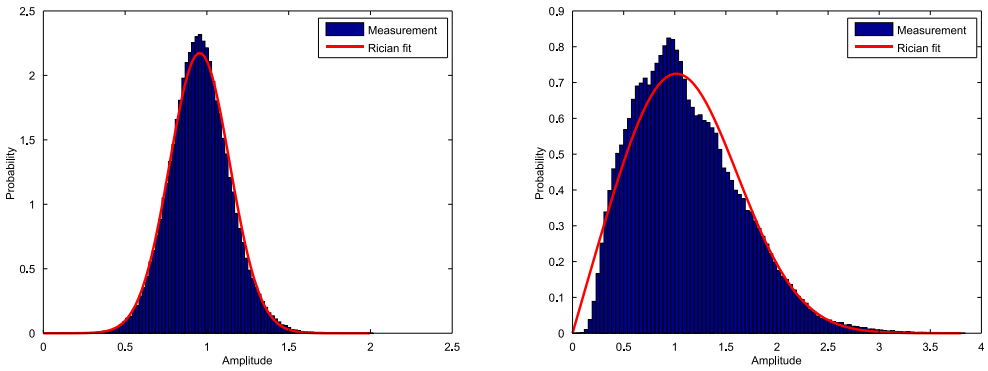

Figure 5–43: Probability distribution of relative path loss amplitude

The fitted parameters K and Omega of the Rice distribution are shown in Figure 5–44. To simplify the model a linear fit has been performed for both parameters. The parameters are:

$$K = -0.62\, d + 25\, dB \tag{5–38}$$

and

$$Omega = 0.013\, d + 1 \tag{5–39}$$

where d is the distance between transmitter and receiver.

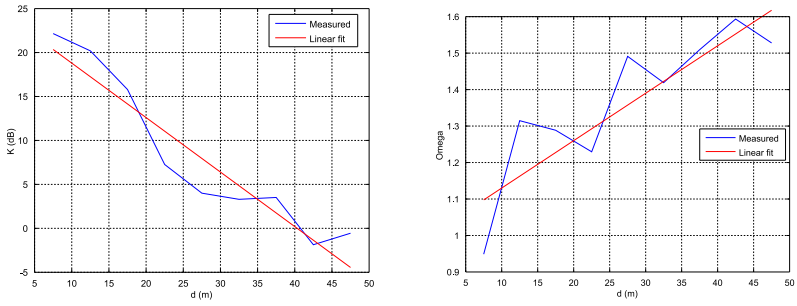

Figure 5–44: Distance dependent model parameter

Using the derived model Figure 5–45 shows a simulated scatter plot if the path loss. Compared to the measured path loss in Figure 5–42 the model yields a good accordance to the measurement.

It has to be emphasized that the derived model delivers instantaneous values of the path loss. This means that two consecutively drawn path loss values for the same or a similar distance do not behave according to effects caused for example by fading caused by a strong ground reflection. This has to be taken into account when using this model for simulations. If more realistic behaviour were necessary a more advanced path loss model has to be used, based for example on a two ray propagation model and additional statistical properties.

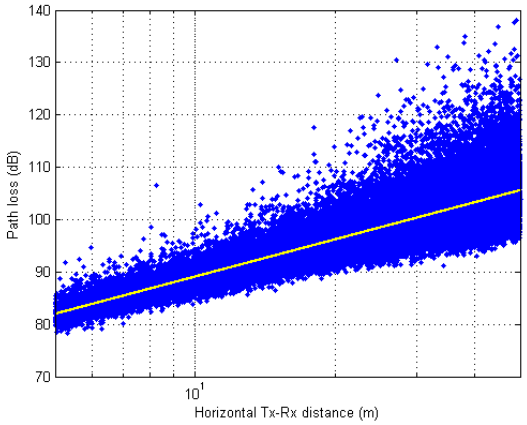

Figure 5–45: Simulated instantaneous small scale path loss

6 Conclusion

6.1 mmWave System usage models and perspectives

The research of state of the art measurement campaigns shows the feasibility of mmWave wireless communication system for access, backhaul and front haul supporting small cells assuming that the additional path loss at frequency bands above 6 GHz can be compensated by use of antenna arrays providing adequate beam forming gain. Using directive antennas reduces also the multi-paths effect such as fast-fading or delay spreading and may increase the throughput.

It can be concluded from indoor and outdoor channel measurements for 28 GHz- 100 GHz bands until now [59] that:

- Rain/Oxygen seems to be no problem for ISD < 200 meters
- Path loss exponent might be similar as for lower frequency bands at LOS ~ 2.0 , NLOS ~ 3.4-3.5 compared to free space model
- There is similar reflection loss as for lower frequency bands but much higher diffraction loss
- Blockage model is important and needs to be investigated in more details

The successful adoption of mmWave technology as an overlay to the modern mobile networks may provide very high speed access using the mmWave Small cells on the one hand and the license free mmWave links for backhaul/fronthaul. Current open issues in this concept are building shadowing, human body blockage, attenuation by dense vegetation, strong mobility effects and the handover problems.

Besides, more exploration is needed to elaborate many important aspects that affect mmWave communication systems performance: whether they are noise or interference limited, polarization effects, beamforming algorithms and antenna techniques. The system level simulations that may answer these questions require accurate and consistent model of the mmWave channel, which is the subject of the present document.

6.2 MiWEBA experimental measurements

In current state, the highly dynamic space-time characterization of the propagation channel at mmWave frequencies under real conditions still is being a research area. Therefore five measurement campaign scenarios were derived from real outdoor environments investigated in MiWEBA work package one. These are university campus (outdoor large access area), street canyon (outdoor access ultra-high rate hot spots), hotel lobby (indoor large access area), above roof top (outdoor backhaul P2P) and street canyon (outdoor front haul P2P/P2M). Taking into account that the development and verification of appropriate channel models for 60 GHz frequency band needs plenty of data from expensive measurement campaigns this report focus firstly on street canyon and university campus measurements.

For the street canyon scenario a measurement campaign with omnidirectional antennas and supporting ray tracing simulations have been performed. Analysis of this data proves the feasibility of millimeter-wave small cells but at the same time the high time variance of the propagation channel was shown. This high time variance is caused by movement of the UE itself as well as pedestrians and cars moving by. In the context of work package 5.3 these effects and strategies to establish stable connections using electronically steerable antennas or beam forming antennas will be investigated.

To complement the measurements with omnidirectional antennas, the measurements with directional and highly directional antennas were made in the university campus environment. The effects of ground reflection and scattering were investigated, the cross-polarization ratio (XPR) estimated. An additional study was accurately performed to analyze the UE motion impact on the mmWave channel characteristics.

6.3 Quasi-Deterministic channel modeling approach

A new quasi-deterministic approach has been developed for modeling the outdoor channels at 60 GHz. This methodology based on the representation of the mmWave channel model impulse response as a few quasi-deterministic strong rays (D-rays) and number of relatively weak random rays (R-rays). The experimental data obtained independently by HHI and IMC partners with help of different measurement setups were used for proposed Q-D channel model validation.

The 3D channel models for main scenarios (Open area (university campus) access, Street canyon access and Hotel Lobby access) were developed in the framework of the Q-D approach, the model parameters were selected on the base of experimental measurements and ray-tracing modeling.

The versatility of the Q-D approach allows the developed channel models for access links to be used for scenarios with same geometries. For all main scenarios the Q-D channel model may be extended to Device to Device (D2D) links with a simple

change of TX antenna parameters. The Street canyon access model may be extended to the Street-level backhaul with a change of the RX antenna parameters.

The explicit description of the deterministic (D-rays) and random (R-rays) within a model have allowed to introduce the novel approach to the mobility effects simulation. The experimental and simulation results have revealed the high sensitivity of mmWave channel characteristics to the vertical displacement of the UE. To account this effect the proposed 3D channel model provides accurate description of the UE motion in horizontal and vertical directions.

7 References

[1] "Technical Specification Group Radio Access Network; Spatial channel model for Multiple Input Multiple Output (MIMO) simulations," 3GPP TR 25.996 V11.0.0, 2012-09.

[2] "WINNER II Channel Models 2007; D5.3: WINNER+ Final Channel Models 2010," IST-4-027756 D1.1.2 V1.2, 2010.

[3] "Guidelines for evaluation of radio interface technologies for IMT-Advanced", International telecommunication union (ITU), Geneva, Switzerland, Technical Report," ITU-R M.2135-1, 2009.

[4] A. Maltsev, V. Erceg, E. Perahia, C. Hansen, R. Maslennikov, A. Lomayev, A. Sevastyanov, A. Khoryaev, G. Morozov, M. Jacob, S. Priebe, T. Kürner, S. Kato, H. Sawada, K. Sato and H. Harada, "Channel Models for 60 GHz WLAN Systems," IEEE 802.11ad 09/0334r8, 2010.

[5] R. Maslennikov and A. Lomayev, "Implementation of 60 GHz WLAN Channel Model, 10/0854r3.," IEEE, 2010.

[6] S. Jaeckel, L. Raschkowski, K. Börner and L. Thiele, ""QuaDRiGa: A 3-D Multicell Channel Model with Time Evolution for Enabling Virtual Field Trials"," IEEE Trans. Antennas Propag., 2014.

[7] "Channel Model Development and Validation," COST 2100.

[8] "D1.2 "Initial channel models based on measurements"," METIS 2020 , 2014.

[9] Y. Oda, R. Tsuchihashi, K. Tsunekawa and M. Hatay, "Measured path loss and multipath propagation characteristics in UHF and microwave frequency bands for urban mobile communications," in Vehicular Technology Conference," IEEE VTS 53, 2001.

[10] L. M. Correia, " "A view of the COST 231-Bertoni-Ikegami model," in European Conference on Antennas and Propagation (EuCAP), pp. 1681-1685.," COST 231, 2009.

[11] M. Hata, "Empirical formula for propagation loss in land mobile radio services," *IEEE Transactions on Vehicular Technology,* vol. 29, pp. 317-325, 1980.

[12] L. Correia, "Digital mobile radio towards future generation systems, final report," COST 231, 1999.

[13] IST-4-027756, "WINNER II D 1.1.2 v1.2, WINNER II Channel Models," WINNER project, 2006.

[14] M.2135, "Guidelines for evaluation of radio interface technologies for IMT-Advanced," ITU-R, 2006.

[15] K. Kitao and S. Ichitsubo, "Path loss prediction formula in Urban Area for the Fourth-Generation Mobile Communication Systems," *IEICE Trans. Comm.*, Vols. E91-B, pp. 1999-2009, 2008.

[16] K. Yonezawa, H. Ishikawa and Y. Takeuchi, "Frequency range extension of path loss prediction formula for over-rooftops propagation in microwave band," in *IEEE Antennas and Propagation Society International Symposium*, 2006.

[17] K. Sakawa, H. Masui, M. Ishii, H. Shimizu and T. Kobayashi, "Microwave path-loss characteristics in an urban area with base station antenna on top of a tall building," in *International Zurich Seminar on Broadband Communications*, 2002.

[18] M. Riback, J. Medbo, J. E. Berg, F. Harrysson and H. Asplund, "Carrier Frequency Effects on Path Loss," in *IEEE Vehicular Technology Conference*, 2006.

[19] P. Zhouyue and F. Khan, "An introduction to millimeter-wave mobile broadband systems," *IEEECommunications Magazine*, vol. 49, pp. 101-107, 2011.

[20] F. Khan and P. Zhouyue, " mmWave mobile broadband (MMB): Unleashing the 300GHz spectrum," in *IEEE Sarnoff Symposium*, 2011.

[21] E. J. Violette, R. H. Espeland, R. O. DeBolt and F. K. Schwering, "Millimeter-wave propagation at street level in an urban environment,"," *IEEE Transactions on Geoscience and Remote Sensing, , vol. 26,* pp. 368-380, 1988.

[22] H. J. Thomas, R. S. Cole and G. L. Siqueira, "An experimental study of the propagation of 55 GHz millimeter waves in an urban mobile radio environment," *EEE Transactions on Vehicular Technology, vol. 43,* pp. 140-146, 1994.

[23] A. M. Hammoudeh, M. G. Sanchez and E. Grindrod, "Experimental analysis of propagation at 62 GHz in suburban mobile radio microcells," *IEEE Transactions on Vehicular Technology, vol. 48,* pp. 576-588, 1999.

[24] L. M. Correia, J. J. Reis and P. O. Frances, "Analysis of the average power to distance decay rate at the 60 GHz band," in *IEEE in Vehicular Technology Conference*, 1997.

[25] A. V. Raisanen, J. Ala-Laurinaho, K. Haneda, J. Jarvelainen, A. Karttunen, M. Kyro, V. Semkin, A. Lamminen and J. Saily, "Studies on E-band antennas and propagation," in *Antennas and Propagation Conference (LAPC)*, Loughborough, 2013 .

[26] M. Kyro, V. Semkin and V. Kolmonen, "Empirical characterization of scattering pattern of built surfaces at mm-wave frequencies," in *European Conference on Antennas and Propagation (EuCAP)*, 2013.

[27] M. Kyro, S. Ranvier, V. Kolmonen, K. Haneda and P. Vainikainen, "Long range wideband channel measurements at 81-86 GHz frequency range," in

European Conference Antennas and Propagation (EuCAP), 2010.

[28] M. Kyro, V. Kolmonen and P. Vainikainen, "Experimental Propagation Channel Characterization of mm-Wave Radio Links in Urban Scenarios," *IEEE Antennas and Wireless Propagation Letters*, vol. 11, pp. 865-868, 2012.

[29] T. S. Rappaport, S. Shu, R. Mayzus, Z. Hang, Y. Azar, K. Wang, G. N. Wong, J. K. Schulz, M. Samimi and F. Gutierrez, "Millimeter Wave Mobile Communications for 5G Cellular: It Will Work!," *IEEE Access*, vol. 1, pp. 335-349, 2013.

[30] S. Rangan, T. S. Rappaport and E. Erkip, "Millimeter-Wave Cellular Wireless Networks: Potentials and Challenges," *Proceedings of the IEEE*, vol. 102, pp. 366-385, 2014.

[31] M. Samimi, K. Wang, Y. Azar, G. N. Wong, R. Mayzus, Z. Hang, J. K. Schulz, S. Shu, F. Gutierrez and T. S. Rappaport, "28 GHz Angle of Arrival and Angle of Departure Analysis for Outdoor Cellular Communications Using Steerable Beam Antennas," in *IEEE conference in Vehicular Technology Conference (VTC Spring)*, New York City, 2013.

[32] T. S. Rappaport, E. Ben-Dor, J. N. Murdock and Q. Yijun, "38 GHz and 60 GHz angle-dependent propagation for cellular & peer-to-peer wireless communications," in *IEEE International Conference on Communications (ICC)*, 2012.

[33] E. Ben-Dor, T. S. Rappaport, Q. Yijun and S. J. Lauffenburger, "Millimeter-Wave 60 GHz Outdoor and Vehicle AOA Propagation Measurements Using a Broadband Channel Sounder," in *IEEE Global Telecommunications Conference (GLOBECOM)*, 2011.

[34] T. S. Rappaport, Q. Yijun, J. I. Tamir, J. N. Murdock and E. Ben-Dor, "Cellular broadband millimeter wave propagation and angle of arrival for adaptive beam steering systems," in *IEEE Radio and Wireless Symposium (RWS)*, 2012.

[35] T. S. Rappaport, F. Gutierrez, E. Ben-Dor, J. N. Murdock, Q. Yijun and J. I. Tamir, "Broadband Millimeter-Wave Propagation Measurements and Models Using Adaptive-Beam Antennas for Outdoor Urban Cellular Communications," *IEEE Transactions on Antennas and Propagation*, vol. 61, pp. 1850-1859, 2013.

[36] J. N. Murdock, E. Ben-Dor, Q. Yijun, J. I. Tamir and T. S. Rappaport, "A 38 GHz cellular outage study for an urban outdoor campus environment," in *IEEE Wireless Communications and Networking Conference (WCNC)*, 2012.

[37] X. Hao, T. S. Rappaport, R. J. Boyle and J. H. Schaffner, "38-GHz wide-band point-to-multipoint measurements under different weather conditions," *IEEE Communications Letters*, vol. 4, pp. 7-8, 2000.

[38] G. R. MacCartney, J. Zhang, S. Nie and T. S. Rappaport, "Path loss models for

5G millimeter wave propagation channels in urban microcells," in *Global Communication Conference (Globecom 2013)*, Atlanta, 2013.

[39] Y. Azar, G. N. Wong, K. Wang, R. Mayzus, J. K. Schulz, Z. Hang, F. Gutierrez, D. Hwang and T. S. Rappaport, ""28 GHz propagation measurements for outdoor cellular communications using steerable beam antennas in New York city," in *IEEE International Conference on Communications (ICC)*, 2013.

[40] T. S. Rappaport and S. Shu, "Multi-beam antenna combining for 28 GHz Cellular link Improvement in urban environments," in *IEEE Global Telecommunication Conference (Globecom)*, Atlanta, 2013.

[41] M. R. Akdeniz, Y. Liu, M. Samimi, S. Sun, S. Rangan, T. S. Rappaport and E. Erkip, "Millimeter wave channel modeling and cellular capacity evaluation".

[42] Z. Hang, R. Mayzus, S. Shu, M. Samimi, J. K. Schulz, Y. Azar, K. Wang, G. N. Wong, F. Gutierrez and T. S. Rappaport, "28 GHz millimeter wave cellular communication measurements for reflection and penetration loss in and around buildings in New York city," in *IEEE International Conference on Communications (ICC)*, 2013.

[43] W. Keusgen, A. Kortke, M. Peter and R. Weiler, "A highly flexible digital radio testbed and 60 GHz application examples," in *IEEE European Microwave Conference (EuMC)*, 2013.

[44] M. W. M. Peter, W. K. M. Raceala-Motoc, R. Felbecker, M. Jacob, S. Priebe and T. Kürner, "Analyzing human body shadowing at 60 GHz: Systematic wideband MIMO measurements and modeling approaches," in *IEEE 6th European Conference on Antennas and Propagation*, 2012.

[45] R. Felbecker, L. Raschkowski, W. Keusgen and M. Peter, "Electromagnetic wave propagation in the millimeter wave band using the NVIDIA OptiX GPU ray tracing engine," in *Antennas and Propagation (EUCAP), 2012 6th European Conference on*, Prague, 2012.

[46] M. Peter, W. Keusgen and R. Felbecker, "Measurement and ray-tracing simulation of the 60 GHz indoor broadband channel: Model accuracy and parameterization.," in *Antennas and Propagation, 2007. EuCAP 2007. The Second European Conference on*, Edinburgh, 2007.

[47] A. Maltsev, A. R. Maslennikov, Sevastyanov, A. Khoryaev and A. Lomayev, "Experimental investigation of 60 GHz wireless systems in office environment," *IEEE JSAC*, vol. 27, no. 8, pp. 1488-1499, 2009.

[48] H. Sawada, "Intra-cluster response model and parameter for channel modeling at 60 GHz (Part 3)," IEEE doc. 802.11-10/0112r1, January 2010.

[49] WINNER, "Spatial channel model for multiple input multiple output (MIMO) simulations", 3GPP TR 25.996 V6.1.0," September 2003. [Online]. Available: http://www.3gpp.org/ftp/Specs/html-info/25996.htm.

[50] F. Khan and Z. Pi, "Millimeter-wave Mobile Broadband (MMB): Unleashing 3-300GHz Spectrum," in *IEEE Sarnoff Symposium*, 2011.

[51] F. Khan and Z. Pi, "An introduction to millimeter-wave mobile broadband systems," *IEEE Comm. Mag.*, vol. 49, no. 6, p. 101 – 107, 2011.

[52] A. Hammoudeh, M. Sanchez and E. Grindrod, "Modelling of Propagation in Outdoor Microcells at 62.4GHz," in *Microwave Conference , vol.1, no., pp.119,123,*, 1997.

[53] K. Sarabandi, E. Li and A. Nashashibi, "Modeling and measurements of scattering from road surfaces at millimeter-wave frequencies," *IEEE Transactions on Antennas and Propagation*, vol. 45, no. 11, pp. 1679-1688, 1997.

[54] "IMST 60 GHz indoor radio channel measurement data," ACTS MEDIAN project technical report.

[55] A. Davydov, A. Maltsev and A. Sadri, "Saleh-Valenzuela channel model parameters for library environment," IEEE document 802.15-06-0302-02-003c, July 2006.

[56] K. Sato, T. Manabe, T. Ihara, H. Saito, S. Ito, T. Tanaka, K. Sugai, N. Ohmi, Y. Murakami, M. Shibayama, Y. Konishi and T. Kimura, "Measurements of reflection and transmission characteristics of interior structures of office building in the 60-GHz band," *Antennas and Propagation, IEEE Transactions on*, vol. 45, no. 12, pp. 1783-1792, 1997.

[57] A. Maltsev, A. Pudeyev, Sadri, A. and C. Cordeiro, "Millimeter-Wave Transceiver With Coarse And Fine Beamforming With Interference Suppression And Method". US 11 2013.

[58] "3GPP TR 36.814 V9.0.0 (2010-03)," 3GPP , 2010.

[59] P. Merz, "Optimizing Spectrum Usage for 2020 and beyond," in *Johannesberg Summit 2014*, 2014 .